DEVELOPMENT OF A 1D HYBRID FLUID-PIC PLASMA MODEL OF LOW POWER HALL THRUSTERS FOR SMALL SPACECRAFT

DÉVELOPPEMENT D'UN MODÈLE PLASMA FLUIDE-PARTICULAIRE HYBRIDE-1D DE PROPULSEURS À EFFET HALL DE FAIBLE PUISSANCE POUR ENGINS SPATIAUX DE PETITE TAILLE

A Thesis Submitted to the Division of Graduate Studies
of the Royal Military College of Canada
by

Curtis Michael Graham

In Partial Fulfillment of the Requirements for the Degree of
Master of Applied Science in Aeronautical Engineering

June, 2023

"I realize I don't know very much. None of us knows very much. But we can all learn more. Then we can teach one another."

- Octavia E. Butler, Parable of the Sower

Development of a 1D hybrid Fluid-PIC plasma model of
low power Hall thrusters for small spacecraft

Développement d'un modèle plasma fluide-particulaire hybride-1d de
propulseurs à effet hall de faible puissance pour engins spatiaux de petite taille

Candidate / Candidat

Curtis Graham
Mechanical and Aerospace Engineering
Royal Military College of Canada

MASc Candidate in Aeronautical Engineering /
Maîtrise candidat en génie aéronautique

Examination Committee / Comité examinateur

Dr. Frank Zeman *Royal Military College of Canada*	Chair / Président
Dr. Igor Telichev *University of Manitoba*	External / Externe
Dr. Patrick Julien *Royal Military College of Canada*	Internal-External / Interne-Externe
Dr. Diane Wowk *Royal Military College of Canada*	Internal / Interne
Dr. Manish Jugroot *Royal Military College of Canada*	Supervisor / Superviseur

Acknowledgements

I would like to thank everyone that made this project possible, and allowed me to explore my passion for space propulsion. Special thanks to Dr Manish Jugroot and the rest of the team at RAPPEL (RMC Advanced Plasma Propulsion and Exploration Laboratory) who were invaluable in their assistance and support throughout. Thanks to Peter, Felix, Luis, Griffin, and Ivan. An additional thank you goes out to the support staff within the Department of Mechanical and Aerospace Engineering at RMC, none of this would be possible without you. A thanks to my family and friends who supported me throughout this journey, and who put up with me endlessly talking about my research. A final thank you is owed to the Natural Sciences and Engineering Research Council of Canada (NSERC) and the Director General of Air and Space Force Development providing funding for this research.

Abstract

Electric spacecraft propulsion allows for significant increases in efficiency and specific impulse over traditional chemical combustion rockets. Hall thrusters are a form of electric propulsion that use a crossed magnetic and electric field to trap electrons and accelerate ions to provide thrust, and their relatively low thrust and high impulse makes them idea for micropropulsion systems on small satellites. The traditionally calculated cross field mobility in Hall thrusters is significantly lower than what is observed experimentally. The mechanism of this anomalous electron mobility in Hall thrusters is not comprehensively understood, and appears to be more significant in lower power devices. To examine anomalous diffusion, and to design and characterize the performance of low power thrusters, numerical simulation provides an ideal avenue. This thesis presents the development and design of a one-dimensional hybrid fluid particle-in-cell simulation software for the characterization and investigation of low power Hall thrusters, and the use of said model to theoretically increase the efficiency of an existing low power thruster.

Résumé

La propulsion électrique des engins spatiaux permet d'augmenter considérablement l'efficacité et l'impulsion spécifique par rapport aux fusées chimiques traditionnelles. Les propulseurs à effet Hall sont une forme de propulsion électrique qui utilise une configuration de champ magnétique et électrique croisé pour piéger les électrons et accélérer les ions afin de fournir une poussée. Leur poussée relativement faible et leur impulsion élevée en font un candidat idéal pour les systèmes de micropropulsion sur les satellites de petite taille. La mobilité dans les propulseurs à effet Hall est significativement inférieure à ce qui est observé expérimentalement et le mécanisme de cette mobilité anormale des électrons dans les propulseurs à effet Hall n'est pas entièrement comprise – et semble être plus important dans les dispositifs de faible puissance. Pour examiner la diffusion anormale et aider à la conception et à la caractérisation des performances des propulseurs de faible puissance, la simulation numérique offre une excellente méthodologie. Cette thèse présente le développement, la conception et la validation d'un logiciel hybride fluide-particulaire unidimensionnel de simulation pour la caractérisation et l'étude de propulseurs à effet Hall de faible puissance pour les petits engins spatiaux.

Nomenclature

α	=	Ionization fraction
ϕ	=	Localized electric potential
θ	=	Collision cross section
μ_{de}	=	Electron mobility
μ_e	=	Electron mobility tensor
λ_k	=	Mean free path, interaction k
λ_D	=	Debye Length
γ	=	Secondary Emission Coefficient
Γ_k	=	Flux, species k
Γ_∞	=	Incomplete Gamma Function
ϵ	=	Electrical permittivity
ρ_k	=	Density, species k
ω	=	Frequency
η	=	Efficiency
ν	=	Collision Frequency
Ω	=	Hall Parameter
$\mathbf{B}$	=	Magnetic field
$\mathbf{D}_k$	=	Diffusivity, species k
$\mathbf{E}$	=	Electric field
A	=	Area
a	=	Acceleration
F	=	Force
g	=	Gravitational Constant
I	=	Electric current
I_{sp}	=	Specific Impulse
$\mathbf{j}$	=	Current Density
k_B	=	Boltzmann Constant
L	=	Length
m_k	=	Mass, species k

n_k	=	Number density, species k
P	=	Power
$\mathbf{p}_k$	=	Momentum, species k
p_k	=	Pressure, species k
q	=	Charge
r	=	Radial distance
r_L	=	Lamor Radius
S	=	Source Term
T	=	Thrust
t	=	Time
T_k	=	Temperature, species k
$\mathbf{u}$	=	Drift Velocity
U	=	Electric potential
$\mathbf{v}$	=	Velocity
x	=	Position

Acronyms

Acronym	Full Form
CHT	Cylindrical Hall Thruster
DSMC	Direct Simulation Monte Carlo
EEDF	Electron Energy Distribution Function
FEMM	Finite Element Methods Magnetics
MCC	Monte-Carlo-Collisions
MMC	Melikov-Morozov Criterion
NWC	Near-Wall Conductivity
PDE	Partial Differential Equation
PIC	Particle-in-Cell
PPPL	Princeton Plasma Physics Laboratory
RAPPEL	RMC Advanced Plasma Propulsion and Exploration Laboratory
RHS	RAPPEL Hall Simulation
SEE	Secondary Electron Emission
SPT	Stationary Plasma Thruster

Contents

1 Introduction

1.1 Rocket propulsion: Introduction

Rocket propulsion is a form of propulsion that ejects mass from a vehicle to push it in the opposite direction. Conservation of momentum dictates that any momentum imparted by accelerating the propellant must be conserved via the acceleration of the vehicle in the opposite direction of propellant ejection. This principle has been widely studied and implemented throughout history in a diverse array of technologies from massive chemical boosters too micro-scale satellite thrusters. Tsiolkovsky pioneered the field of rocket science through his development of the rocket equation and early designs of space faring vehicles [46]. His work forms the basis of the modern field of rocket science used today.

Tsiolkovsky developed an idea called Free Space, which is a theoretical space independent of the effects of gravity or drag. In this space, ejecting mass from a body will cause it to accelerate proportionally in the other direction. A higher velocity of ejected propellant indicated a higher momentum transfer occurring between the vehicle and propellant, resulting in a higher acceleration. The modeling of this relationship leads to the rocket equation.

1.1.1 Rocket equation: Principles

To develop this model, the first step is conservation of momentum. Expressing the change in velocity of the rocket, dV, as an expression of the rocket's mass M_r, mass of fuel M_f, and an infinitesimal mass of spent fuel dM results in equation 1.2 [46].

$$0 = \Delta \mathbf{P}_r + \Delta \mathbf{P}_{exhaust} \tag{1.1}$$

$$dV_r(M_r + M_f) = V_{exhaust} dm \tag{1.2}$$

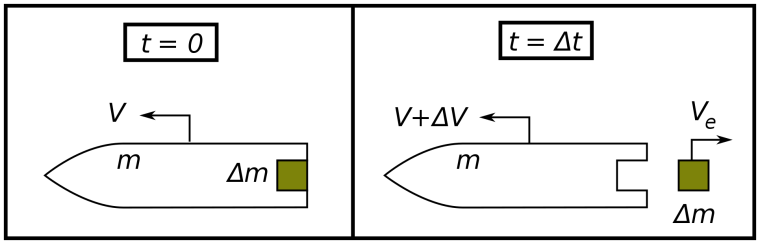

Figure 1.1: Rocket Propulsion System

Separation of variables and integration is the next step. Conservation of mass dictates that the infinitesimal exhaust fuel mass dM is equal to the change in fuel mass M_f, and is negative in equation 1.3 [46].

$$\int \frac{1}{V_{exhaust}} dV = -\int \frac{1}{M_r + M_f} dm \tag{1.3}$$

$$\frac{V}{V_{exhaust}} = -\ln(M_r + M_f) + C \tag{1.4}$$

Assuming an initial mass of $m_i = M_r + M_f$ when stationary, $V = 0$, the constant can be calculated via equation 1.5.

$$0 = -\ln\Big(M_r + M_f\Big) + C \tag{1.5}$$

$$C = \ln(M_r + M_f) \tag{1.6}$$

When this constant is substituted back into 1.4, it gives the rocket equation. This equation, equation 1.8, expresses the velocity of the rocket, V_{rocket}, in terms of the ratio of the initial full rocket mass to current rocket mass, m_i/m, and the exhaust velocity of the fuel $V_{exhaust}$ [46].

$$\frac{V}{V_1} = \ln\left(\frac{M_r + M_2}{M_r + M_f}\right) \tag{1.7}$$

$$\Delta V_r = V_{exhaust} \ln\left(\frac{M_r + M_f}{M_r}\right) \tag{1.8}$$

For a vehicle to achieve a given speed in free space, it must accelerate $m_i - m$ propellant to speed $V_{exhaust}$. As one would expect, the change in velocity and mass in a nonlinear relationship. As the vehicle gets lighter, the same amount of fuel, dM, will add more ΔV to the vehicle. As more fuel is added to the vehicle, it will reduce the ΔV experienced per amount of fuel, dM. This equation is also time independent. It does not matter over what time the fuel is accelerated or how consistently, only that it does indeed get accelerated to the give $V_{exhaust}$. At that point, the vehicle will have achieved the prescribed ΔV. Section 1.3 will outline how electric propulsion can achieve higher a ΔV than chemical combustion rockets, making it an ideal candidate for long missions such as deep space exploration, interplanetary travel, and satellite orbit maintenance.

1.1.2 Rocket Propulsion Metrics

Thrust

Given an understanding of the relationship between rocket vehicle velocity and propellant velocity, it would be useful to quantify the relationship in time. Newton's Laws of Motion can be combined with the rocket equation to determine the thrust force generated by the rocket in question. Using the rocket as a moving reference frame, the exhaust velocity can be treated as a constant and factored out of the derivative as seen in equation 1.11.

$$F_{thrust} = \frac{d}{dt}\mathbf{P}_r = -\frac{d}{dt}\mathbf{P}_{exhaust} \tag{1.9}$$

$$F_{thrust} = -V_{exhaust}\frac{d}{dt}m \tag{1.10}$$

$$F_{thrust} = -V_{exhaust}\dot{m} \tag{1.11}$$

While the final velocity of a rocket is not dependant on thrust, as seen from the rocket equation 1.8, it is still an important metric for rocket propulsion systems. Launch vehicles have to produce enough force to overcome gravity, and station-keeping thrusters only require enough force to nudge a satellite over weeks or months. Both of these applications would have wildly differing mass flow rates and would make comparison difficult. Exhaust velocity is often used a a comparison metric instead of thrust, and is often referred to as specific impulse [47].

Specific impulse

Specific impulse if the impulse a rocket propulsion system generates per unit weight of fuel used to generate that force. It can be thought of as the mass efficiency of the system, a measurement of how effectively the propellant is used in generating thrust. The calculation of this can be seen in equation 1.14.

$$I = F \quad dt = V_{exhaust}\dot{m} \quad dt \tag{1.12}$$

$$I_{sp} = \frac{F \quad dt}{\dot{m}g \quad dt} = \frac{V_{exhaust}\dot{m} \quad dt}{\dot{m}g \quad dt} \tag{1.13}$$

$$I_{sp} = \frac{V_{exhaust}}{g} \tag{1.14}$$

The units for specific impulse work out to be seconds, but can be thought about as Newton-seconds per Newton. The impulse generated per unit weight of propellant. When the mass ratio for fuel to vehicle is a critical aspect of rocket performance, as outlined in equation 1.8, optimizing the exhaust velocity is of critical importance. Specific impulse is a measure of this optimization [47].

In traditional chemical rockets, the propellant is accelerated through thermal expansion through a nozzle, driven by a combustion reaction. As such, there is a hard limit on the specific impulse determined by the chemical energy density of the fuel [12]. Assuming a 100% conversion of chemical potential energy to kinetic energy, a fuel mix of hydrogen and liquid oxygen has a maximum specific impulse of around 300s. This limit on impulse means that huge amounts of propellant must be used to achieve high ΔV in chemical rocket propelled spacecraft. This hindrance motivates investigation of propulsion methods that can reach higher specific impulses.

1.2 Electric propulsion for spacecraft

The use of electromagnetic fields to accelerate particles has been well documented, and can accelerate particles to much higher speeds than thermal gas expansion in nozzles. These thrusters have been used since the 1960's when the Soviet space program first launched electric thrusters in space missions [47].

Charged particles in an electric field will experience a Coloumb force proportional to the charge of the particle, as described in equation 1.15. These fields can be used to accelerate propellants in an electric rocket.

$$F_e = qE \tag{1.15}$$

This can greatly increase the exhaust speed of propellant in a rocket propulsion system, resulting in much higher specific impulses than seen in chemical rockets. These impulses can range from the chemical upper limit of 500s all the way up to 14,000s [26].

However, there are still limitations to these systems. One such limitation is charge accumulation. Consider a neutrally charged satellite, if it were to eject massive amounts of positively charged particles conservation of charge would dictate that the satellite would begin to accumulate a negative charge of its own. This would then start to attract the propellant back to the spacecraft via the same mechanism that accelerated it in the first place, and greatly reduce the exhaust velocity.

Another limitation is the neutral particle density in the acceleration channel. High neutral densities within the acceleration regime of the thruster will reduce the speed that the charge particles can reach. A high neutral density will result in many collisions with the neutrals, losing speed and momentum with each collision. This makes many electric rockets inoperable in atmospheric conditions.

Power becomes an important metric when dealing with electric thrusters. Generating currents at high voltages means that power requirements will increase. Increasing the speed at which the exhaust exits the craft often increases the current needed to neutralize the exhaust, and in turn increases the power requirements of the thruster.

There are three distinct families of electric thruster which will be outlined in the following sections. Electrostatic thrusters that use electric fields to accelerate reactions mass, electrothermal thrusters that use electricity to heat up reaction mass and use the thermal expansion to drive the thrust, and electromagnetic thrusters that use a combination of electric and magnetic thrusters. Figure 1.2 shows a plot highlighting chemical and electric propulsion

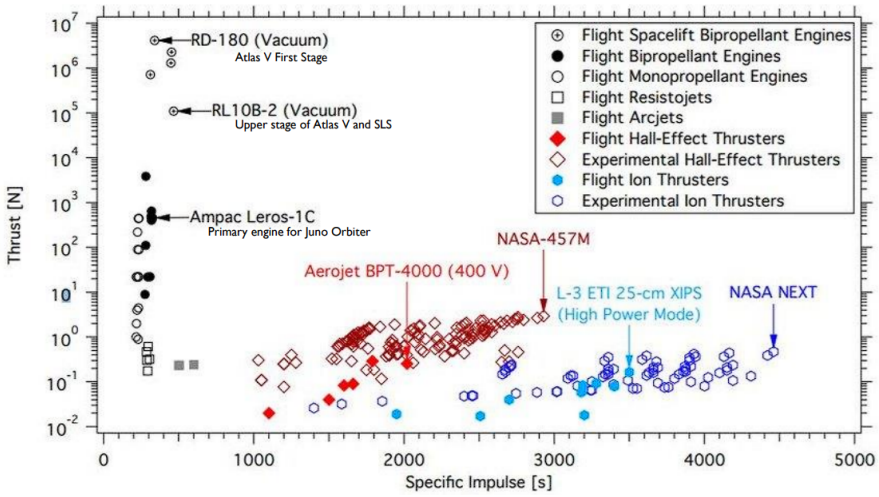

Figure 1.2: Rocket Propulsion Systems: Thrust *vs* Specific Impulse (from [21])

devices by thrust vs. specific impulse, and specifies some specificaly well known thrusters.

1.2.1 Electrothermal thrusters

Electrothermal thrusters are similar to chemical rockets. They use thermal expansion of a propellant directed through a nozzle to generate thrust. Rather than relying on chemical reactions to heat the propellant, electrothermal thrusters use electrical heating to supplement a chemical reaction. This increases the energy density of the fuel, and can produce higher specific impulses than chemical rockets.

Resistojet thrusters

A resistojet, as seen in figure 1.3, uses a high current running through a restive heating element to generate heat, and then runs propellant across the surface of the resistor to transfer the heat via convection. This allows for increases in specific impulse, as the temperature is no longer limited by the chemical potential energy of the propellant, only the power that can be run through the resistor. Resistojets can produce anywhere from 0.5 to 6000 mN of thrust at 150 to 850 s of specific impulse [20]. Resistojets are limited by

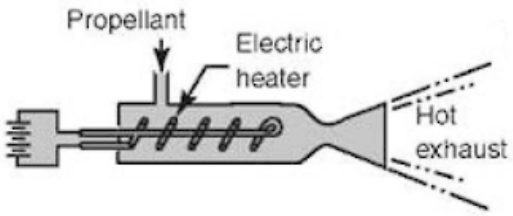

Figure 1.3: Resistojet Thruster from [47]

the material characteristics of the heating element and the electrical power required to use it.

Arcjet thrusters

Arcjets operate using a similar scheme, but rather than use a resistive heating element, they use an discharge arc between electrodes to generate the heat in the propellant. This allows for higher temperatures to be achieved in the propellant and higher specific impulses accordingly. Arcjets function in the range of 50 to 6800 mN of thrust at 130 to 2200 s of specific impulse [20]. Arcjets typically suffer from significant cathode ablation from the high current discharge entering the cathode, in addition to energy efficiency from the high power required to maintain an arc discharge.

1.2.2 Electrostatic thrusters

Electrostatic thrusters use a static electric field to accelerate charged particles. The nature of those charge particles can vary from molecules to ions. The departure from thermal expansion reduces energy lost from heat transfer to surroundings, and more efficiently accelerates the reaction mass.

Ion thrusters

Ion thrusters are the simplest type of electrostatic thruster. They generate ions through ionization of a neutral propellant gas, then extract and accelerate those ions with the use of a series of electrically biased gridded electrodes. The electrical bias generates an electric field, which will accelerate the ions towards it. The ion gets accelerated through the grids, where a secondary electron source provides a current of electrons to neutralize the ion beam to

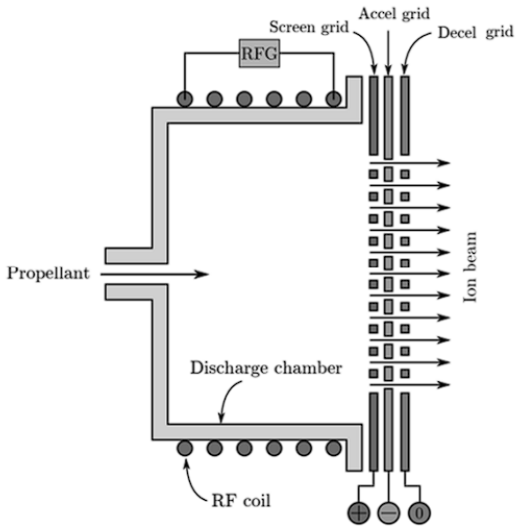

Figure 1.4: Gridded Ion Thruster (from [43])

avoid charge buildup. Figure 1.4 depicts a simple diagram of an ion thruster. An electron source to induce ionization in the neutral propellant, an series of electrodes to extract and accelerate the ionized propellant, and another electron source to neutralize the current.

Ion thrusters can achieve specific impulse on the scale of 1500-10,000 s and thrusts from 0.01–750 mN, but face drawbacks from the complexity of the power systems required [20]. Space charge also limits the mass flow rate of the system. Too many positive charges in the same location will start to generate an electric field that works against the field generated by the electrodes, resulting in reduced specific impulse. Finally, electrode failure is also an issue in gridded ion thrusters, as repeated impacts of ions on the electrodes causes wear over time and eventually device failure.

Electrospray thrusters

Electrospray thrusters use a similar approach. They are micro-scale thrusters that use a charged fluid as a propellant, and they accelerate droplets of that fluid through a series of electrodes. Typically some sort of porous medium is used as the propellant emitter, and an electric field will spray droplets off of the emitter and accelerate them similarly to an ion thruster. A distinct ad-

vantage of electrospray thrusters is the ability to use positively and negatively charged fluid in an alternating firing scheme to eliminate the need for beam neutralization.

1.2.3 Electromagnetic thrusters

Electromagnetic thrusters use a combination of electric and magnetic fields to produce thrust. Magnetic fields apply a force on charged particles perpendicular to the direction of motion, as described by the Lorentz Law as shown 2.28.

$$F_B = q \cdot \mathbf{u} \times \mathbf{B} \tag{1.16}$$

The perpendicular nature of this force means that charged particles cannot be accelerated linearly by a static magnetic field, only deflected. As a result, magnetic fields are used to contain charged particles and focus them rather than accelerate. This results in a diverse set of thrusters.

Pulsed plasma thrusters

Pulsed plasma thrusters use an arc discharge similar to arcjet thrusters, but use the self generated magnetic field to focus the charged particles. An ablative anode, typically made of Teflon, disintegrates when the discharge arc makes contact with it. The high electron current jumping to the anode generates a very high strength magnetic field that focuses the ions produced by the disintegrating anode and ejects them from the thruster. These thrusters can only operate at high power on account of the high current discharge required for operation, limiting their applications. Typical specific impulses range from 1400-2700 s and thrusts from 0.05-10 mN [20].

Hall thrusters

Hall thrusters use a crossed axial electric and radial magnetic field to generate thrust. The magnetic field captures electrons in a Hall current (described in detail in section 1.4) that creates an electric field which ionizes and accelerates ions similarly to an electrostatic thruster [20]. The presence of electrons and ions within the plasma eliminates the space charge limitation of the electrostatic thrusters, so higher thrusts can be achieved with these thrusters (see figure 1.5).

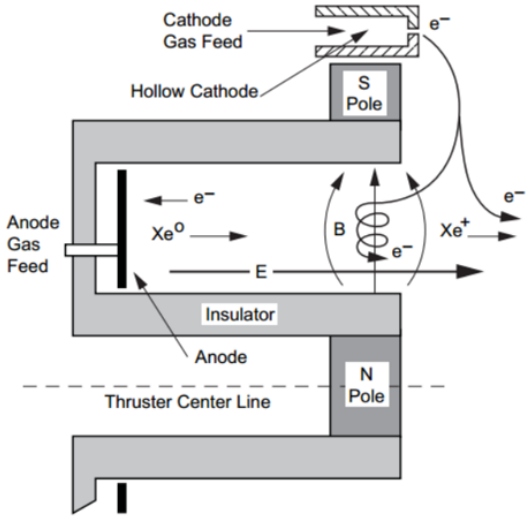

Figure 1.5: Hall thruster (from [28])

Typical failure methods for Hall thrusters are channel wall erosion, cathode failure, and material thermal failure. Higher densities of charged particles result in higher ablation rates of the materials in the thruster, and also require higher currents from the cathode neutralizer to maintain vehicle neutrality. These thrusters can achieve specific impulse in the range of 600–3000 s and thrusts from 0.01–2000 mN. The operating principles of Hall thrusters require knowledge of plasmas to fully understand.

1.3 Research motivation

Computer modeling of physical systems provides significant advantages in the engineering process, and can help with the design of experiments and testing of physical models. Hall thruster simulation software is difficult to attain, and limits the capacity of the RAPPEL lab to conduct research into Hall thruster micropropulsion systems. The development of an efficient 1D numerical plasma model for Hall thrusters will allow for the RAPPEL lab to investigate and design micro hall thrusters and their associated phenomenon with increased accuracy and efficiency.

2 Background on Hall Thrusters

2.1 Plasmas: Characteristics and behaviour

Plasma is a state of matter defined as a fluid that is partially or completely ionized. Being a mixture of ions, electrons, and neutral gas species, the physics that govern the behaviour of plasma is complex. A mixture of electrodynamics, fluid dynamics, chemistry, and thermodynamics. Plasmas are the most abundant state of visible matter in the universe, and can account for 99 % of visible matter [36].

2.1.1 Plasma collective behaviour

A natural starting point for the mathematical modeling of a plasma is with a neutral gas. Gasses are defined using mass densities and number densities of atoms/molecules in a given volume. Number density can be used in an ideal gas to determine pressure and temperature from the ideal gas law, equation 2.1 where n is number density, p is pressure, k_B is the Boltzmann constant and T is temperature.

$$p = nk_BT \tag{2.1}$$

Just as a gas is a fluid composed of neutral particles, plasmas can be thought of a a mixture of an electron gas, ion gas, and neutral gas all with their own number density, pressure, and temperature. The number densities for electrons, n_e, ions, n_i, and atoms, n_a, are all distinct properties of a plasma [36].

Ionization is required to form a plasma. In space propulsion, the primary mechanism of ionization is electron impact ionization, seen in equation 2.2.

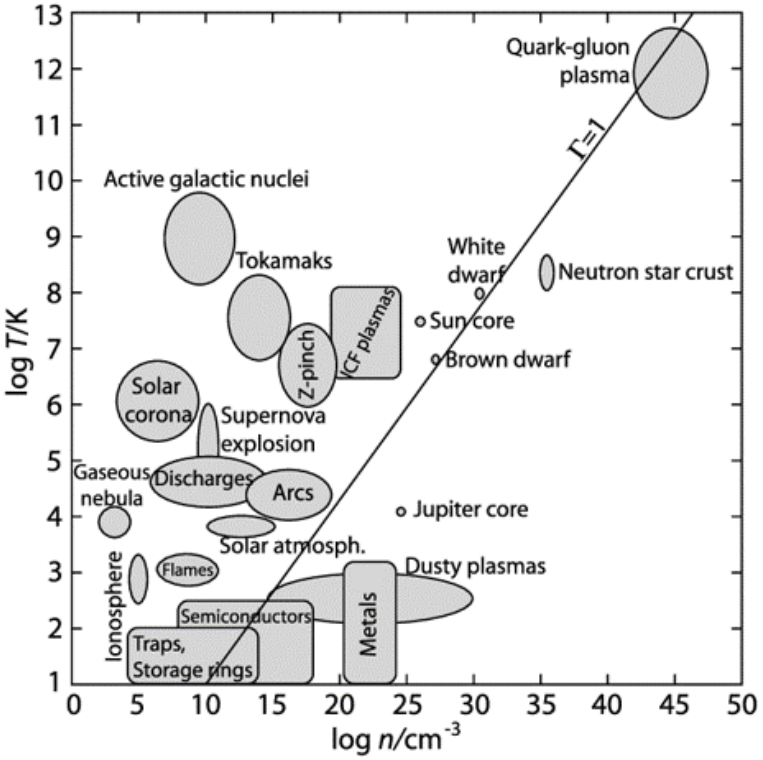

Figure 2.1: Plasma Temperature *vs* Density (from [10])

This is where a high energy electron impacts a neutral atom and imparts sufficient energy to dissociate the outermost electron bound to the neutral atom. In a bulk gas when there is sufficient energy, this causes an avalanche of ionization events, each one producing an additional electron.

$$e + Xe \rightarrow Xe^{+} + 2e \tag{2.2}$$

Other mechanisms for ionization exist such as photionization, but they are not as relevant for plasmas in electric propulsion. Photoionization is a much more significant mechanism in some experimental Fusion reactors and in stellar cores [36].

Plasmas differ significantly from a mixture of neutral gasses as they have an inherent electrical charge. This means that the electronic gas and ionic gas will exert a force both on themselves and on each other beyond just the

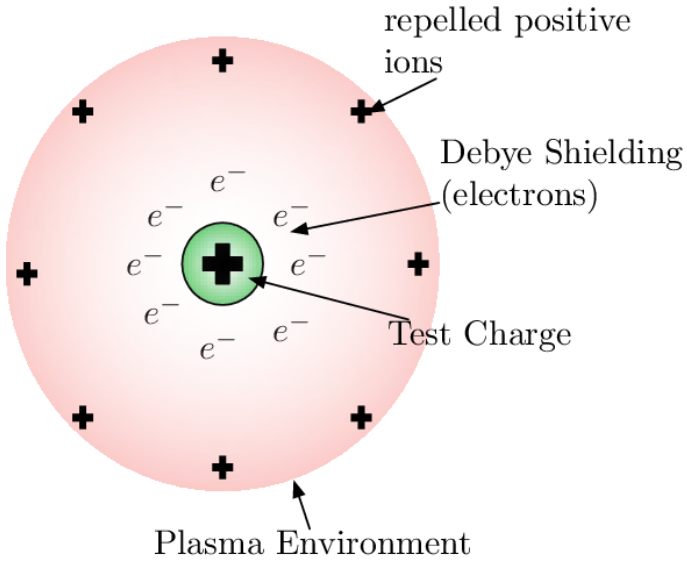

Figure 2.2: Mechanism of Debye shielding (From [40])

collisions seen in a typical gas mixture. This results in collective behaviour. An outside stimulus that effects some number of particles will have an effect on the behaviour of the entire system through a cascading series of electrostatic interactions [36].

Debye shielding

One of the most significant bulk behaviours of a plasma is self shielding, or Debye shielding. Take an even distribution of electrons and ions, ie $n_{e1} = n_{i1}$ as shown in figure 2.2. Inserting a positive test charge $Q+$ into the plasma will attract the electrons in the vicinity, and repel the ions. This creates a local charge perturbation. The nature of this perturbation will serve to reduce the electric field generated by the charge $Q+$ by the increase in negative charge in its immediate surroundings, effectively shielding the charges further away from its influence [36].

To mathematically model the Debye potential, the Boltzmann distribution is used, taken from statistical mechanics 2.3. The Boltzmann distribution describes the relative population of energy states W_j and W_k where g_j and g_k are their respective degeneracies. Assuming the point charge $Q+$ located at

the origin of the coordinate system generates a perturbed potential function $\phi_j(r)$, the population of charged particles that can overcome the generated potential is expressed as equation 2.4 [36]. This distribution is described by the Boltzmann Distribution where the subscript j indicates perturbed state and the subscript k indicates unperturbed state.

$$\frac{n_j}{n_k} = \frac{g_j}{g_k} \exp\Big(\frac{W_k - W_j}{k_B T}\Big) \tag{2.3}$$

$$n_j = n_k \exp\Big(\frac{-W_j}{k_B T}\Big) \tag{2.4}$$

For the respective ionic and electronic species:

$$n_e = n_{e0} \exp\Big(\frac{e\phi_j(r)}{k_B T}\Big) \tag{2.5}$$

$$n_i = n_{i0} \exp\Big(-\frac{e\phi_j(r)}{k_B T}\Big) \tag{2.6}$$

The high energy nature of plasmas allows for the assumption of high thermal energy, $k_b T$, relative to the perturbed potential $e\phi_j(r)$. This allows for a first order Taylor series approximation to eliminate the exponential, shown in equations 2.7 and 2.8 [36].

$$n_e = n_{e0}\Big(1 + \frac{e\phi_j(r)}{k_B T}\Big) \tag{2.7}$$

$$n_i = n_{i0}\Big(1 - \frac{e\phi_j(r)}{k_B T}\Big) \tag{2.8}$$

Relating the two distributions, electronic and ionic, can be done with the Poisson equation, equation 2.10, relating charge density to potential. The charge density, ρ, can be expressed as the sum of the two distributions n_e and n_i and the point charge $Q+$ expressed as a Dirac Delta [36].

$$\nabla^2 \phi = -\frac{\rho}{\epsilon_0} \tag{2.9}$$

$$\nabla^2 \phi = -\frac{1}{\epsilon_0}[Q\delta(r) - en_e + en_i] \tag{2.10}$$

Several assumptions can be applied at this point. The expressions for number density after perturbation derived from the Boltzmann Distribution allow for an expansion of the right hand side of the expression. Spherical symmetry can be assumed on the left hand side to simplify the Laplacian operator as well, resulting in equation 2.12 [36].

$$\frac{\delta^2\phi}{\delta r^2} + \frac{2}{r}\frac{\delta\phi}{\delta r} = -\frac{1}{\epsilon_0}[Q\delta(x) - en_{e0}\Big(\frac{e\phi(r)}{k_BT}\Big) - en_{i0}\Big(\frac{e\phi(r)}{k_BT}\Big)] \tag{2.11}$$

$$\frac{\delta^2\phi}{\delta r^2} + \frac{2}{r}\frac{\delta\phi}{\delta r} - \frac{1}{\lambda_D^2}\phi(r) = -\frac{1}{\epsilon_0}Q\delta(r) \tag{2.12}$$

Where

$$\frac{1}{\lambda_D^2} = en_{e0}\Big(\frac{e\phi(r)}{k_BT}\Big) + en_{i0}\Big(\frac{e\phi(r)}{k_BT}\Big) \tag{2.13}$$

From perturbation theory, an initial assumption to solve the Helmholtz differential equation in equation 2.12 is a mathematical perturbation $f(x)$ (not to be confused with the perturbed state mentioned earlier) of the Coulomb potential for a point charge [36]. The assumed solution takes the form of equation 2.15, with the limit of $r \in \mathbb{R} > 0$ [36].

$$\phi(x) = \frac{a}{r}f(r) \tag{2.14}$$

Within this range of $r \in \mathbb{R} > 0$, the Dirac delta of the point charge will be zero. This simplifies the differential equation 2.12 to:

$$f'' - \frac{1}{\lambda_D^2}f = 0 \tag{2.15}$$

This differential equation has solutions $f_1(r) = \exp(-r/\lambda_D)$ and $f_1(r) = \exp(r/\lambda_D)$. Applying a limit of $\lim_{r\to\infty} f(r) = 0$ means $f_2(r)$ can be dismissed as a trivial solution [36].

Gauss' Law can be applied to determine the scaling factor a. For when $r = 0 + \delta r$, The only charge contained by the surface A will be charge $+Q$. This allows for a first principles limit to be applied, $\lim_{r\to 0}\phi(r) = \frac{a}{r}$. As distance to the point charge drops, the influence of the outer charges becomes insignificant [36].

$$\oint_A E \quad dA = \frac{Q}{\epsilon_0} \tag{2.16}$$

Applying spherical symmetry (ie constant electric field along surface A), the electric field can be pulled out of the integral and related back to the electric potential through Gauss' Law.

$$\oint_A E \quad dA = 4\pi r^2 E = \frac{Q}{\epsilon_0} \tag{2.17}$$

$$E = \frac{Q}{4\pi r^2 \epsilon_0} \tag{2.18}$$

$$E = -\Delta\phi = \frac{a}{r^2}\left(1 + \frac{r}{\lambda_d}\right)\exp(-r/\lambda_D) \tag{2.19}$$

The limit of $\lim_{r\to 0} E = \frac{a}{r^2}$ can then be applied, giving a value for the scaling constant a.

$$\lim_{r\to 0} E = \frac{a}{r^2} = \frac{Q}{4\pi r^2 \epsilon_0} \tag{2.20}$$

$$a = \frac{Q}{4\pi\epsilon_0} \tag{2.21}$$

And thus

$$\phi(r) = \frac{Q}{4\pi\epsilon_0 r^2} e^{-r/\lambda_D} \tag{2.22}$$

This is the Debye-Huckle potential, and describes the spatial effect of Debye shielding [36]. An exponential decay of the traditional Coulomb potential caused by the localized presence of oppositely charged particles present in a plasma. This effect is characterized by the Debye length λ_D shown in equation 2.23. This value describes the combined shielding effects of electrons and ions in a plasma [36].

$$\lambda_D = \left(\frac{\epsilon_0 k_B T}{n_0 e^2}\right)^{-1/2} \tag{2.23}$$

Quasineutrality

The Debye self shielding results in positive and negative charges mixing amongst each other. Locally, the charge distributions create potentials as was outlined earlier. So on scales less than the Debye length, a plasma cannot be considered neutral on account of the charge disparities that arise. However on scales larger than the Debye length, a plasma is neutral as the shielding effects have enough space to take effect. Thus plasmas are considered quasi-neutral [36].

Plasma frequency

The Debye length gives a metric for collective plasma effects in space, and can be related to collective plasma effects in time. Electrons are significantly lighter than the heavy ionic species, and are accelerated much faster, so it is the negative charges that characterize how fast Debye shielding occurs. Working with the earlier assumption of low potential energy caused by the charge perturbation compared to the thermal energy of the plasma, the energy of an electron can be assumed to be completely thermal [36]. From kinematics, the time taken for an electron to establish a local Debye equilibrium will be on average the time taken to cross distance λ_{De}. The inverse of this time is known as the plasma frequency and can be seen in equation 2.24. In this expression, electron velocity is defined by equating thermal energy $k_B T$ to kinetic energy.

$$\omega_{pe} = \frac{\mathbf{u}_e}{\lambda_{De}} = \left(\frac{n_{e0} e^2}{\epsilon_0 m_e} \right)^{1/2} \tag{2.24}$$

This is the characteristic frequency at which plasma oscillations will arise. The migration of charges within a plasma creates charge disparities that oppose the migration, and draw back the charges. Treating the Debye potential as a harmonic oscillator will also lead to oscillations occurring at this plasma frequency [36].

$$f'' = -kf \tag{2.25}$$

$$\omega = \sqrt{\frac{k}{m}} \tag{2.26}$$

From equation 2.15 we know for our Debye system $k = 1/\lambda_D^2$ and from equation 2.23 the frequency of harmonic osculation of an electron in the Debye potential can be expressed as equation 2.27.

$$\omega = \left(\frac{n_{e0} e^2}{\epsilon_0 m_e} \right)^{1/2} \tag{2.27}$$

These two parameters, Debye length and plasma frequency, define a plasma and how collective behaviours propagate through it. The parameters are critical in understanding and developing models of plasma systems [36].

2.1.2 Magnetic field effects

Plasmas generate their own electric potentials and forces, as was examined in the previous section. The motion of charges also generates magnetic fields according to ampere's law. These self generated fields are often insignificant, and in the context of electric propulsion can almost always be ignored, with the exceptions of high current thrusters such as arcjets and pulsed plasma thrusters.

Lorentz force

To begin examined the effects of a magnetic field on a plasma, the logical starting point is the Lorentz Law, equation 2.28 [36].

$$\mathbf{F}_B = q\mathbf{u} \times \mathbf{B} \tag{2.28}$$

A magnetic field will exert a force perpendicular to the motion of a charged particle proportional to its charge. Breaking the equation down into Cartesian vectors results in equation 2.29.

$$\begin{aligned} \dot{u}_x &= u_y \frac{q}{m} B_z \\ \dot{u}_y &= -u_x \frac{q}{m} B_z \\ \dot{v}_z &= 0 \end{aligned} \tag{2.29}$$

Combining the equations of motion in the x-y plane results in a harmonic oscillator as seen in equation 2.30. The physical manifestation of this oscillator is a closed circular path. This circular path arises from the sinusoidal solution of equation 2.30 [36].

$$\dot{\mathbf{u}}_{x,y} = -\left(\frac{qB_z}{m}\right)^2 \mathbf{u}_{x,y} \tag{2.30}$$

From equation 2.26 the oscillation frequency can be determined for a moving particle in a magnetic field as seen in equation 2.31. This oscillation frequency is known as the cyclotron frequency [36]. The polarity of the charge will determine the direction of circling. The associated gyration radius is described in equation 2.32, and is known as the Larmor radius [36].

$$\omega_c = \frac{|q|}{m} B_z \tag{2.31}$$

$$r_L = \frac{u_\perp}{\omega_c} \tag{2.32}$$

$E \times B$ Drift

Combining the effects of electric and magnetic fields is important in understanding plasma behaviours. In Hall thrusters specifically, the electric and magnetic fields are perpendicular to each other. This creates some unique phenomena in the behaviours of charged particles and plasmas. As with the motion of a charged particle in a magnetic field, the natural starting point is developing equations of motion from the electrostatic force described in equation 2.33, a combination of the Lorentz and Coulomb forces at play. Assuming the crossed fields are composed of $\mathbf{B} = (0, 0, B_z)$ and $\mathbf{E} = (E_x, 0, 0)$ the Cartesian equations of motion are described in equation 2.34

$$\mathbf{F} = q(\mathbf{E} + \mathbf{u} \times \mathbf{B}) \tag{2.33}$$

$$\begin{aligned} \dot{u}_x &= \frac{q}{m}\Big(E_x + u_y B_z\Big) \\ \dot{u}_y &= -\frac{q}{m}\Big(u_x B_z\Big) \\ \dot{u}_z &= 0 \end{aligned} \tag{2.34}$$

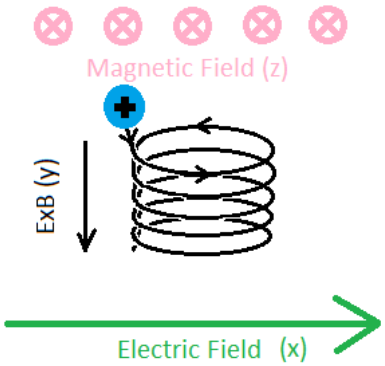

Figure 2.3: Mechanism of $E \times B$ drift

This system of differential equations is very similar to the system described by equation 2.29, with the addition of the electric field term. Unlike that system however, the combination of the equations of motion is not as simple. Substituting the derivatives in to simplify the system of differential equations into ordinary differential equations results in the following equations [36]:

$$\dot{u}_x = -\left(\frac{qB_z}{m}\right)^2 u_x \tag{2.35}$$

$$\dot{u}_y = -\left(\frac{qB_z}{m}\right)^2 (u_y + E_x/B_z) \tag{2.36}$$

These equations describe harmonic oscillation in the direction of the electric field as described by equation 2.35, and a more complex solution in the $E \times B$ direction as described by equation 2.36. This depicts a harmonic oscillator with an offset velocity [36]. This offset velocity is referred to as a drift velocity, and is pictured in figure 2.3

Hall effect

In the presence of crossed electric and magnetic fields, a single charged particle will generate no net current in the direction of the electric field. This changes in a bulk material. Collisions with other particles, neutrals ions or electrons, will reduce the kinetic energy of the particle in question. These reductions interrupt the cyclical motion in the x direction from figure 2.3,

and allow for the charged particles to move in the direction dictated by the Coulombic force being applied by the electric field [23]. In high density materials such as metallic conductors, these collisions are so numerous that the $E \times B$ drift can be neglected completely. In other materials, the $E \times B$ drift does not completely capture charged particles in the y, z plane, but significantly slows their progress through the electric field. This effect is known as the Hall effect [23].

The Hall effect in a bulk modulus is described in terms of currents. Defining current density $\mathbf{j}$ in terms of charge carrier number density n and velocity $\mathbf{v}$ gives equation 2.37. The resistance is described by momentum reducing collisions with neutral atoms in a lattice or gas, and mathematically is described by equation 2.38, where ν is the carrier-neutral collision frequency and m is the carrier mass [23].

$$\mathbf{j} = en\mathbf{u} \tag{2.37}$$

The resistance is described by momentum reducing collisions with neutral atoms in a lattice or gas, and mathematically is described by equation 2.38, where ν is the carrier-neutral collision frequency and m is the carrier mass. It is essentially a friction force opposing the motion of the charge carriers [23].

$$\mathbf{F}_f = -m\nu\mathbf{u} \tag{2.38}$$

Assuming the charge carriers have reached an equilibrium and are not accelerating, the forces can be balanced as in equation 2.39.

$$q(\mathbf{E} + \mathbf{u} \times \mathbf{B}) - m\nu\mathbf{u} = 0 \tag{2.39}$$

This results in Ohm's Law with the addition of the magnetic effects. Isolating the magnetic effects can be done by assuming a pseudo potential and associated electric field such that $E_{effective} = E_0 + E_H$ where $E_H = -\mathbf{u} \times \mathbf{B}$. Relating this back to the current density, equation 2.40 arises [23].

$$E_H = \mathbf{B} \times \mathbf{j}/en \tag{2.40}$$

This pseudo electrical field is referred to as the Hall field or Hall potential, and can be thought of as the equivalent electric field that would created a drift of the same speed as $E \times B$ drift in the same magnetic field. The magnitude

of this Hall potential is dependant on the strength of the magnetic field, and the neutral atom density. Higher densities will impede the oscillatory motion required for $E \times B$ drift, and thus reduce the drift velocity. A stronger magnetic field can counteract these effects by increasing the gyrofrequency, resulting in more oscillations before interruption [23]. In most solid materials, the neutral background density is too high for this effect to be of consequence. In plasmas however, the background density can be many orders of magnitude lower than in solids. This makes the Hall effect much stronger in some plasma applications, specifically low density plasmas such as those used in electric propulsion [23].

The strength of the Hall effect can be measured by the ratio of gyration periods to the interruptions to said gyrations. The interruption frequency will be the frequency of collisions with the background neutrals, earlier defined as ν. This ratio is known as the Hall parameter, and is described in equation 2.41.

$$\Omega_{Hall} = \frac{\omega_c}{\nu} = \frac{eB}{m\nu} \tag{2.41}$$

The Hall parameter is also the ratio of the velocities in the E and $E \times B$ direction. From equation 2.39, the velocity in the E direction will be:

$$u_x = \frac{eE_x}{m\nu} \tag{2.42}$$

And from equations 2.40 and 2.37 the velocity in the y direction will be as described in equation 2.43. This expression can then be rearranged to show the ratio of velocity in the direction of the electric field and in the $E \times B$ direction [36].

$$u_y = \frac{eBu_x}{m\nu} \tag{2.43}$$

$$\frac{u_y}{u_x} = \frac{eB}{m\nu} \tag{2.44}$$

2.1.3 Characteristic Length

There are several distinctions within plasmas that are useful in making regarding the interaction of particles within a plasma and the characteristic length of the plasma. With regards to the model developed in this thesis, the

distinction of a collisionless plasma and magnetized plasma are critical. The characteristic length of the plasma is the length of the region of interest, for this thesis that is the Hall thruster channel length.

Collisionless is an assumption negating collisions within a plasma. It assumes that the effects of collisions between particles of the same species are negligable. It is considered a valid assumption if one of two conditions is true [36]. The first is if the mean collision period is larger than the timeframe of interest of the plasma. This is not the case for Hall thrusters. The other condition is if the mean free path of collisions λ_{mfp} is larger than the characteristic length of the plasma L [36]. Given the mean free path defined by equation 2.45 [36], the mean free path of ion-ion collisions in Hall thrusters is on the order of $1 - 10m$ using an ion radius of $200pm$ and density of $1 \times 10^{19} m^{-3}$. This means that the ions can be treated as collisionless as the characteristic length $L \approx 1 - 10cm$ is significantly less than the mean free path of collisions $\lambda_{mfp} \approx 1 - 10m$.

$$\lambda_{mfp} = \frac{1}{n\pi r^2} \tag{2.45}$$

Magnetized plasmas are plasmas where magnetic effects are critical. They are characterized by the characteristic length and the gyroradius of the species within the plasma. If the Lamor radius is larger than the characteristic length of the plasma, than the plasma can be assumed to be unmagnetized, as magnetic effects will have little impact. Equation 2.32 defines the Lamor radius. For a Hall thruster operating at $300V$, a conversion of electric potential to kinetic energy can be used to re-write the expression as equation 2.46

$$r_L = \sqrt{\frac{2mV}{eB^2}} \tag{2.46}$$

For Xenon ions this yields a Lamor radius on the order of $r_L \approx 10 - 100cm$ which is larger than the characteristic length of the channel, so the ions can be considered unmagnetized. For electrons however, the Lamor radius is on the order of $r_L \approx 1 \times 10^{-4} - 1 \times 10^{-3} cm$, so magnetic effects on electrons must be modeled.

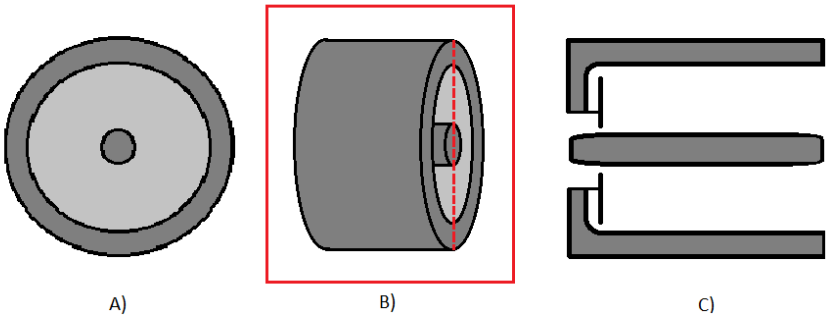

Figure 2.4: Diagrams depicting typical structure of an annular Hall thruster. A) Front view looking down the central propellant channel B) Isometric View C) Cross section of Thruster and propellant channel

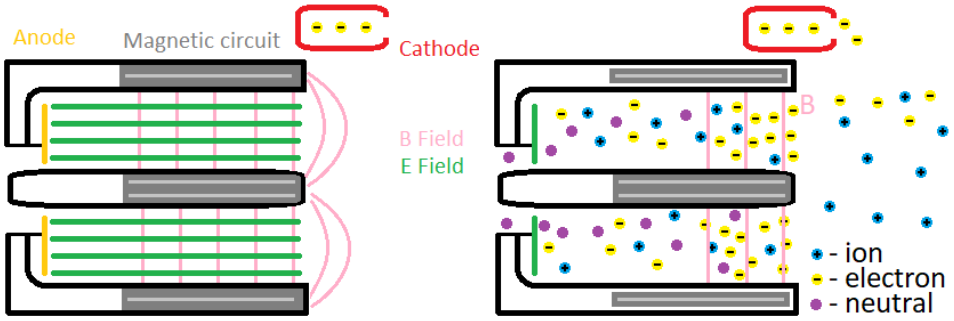

Figure 2.5: Left: Electric and magnetic field orientation in a Hall Thruster. Right: Plasma species distribution in a Hall thruster.

2.2 Design of Hall thrusters

Hall thrusters take advantage of the Hall effect, and the quasineutral nature of plasmas. The basic structure of a Hall thruster is a propellant channel with a gas emitting anode at the base, and a electron emitting cathode outside the channel. Typically Hall thrusters are annular in nature, as depicted in figure 2.4, although cylindrical variants without the central annulus are also common [47].

A magnetic circuit generates a field that is perpendicular to the propellant channel. The anode and cathode generate an electric field that is parallel to the channel, and consequently perpendicular to the magnetic field. The field orientations can be seen in figure 2.5.

The cathode supplies electrons, and anode supplies the propellant gas, typically Xenon. Under appropriate operating conditions, sufficiently strong magnetic field and low neutral gas density, the Hall effect can capture the emitted electrons in the $E \times B$ field. The $E \times B$ direction in this case is a circle around the central annulus of the thruster. With sufficiently strong fields, the Hall effect captures electrons in a toroidal current. This creates a local electron density that serves two purposes, ionization of the neutral propellant gas, and the generation of an electric field to accelerate the ions [36]. The much heavier ions have a gyrofrequency several orders of magnitude lower than the electrons, so the hall effect does not effect them in the same way. The ions are accelerated by the electric field to velocities on the order of $10 - 20km/s$ [36].

Debye shielding allows for a higher ion density in Hall thrusters compared to Ion thrusters that cannot sustain a quasineutral plasma if number density is too high. Traditional Hall thrusters can only be operated in space on account of the low neutral gas density required for the Hall effect to capture the electrons.

Design variables

There are several design variables that go into the design of a Hall thruster which can be divided into the categories geometric, electromagnetic, propellant, and performance related. These variables are outlined in table 2.2, and the geometric variables are depicted in figure 2.6. Fixed variables are inherent in the design stage, and cannot be modified in operation. Controlled variables can be modified during operation of the thruster, and dependant indicates a dependence on the other variables.

Hall thruster design variables			
Variable	Category	Notation	Dependence
Channel Length	Geometric	L	Fixed
Channel Width	Geometric	h	Fixed
Channel Radius Inner	Geometric	r_i	Fixed
Channel Radius Outer	Geometric	r_o	Fixed
Discharge Voltage	Electromagnetic	U_d	Controlled
Magnetic Field	Electromagnetic	$\mathbf{B}$	Fixed
Propellant Mass	Propellant	m	Fixed
Mass Flow Rate	Propellant	$\dot{m}_j$	Controlled
Discharge Current	Electromagnetic	I_d	Dependant
Thrust	Performance	T	Dependant
Specific Impulse	Performance	I_{sp}	Dependant
Power	Performance	P	Dependant
Exhaust Velocity	Performance	$\mathbf{v}$	Dependant
Thrust Efficiency	Performance	η	Dependant
Ionization Fraction	Performance	α	Dependant

Several relations can start to be constructed from these variables. Thrust, specific impulse, and mass flow rate can be related via equations 1.11 and 1.14. Thruster power can be be defined as the product of the discharge voltage and

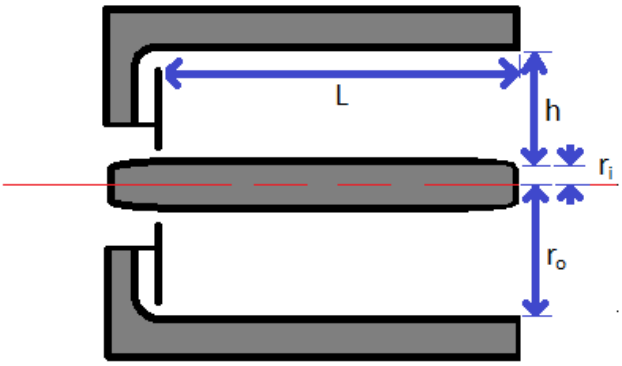

Figure 2.6: Geometric parameters in a Hall thruster

discharge current, and can be used to calculate the thrust efficiency of Hall thrusters, as in equation 2.48 [2].

$$P = U_d I_d \tag{2.47}$$

$$\eta = \frac{g I_{sp} T}{2P} \tag{2.48}$$

Relating all of these variables is a complex task. The channel geometry will affect the heat transfer and ionization occurring in the plasma. The mass flow rate will influence the neutral particle density and reaction rates as well as the particle mobility. Discharge current will be affected by the mobility of electrons in the plasma. The construction of an a-priori model to connect all of these variables is the focus of Chapter 3. Empirically, there are trends that arise in the design of low power Hall thrusters.

2.2.1 Miniaturization effects in Hall thrusters

Hall thrusters are very versatile propulsion units, able to provide the characteristic high specific impulse of electric propulsion at relatively high thrusts. There are some significant effects in the miniaturization of Hall thrusters. There are several factors that contribute to these effects, the most significant being the square cube law of geometric scaling. The square cube law dictates that with a geometric scaling factor α, the surface area of a geometry will change with a factor of α^2 and the volume with α^3. This has significant impact on Hall thrusters as different mechanisms depend on volume and surface area effects. Dannenmayer et. al. developed a series of scaling relations in Hall thrusters that were used to validate the model developed in this thesis [9].

Scaling down the power of Hall thrusters can be done in two ways, reduction in the discharge voltage or discharge current. Reducing the discharge voltage is straightforward, as it is one of the controlled inputs in a Hall thruster. Reduction in the discharge current is more complex. Due to the quasineutral nature of plasmas, the discharge current at steady state operation can be assumed to be a fraction of the mass flow rate in to the thruster, $I_d = \alpha \dot{m}$ [2]. Conservation of mass dictates that the mass flow in and out of the thruster must be equal, and quasineutrality means that no net charge can accumulate. Any charged particles leaving the thruster will be the fraction of fuel ionized in the thruster, and the discharge current will be equal to the charge flow rate

of this ion stream to neutralize it [2]. A reduction in the discharge voltage reduces the specific impulse of the thruster via a reduction in the exhaust velocity. Converting the electrical potential energy to kinetic energy, the change in specific impulse will be directly proportional to the root of the discharge voltage. A reduction in the discharge current requires a reduced mass flow rate in the thruster [2]. A reduction in the propellant mass flow rate will reduce the density of neutral atoms in the channel, and thus the frequency of ionization events.

$$I_{sp} \propto \sqrt{U_d}$$

Mathematically speaking, this gives a limit on thruster geometry. to ensure sufficient ionization occurs in the propellant, the mean free path of ionization must be significantly smaller than then channel length. This limit is known as the Melikov-Morozov criterion, and applies to all Hall thrusters. Equation 2.49 shows the Melikov-Morozov criterion in mathematical form, calculating the ionization mean free path from the neutral particle density, thermal velocities of the electrons and neutral species, and the ionization cross section for the propellant [2].

$$\lambda_i = \frac{v_n(T_n)}{n_n < \theta_i v_e >} << L \tag{2.49}$$

This presents the propellant utilization problem. Low power Hall thrusters need to either operate at reduced specific impulse or reduced propellant ionization fractions [2]. The reduction in propellant ionization fraction will also reduce the specific impulse, as the average exhaust velocity per unit mass of propellant will decrease.

$$L \propto \lambda_i$$

$$I_D \propto n_n \propto \dot{m}$$

In Hall thrusters, it is important to maintain a magnetic field strong enough to contain electrons in a Hall current, but not too strong that the ions are contained as well. The Larmour of the various particles is a good measure of how effectively trapped they are. If the Larmour radius is significantly smaller than the channel Length, then the particles are effectively trapped, and if it it larger than the channel length they are not trapped. This leads to the following inequality in equation 2.50. The Larmour radius of the electrons

has to be significantly smaller than the channel length, which in turn has to be significantly smaller than the ion Larmour radius.

$$r_{Le} << L << r_{Li} \tag{2.50}$$

Given the inverse relation of the Larmour radius to the magnetic field strength outline in equation 2.32, it can be determined that as a thruster scales down geometrically, the magnetic field must scale proportionally in the other direction, i.e. if the length is halved, the magnetic field must double in strength [9].

The magnetic field strength is also coupled to the neutral number density. For the Hall current to form, it is required that the neutral particle collision frequency is significantly lower than the cyclotron frequency [9]. The cyclotron frequency is directly proportional to the magnetic field strength. The neutral gas density, being drive by a gas expansion, is dependant on the mass flow rate and the cross sectional area of the channel as depicted in equation 2.52 [9].

$$\omega_c >> \nu_n \tag{2.51}$$

$$\dot{m}_n = n_n m_n v_n A \tag{2.52}$$

As the cross sectional channel area scales down, the magnetic field must scale up accordingly to maintain a high Hall parameter [9]. Alternatively, the mass flow rate could be scaled down but that introduces a limit on thrust and specific impulse.

$$B \propto \frac{1}{L}$$

$$B \propto \frac{1}{h(r_i - r_0)}$$

Equation 1.11 shows the thrust force of a rocket propulsion system as a product of the exhaust velocity and mass flow rate at said velocity. Converting electrical potential energy to kinetic energy, the exhaust velocity of the ions will scale with the square root of the discharge voltage [9]. The thrust also depends on the mass flow rate of the ions, distinct from the mass flow rate of the propellant. From the Melikov-Morozov criterion outlined earlier, it is

known that the ionization fraction scales with the thruster channel length. Accordingly, thrust will also scale with channel length [9].

$$T \propto \dot{m}\sqrt{U_d}$$

Dannenmayer et. al. determined scaling coefficients for these laws empirically [9]. As part of the validation of the numerical model in this thesis, these scaling coefficients will be determined through the numerical model and compared to the values determined by Dannenmayer to define the range of accuracy of the simulation.

2.2.2 Summary of Scaling Laws in Hall Thrusters

These scaling laws give a more in depth understanding of how Hall thrusters work, and allow for modification of the thruster to achieve the design goals.

$$I_{sp} \propto \sqrt{U_d}$$

$$L \propto \lambda_i$$

$$B \propto \frac{1}{L}$$

$$B \propto \frac{1}{h(r_i - r_0)}$$

$$T \propto \dot{m}\sqrt{U_d}$$

$$r_{Le} << L << r_{Li}$$

$$\omega_c >> \nu_n$$

$$I_D \propto n_n \propto \dot{m}$$

These scaling laws, while useful, are not a substitution for an in depth numerical model. Chapter 3 outlines the design of the RAPPEL Hall Simulation software that is used in conjunction with these scaling laws to design and analyze low power Hall thrusters.

2.3 Research Goals

The goal of this thesis is to present the development and testing of a first principles numerical model of a low power Hall thruster intended for use as an engineering design tool. For context, microsatellites and low power propulsion systems are increasing in demand, and the ability to analyze designs before construction allows for a streamlined design process. This thesis will define and validate the model, present findings on its precision and accuracy as a design tool through literature comparisons of experimental and numerical characterizations of Hall thrusters. The numerical model, referred to as the RAPPEL Hall Simulation (RHS), was used to examine the operation of a dual stage cylindrical Hall thrsuter. This thesis examines how several different models of anomalous electron transport in fluidic electron models scale with thruster dimensions and power, and additionally aims to provide insight into the operation of a multistage Hall thruster for small spacecraft.

3 Numerical Model Design: Hall Thrusters

As plasmas exist in many diverse environments and structures, the modeling of plasmas is also diverse in nature. Modeling the nuclear fusion plasmas in tokamaks and stellar cores is going to be very different from modeling the arc discharges of lightning or glow discharges. The design of a model appropriate for the highly magnetized, low temperature, low density plasmas in Hall thrusters is the focus of this section.

Modeling a plasma could be done by comprehensively calculating the exact location and velocity of every ion, neutral atoms, and electron in a plasma. In a Hall thruster though, expected plasma densities are on the order of 1×10^{18} electrons $/m^3$, so from a computational point of view this approach is not only highly impractical, but almost impossible on account of the amount of RAM required. Simplification is required, and ranges from grouping individual particles together into macroparticles that represent hundreds or thousands of particles, to treating the plasma as a fluid and applying fluid-dynamics principles [8].

There is a trade-off in accuracy versus simplicity as these simplifying assumptions are made. A magnetohydrodynamic code will treat the entire plasma as a single fluid, but will not capture plasma structures that form or some of the other bulk behaviours exhibited by plasmas. Combinations of models can be used as well, splitting the heavy ionic species and treating it differently from the light electronic species is common practice on account of the significant difference in mass between electrons and ions [8].

In terms of Hall thrusters, there are several common approaches to numerical models. These include full kinetic models for investigating plasma

behaviour in the thruster, full fluid models for examining the thruster performance, and hybrid fluid-PIC methods for thruster performance and simplified reactions [42]. As a design tool, the hybrid approach excels. It offers a significantly lower computational cost than a full kinetic approach for simulating plasma systems. It lacks the accuracy to examine some of the less understood phenomena in Hall thrusters however [42]. The modeling of chemical reactions in a hybrid scheme is simpler than in a full fluid scheme, as reactions can be handled on a particle-per-particle basis as opposed to calculating bulk reaction rates and applying them as source coefficients. As the research goal of this project is to develop a tool for the design and simulation of low power hall thrusters, the Hybrid scheme fits best on account of the relatively low computational cost and simpler implementation of chemical reactions.

The model outline can be seen in figure 3.1. The simulation was created in MATLAB and was original work done for this thesis. The physics at play in Hall thrusters is complex and multifaceted. As such, there is a high degree of interaction between the various modules of the simulation program. This chapter will outline the approach to physical modelling taken in the development of the RAPPEL Hall Simulation Software, and justify the decision made as part of that process.

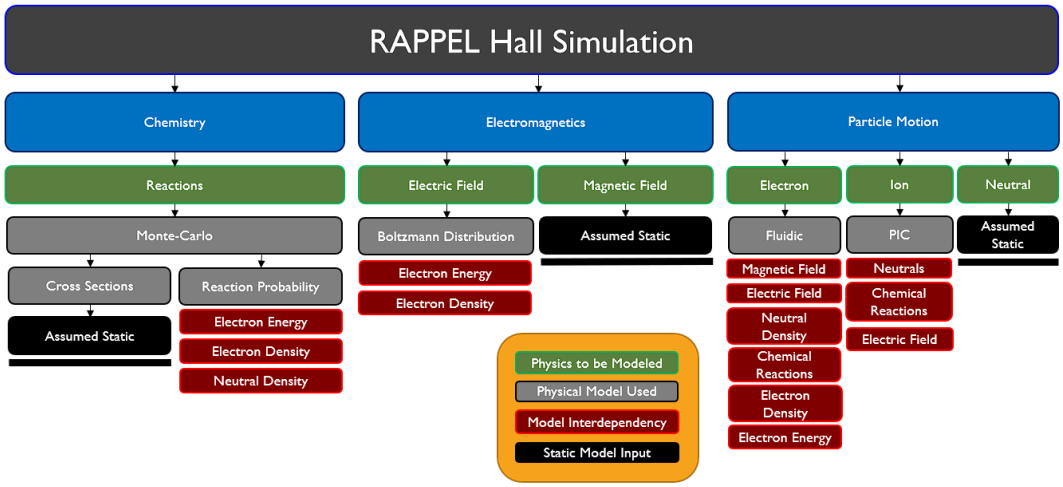

Figure 3.1: Outline of the RAPPEL Hall Simulation

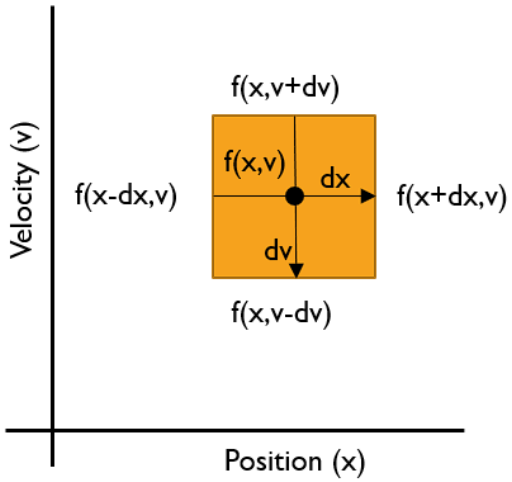

Figure 3.2: Graphical Depiction of Boltzmann Equation in Phase Space

3.1 Boltzmann Equation

The Boltzmann equation, equation 3.1, models a distribution of particles in a Newtonian system. The Boltzmann Equation arises from conservation of mass in a 6 dimensional phase space, 3 spatial and 3 velocity dimensions. Change in the velocity dimensions is driven by external force **F** and change in the spatial dimensions is driven by the velocity v. Collisions can introduce or remove particles, and are accounted for in the Boltzmann Equation with the collision term on the right hand side. Conservation of mass dictates that the net number of particles must be conserved [8]. The solution to the Boltzmann Equation is a distribution function, a function that depicts the spatial and velocity distribution of the particles in the system.

$$\frac{\partial f}{\partial t} + \mathbf{v}\frac{\partial f}{\partial x} + \frac{\mathbf{F}}{m}\frac{\partial f}{\partial \mathbf{v}} = \frac{\partial f}{\partial t}_c \tag{3.1}$$

Models that solve the Boltzmann Equation for each particle and keep track of the position and motion of the system are referred to as kinetic or PIC models.

3.2 Particle-in-cell ionic species

The heavy ionic species in the RHS was represented with a PIC appraoch. The heavy ionic species was assumed to be unmagnetized and collisionless. The gyroradius of the ions would be significantly larger than the characteristic length of the channel, $r_i >> L$, and the mean free path of heavy species collisions is also larger than the channel length $\lambda_i >> L$ [4]. These characteristics make the modeling of the ionic species much simpler than the electron species. Magnetic effects can be ignored, as well as diffusive properties and pressure terms. The result is a charged particle species that reacts to an electric force [8].

To reduce the computational load, macroparticle representation was used. As mentioned previously, a macroparticle represents the motion of multiple actual particles. One Xenon ion macroparticle will represent millions of actual ions. The charge to mass ratio of the macroparticle will remain the same as the original ions it represents. Acceleration of the macroparticle will thus remain the same as the acceleration of an ion in the same electric field, proportional to the charge and inversely proportional to the mass [8].

For a kinetic particle in cell (PIC) species, the particle position and velocity are tracked and updated with each timestep based on the forces being applied. The one dimensional nature of the simulation being developed for this thesis greatly simplifies the equations of motion, which can be seen in equations 3.2 to 3.4 [8].

$$x_2 = x_1 + v\Delta t \tag{3.2}$$

$$v_2 = v_1 + a\Delta t \tag{3.3}$$

$$a = \frac{q}{m}\mathbf{E} \tag{3.4}$$

This forward difference method is inherently unstable however, so a central difference method in time is used instead, averaging the electric field to accelerate ions with each timestep. The nature of this instability is outlined in chapter 6. The limits on stability in the central difference scheme are resolving the Debye length on a spatial scale and plasma frequency on a temporal scale [8].

$$x_{n+1} = x_n + v_{n+1/2}\Delta t \tag{3.5}$$

$$v_{n+1/2} = v_{n-1/2} + a\Delta t \tag{3.6}$$

To abide by this limit for the electronic species as well as the ionic/neutral species, the timestep would need to be on the order of 1×10^{-12} s. As Hall thrusters require 4×10^{-6} s to ignite, this would be a very intense computational load. To circumnavigate this issue, the electrons were modeled with a different approach.

3.3 Drift-diffusion electron model

Fluid models of a plasma assume that the plasma is in thermodynamic equilibrium with itself, and that characteristics such as density, temperature, and energy form a continuous distribution throughout the plasma. This requires sufficient interaction of the plasma particle with one another. Given a cube with side length equal to the Debye length, a fluid model can be considered appropriate if the number of particles in such a cube is significantly greater than 1 [8]. This is the case for Hall thrusters.

In a fluid approximation, the assumption of a thermodynamic distribution of electrons in an EEDF allows for integration over the velocity space, simplifying the Boltzmann Equation from a 6D PDE to a 3D PDE [36]. This simplification takes the form of assuming an electron energy distribution function, allowing electron energy to be represented by an average electron energy, and using the assumed energy distribution of electrons around that average to calculate transport parameters.

3.3.1 Electron Energy Distribution Function

The Electron Energy Distribution function, or EEDF is what allows for a fluid model of the electrons to be implemented. Assuming that the electron energy has a probabilistic distribution around a given average energy allows for the model to keep track of that average energy, rather than attempt to model the energy of each particle individually in a Vlasov or PIC scheme. For this model, a Maxwellian-Boltzman distribution was assumed, taking the form of equation 3.7 [29].

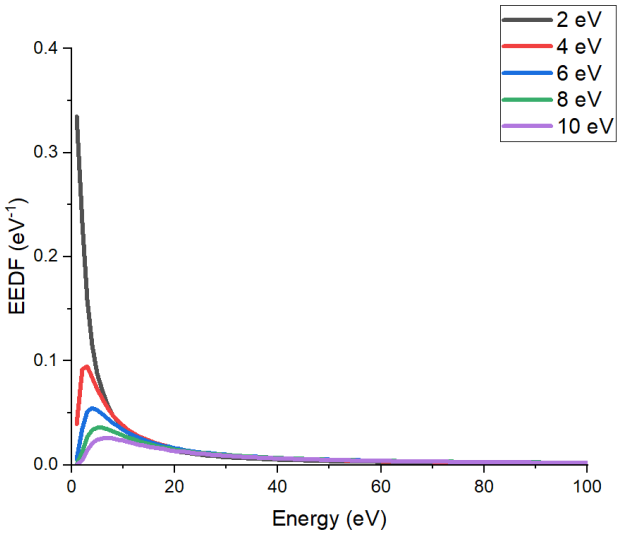

Figure 3.3: Numerically calculated Maxwellian electron energy distribution for given average energy ϵ

$$P(E) = \epsilon_e^{-3/2}\Gamma_\infty(5/4)^{3/2}\Gamma_\infty(3/2)^{-5/2}e^{(-E\Gamma_\infty(5/2)\Gamma_\infty(3/2)^{-1}/\epsilon_e)} \tag{3.7}$$

Where Γ_∞ is the incomplete gamma function [29]. This distribution can be seen graphically in figure 3.3. The average energy of the distribution modifies the distribution itself, a result of increased energy diffusion at higher energies [29].

Other electron energy distributions exist and are used by plasma models, but for Hall thrusters a Maxwellian-Boltzmann distribution is sufficient [5]. Other distributions include Druvenstyn and Mixed electron distributions [29].

The solution to the Boltzmann Equation is defined as a distribution function f. When f is integrated over velocity space, simplified greatly by an assumed electron energy distribution function, it gives the electron number density n. When f is multiplied by the average velocity of each particle in the distribution then integrated, it gives momentum, $n\mathbf{u}$. The electron energy, density $n\epsilon$ can be calculated by integrating over the velocity space and multiplying by the average velocity squared [42].

$$n = \int f(x, \mathbf{v}, t) \quad d^3\mathbf{v} \tag{3.8}$$

$$\mathbf{u} =< v >= \frac{1}{n} \int \mathbf{v} f(x, \mathbf{v}, t) \quad d^3\mathbf{v} \tag{3.9}$$

$$\epsilon = \frac{m}{2e} < v >^2 = \frac{m}{2en} \int v^2 f(x, \mathbf{v}, t) \quad d^3\mathbf{v} \tag{3.10}$$

As integrating the distribution function f over velocity space gives the number density distribution, The same integration of the Boltzmann Equation yields an expression for the conservation of those particles, or the conservation of mass. This is referred to as the continuity equation and is seen in equation 3.11 [42].

$$\frac{\partial n}{\partial t} + \nabla(n\mathbf{u}) = S_c \tag{3.11}$$

Where S represents a source term. This source term represents the particles gained/lost to collisions. With knowledge of the velocity distribution, the number density in the simulation domain can now be solved for. To get this information, another conservation law is applied. Rather than conservation of mass across a boundary, conservation of momentum can be applied. This is done as simply as multiplying the Boltzmann Equation by the velocity distribution, and integrating over velocity space [42]. This results in a momentum continuity equation, equation 3.12.

$$\frac{\partial \mathbf{u}}{\partial t} + (\mathbf{u}\nabla)\mathbf{u} = \frac{e}{m}(\mathbf{E} + \mathbf{u} \times \mathbf{B}) - \frac{e}{mn}\nabla(nT) - \nu\mathbf{u} - S_c \tag{3.12}$$

3.3.2 Electron Flux

At this point it is useful to relate the momentum continuity equation 3.12 back to the continuity equation 3.11. This is done by the introduction of the electron flux parameter, defined in equation 3.13 [18].

$$\Gamma = n_e \mathbf{u}_e \tag{3.13}$$

Due to the low mass of electrons, the inertial term can be neglected. The electron temperature can also be expressed as $2/3\epsilon_e$ [42]. These assumptions allow for equation 3.12 to be re written in terms of electron flux as equation 3.14 after being multiplied by the number density, n_e, as well as the omission of source terms. This can be recognized as the drift diffusion equation [42].

$$\Gamma = n_e \mathbf{u}_e = -\frac{e}{m_e \nu_e} n_e (\mathbf{E} + \mathbf{u} \times \mathbf{B}) - \frac{2}{3} \frac{e}{m_e \nu_e} \nabla (n_e \epsilon_e) \tag{3.14}$$

Equation 3.14 forms the basis of the drift-diffusion model of plasmas. The flux is characterized by two terms, the electromagnetic driven drift and the thermal driven diffusion. Once the flux is calculated, it can be used to calculate the change in number density. The diffusion is characterized by a diffusion coefficient, and drift characterized by an electron mobility coefficient [42].

3.3.3 Electron mobility and diffusivity

Electron mobility, defined in equation 3.15, is defined as the ratio of the terminal velocity an electron can achieve in a medium to the electric field being applied to accelerate the electron [36]. The acceleration from the electric field with be proportional to the charge to mass ratio of the electron, and it will lose its speed whenever it hits a heavy species, ionic or neutral. From kinematics we can then average the speed to be the product of the charge to mass ratio and the time between heavy species collisions [36]. This allows for a simplification of equation 3.14.

$$\mu_{de} = \frac{\mathbf{u}_e}{\mathbf{E}} = \frac{e}{m_e \nu_{m,e}} \tag{3.15}$$

The Einstein relation, equation 3.16, was used to relate the diffusion coefficient to the electron mobility [11]. There are multiple approaches to the calculation of the diffusion coefficient however, some involve solving the Boltzmann equation directly, where others, such as the Einstein relation, assume an electron energy distribution function (EEDF). The Einstein relation assumes a Maxwellian EEDF [11], which is proven to be accurate in Hall thruster models [5] [18].

$$D = \frac{2}{3} \mu T \tag{3.16}$$

These two transport coefficients simplify the drift diffusion equation to equation 3.17.

$$\Gamma = -\mu n_e(\mathbf{E} + \mathbf{u} \times \mathbf{B}) - \nabla(Dn_e) \tag{3.17}$$

This calculation still requires the cross product of the velocity and magnetic field to be calculated. To avoid this, the magnetic field effects can be combined with the electron mobility term to form a non-isotropic electron mobility term [36]. This results in the electron mobility tensor described in equation 3.18. This tensor is constructed by using Ohm's Law described in chapter 2.3.3 to express the $E \times B$ product in terms of the electric field, and factor out the constants.

$$\boldsymbol{\mu}_e^{-1} = \begin{bmatrix} \frac{1}{\mu_{de}} & -B_z & B_y \\ B_z & \frac{1}{\mu_{de}} & -B_x \\ -B_y & B_x & \frac{1}{\mu_{de}} \end{bmatrix} \tag{3.18}$$

This tensor allows for the drift diffusion equation to be again re written as seen in equation 3.19.

$$\Gamma = -n_e \boldsymbol{\mu}_e \mathbf{E} - \nabla(Dn_e) \tag{3.19}$$

To simplify this relation to one dimension, the Hall parameter was used to relate the axial and transverse velocities to allow for an expression of a scalar electron mobility that accounts for the Hall effect [27]. This requires assuming the perpendicular electric field is negligible, $E_y = 0$. This gives rise to equations (3.21) and (3.22).

$$\mathbf{E} = \mu_e^{-1} \cdot \mathbf{v} \tag{3.20}$$

$$\mathbf{E} = \begin{bmatrix} \frac{1}{\mu_{de}} & -B_z & 0 \\ B_z & \frac{1}{\mu_{de}} & 0 \\ 0 & 0 & \frac{1}{\mu_{de}} \end{bmatrix} \cdot \begin{bmatrix} v_x \\ v_y \\ v_z \end{bmatrix} \tag{3.21}$$

$$\mathbf{E}_x = v_x \frac{m_e \nu_m}{q} - v_y B_z \tag{3.22}$$

$$\mathbf{E}_x = v_x \frac{m_e \nu_m}{q} - \Omega_{Hall} v_x B_z \tag{3.23}$$

$$\mu_{e,x} = \frac{e}{m_e \nu_m} \frac{1}{1 + \frac{\omega_e^2}{\nu_m^2}} \tag{3.24}$$

Thus the electronic flux can be written as equation 3.25:

$$\Gamma = -n_e \mu_x E - \nabla(D n_e) \tag{3.25}$$

The last variable to be defined in this mobility model is the electron-neutral collision frequency, ν_m. This is defined by taking the electron-neutral elastic collision cross section and multiplying it by the neutral density and relative electron velocity, as defined in equation 3.26 [44]. The cross section is an empirically determined constant, for Xenon it takes on a value of $2.7 \times 10^{-19} \mathrm{m}^{-3}$.

$$\nu_m = n_n \theta_{en} \sqrt{\frac{8kT_e}{\pi m_e}} \tag{3.26}$$

The drift diffusion model is composed of the electron flux, the electron mobility, and the Einstein relation. To close the system, the electron temperature must still be calculated.

3.3.4 Electron energy flux

The electron temperature is defined by the electron energy distribution function and the average electron energy distribution defined in equation 3.10. Multiplying the Boltzmann Equation by $mu^2/2$ gives an energy continuity equation 3.27 [42]. This integration of the Boltzmann equation is outlined by Hagelaar et al. [18] and assumes a Maxwellian electron energy distribution.

$$\frac{\partial(n_e \epsilon_e)}{\partial t} + \frac{5}{3} \nabla n_e \mathbf{u}_e \epsilon_e - \frac{10}{9} \nabla(n_e \epsilon_e \mathbf{u}_e \nabla \epsilon_e) + n_e \mathbf{u}_e \mathbf{E} = -S_c \tag{3.27}$$

Using the flux defined in equation 3.25 this expression can be simplified.

$$\frac{\partial n_e \epsilon_e}{\partial t} + \frac{5}{3} \epsilon_e \nabla \Gamma + \mathbf{E}\Gamma = -S_c \tag{3.28}$$

To simplify this relation, it is useful to define an electron energy flux Γ_ϵ and associated transport coefficients, equations 3.29 through 3.31 [18]:

$$\Gamma_\epsilon = -n_e \epsilon_e \mu_\epsilon \mathbf{E} - \nabla(D_\epsilon n_e \epsilon_e) \tag{3.29}$$

$$\mu_\epsilon = \frac{5}{3} \mu \tag{3.30}$$

$$D_\epsilon = \frac{5}{3} D \tag{3.31}$$

The electron energy density can then be expressed as the solution to equation 3.32. The average electron energy ϵ_e relates directly to the electron temperature via the expression previously used, $T = 2/3\epsilon_e$ [18].

$$\frac{\partial n_e \epsilon_e}{\partial t} + \nabla \Gamma_\epsilon + \mathbf{E}\Gamma = -S_{c\epsilon} \tag{3.32}$$

3.3.5 Electron model summary

The drift diffusion model is therefore characterized by the following equations:

$$\frac{\partial n_e}{\partial t} + \nabla \Gamma = -S_c \tag{3.33}$$

$$\Gamma = -n_e \mu_x E - \nabla(D n_e) \tag{3.34}$$

$$\mu_{e,x} = \frac{e}{m_e \nu_m} \frac{1}{1 + \frac{\omega_e^2}{\nu_m^2}} \tag{3.35}$$

$$\nu_m = n_n \theta_{en} \sqrt{\frac{8kT_e}{\pi m_e}} \tag{3.36}$$

$$D = \frac{2}{3} \mu T \tag{3.37}$$

$$\Gamma_\epsilon = -n_e \epsilon_e \mu_\epsilon E - \nabla(D_\epsilon n_e \epsilon_e) \tag{3.38}$$

$$\mu_\epsilon = \frac{5}{3} \mu \tag{3.39}$$

$$D_\epsilon = \frac{5}{3} D \tag{3.40}$$

$$\frac{\partial n_e \epsilon_e}{\partial t} + \nabla \Gamma_\epsilon + \mathbf{E}\Gamma = -S_{c\epsilon} \tag{3.41}$$

This model assumes a Maxwellian electron energy distribution function. More accuracy can be gained through implementing Boltzmann Solvers that will calculate the EEDF through approximated solutions, but the assumption and accuracy of a Maxwellian EEDF is well documented and supported by literature [18][42][5]. The numerical model now accounts for the transport of electrons and ions through time and space, but in plasmas ions and electrons appear and disappear based on chemical reactions within the plasma. These are accounted for with a Monte-Carlo Scheme.

3.4 Monte-Carlo-Collisions

The Monte-Carlo-Collision method (MCC) is based on generating random numbers and comparing them to a probability distribution to determine an outcome. In the context of the simulation that was developed in this thesis, the Monte Carlo scheme is used to determine when chemical reactions occur. The reaction probabilities are determined by cross sections sourced from Rapp [38], species densities, and species energies. The probabilities are calculated by equation (3.42) as given by Birdsall [8], where P is the probability between 1 and 0, n_n is the target species density, v_r is the relative velocity between the particles, $\theta_{[\phi]}$ is the energy dependant cross section, and Δt is the timestep. The program cycles through each macroparticle and calculates the probability of each reaction.

$$P = 1 - e^{-n_n v_r \theta_\phi \Delta t} \tag{3.42}$$

If the randomly generated number is less than the probability for a given macroparticle, the particle is flagged and the appropriate reaction is performed. Macroparticles are converted from one species to the other with their respective reactions. The position and velocity of the ion/neutral as it changes species is unchanged as the reaction occurs [8]. Tables 3.1 and 3.2 show the species being reacted and the modeled reactions respectively.

Table 3.1: Plasma species

Species	**Symbol**	**Type**
Electron	e	Electron
Xenon	Xe	Neutral
Xenon ion	Xe+	Ion

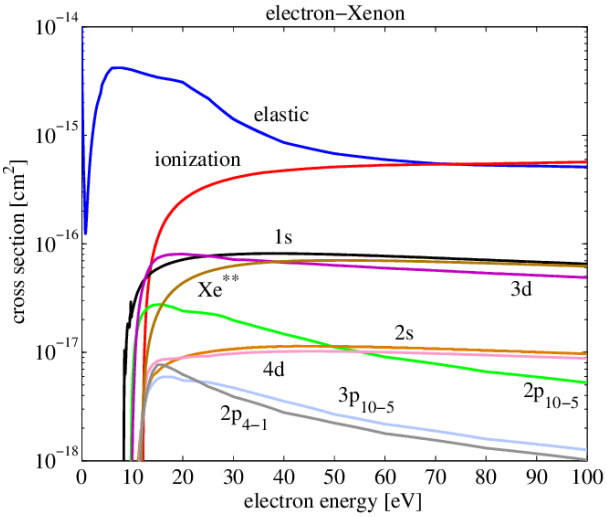

Figure 3.4: Various reaction cross sections for Xenon (Taken from [3])

Table 3.2: Collision reactions

Reaction	**Parameters**	**Type**
e+Xe → 2e+Xe+	Cross section	Ionization
e+Xe+ → Xe	Cross section	Recombination

As these reactions are flagged on each macroparticle, the electron density and electron energy density are updated accordingly. For each macroparticle ionized, an appropriate amount of electrons are injected into the electron distribution function at the ionization energy of Xenon. The same is done for neutralization. This accounts for the source terms from the drift diffusion model that were neglected earlier.

To close the system, the electric and magnetic fields need to be defined, and the boundary conditions of the system.

3.5 Electric and magnetic fields

3.5.1 Electric Fields

There are several approaches to calculating self consistent electric fields within a plasma as it applies to Hall thrusters. The two most commonly used

include a Poisson Equation Solver that solves Gauss's Law, and a quasineutrality assumption that allows for the electric potential, and thus electric field, to be calculated from the plasma number density.

Gauss's Law Approach: Poisson Solver

In this method of determining electric fields, the potential is calculated from the charge density via Gauss's law. To determine the net charge density, the ions were sorted into cells and that sum was divided by the volume of each cell. The electron density was subtracted from this ion number density, and the resulting distribution was multiplied by the elementary charge e to get a charge distribution ρ [6]. Gauss's law was applied to get an electric potential which was subsequently converted to an electric field [6]. Mathematically, this process takes the form of the Poisson Equation, and is seen in equation 3.43.

$$\nabla^2\phi = -\frac{\rho}{\epsilon} \tag{3.43}$$

$$\frac{\phi_{i+1} - 2\phi_i + \phi_{i-1}}{\Delta x^2} = -\frac{\rho}{\epsilon} \tag{3.44}$$

The numerical solution to the Poisson equation uses a finite difference scheme to relate the potential to the change in charge density. Equation 3.44 shows a central difference discretization of the Poisson Equation. A discretized matrix can be formulated to calculate the potential via matrix multiplication to reduce the computational load of the simulation, as seen in equation 3.45. The matrix will be $n \times n$, where n is the number of cells in the simulation domain [6].

$$P = \begin{bmatrix} 2 & -1 & 0 & 0 & \cdots & 0 \\ -1 & 2 & -1 & 0 & \cdots & 0 \\ 0 & -1 & 2 & -1 & \cdots & 0 \\ \vdots & \ddots & \ddots & \ddots & \ddots & \vdots \\ 0 & 0 & \cdots & -1 & 2 & -1 \\ 0 & 0 & \cdots & 0 & -1 & 2 \end{bmatrix} \tag{3.45}$$

The introduction of this discretization matrix simplifies the otherwise complex task of solving this system of equations. Without the discretized matrix, an iterative Newtonian solver could be used.

$$-\frac{1}{\Delta x^2}\boldsymbol{\phi}\mathbf{P} = \frac{\rho}{\epsilon} \tag{3.46}$$

$$\mathbf{P}\boldsymbol{\phi} = -\frac{\Delta x^2}{\epsilon}\rho \tag{3.47}$$

Quasineutrality presents an issue with this approach. At scales larger than the Debye length, equation 3.48, there should be be effectively zero charge density as the space will be neutral. This presents a limit on the spatial discretization of the simulation; $dx \leq \lambda_D$

$$dx \leq \lambda_D = \left(\frac{\epsilon_0 k_B T}{n_0 e^2}\right)^{-1/2} \tag{3.48}$$

Quasineutral Approach: Boltzmann Distribution

The other method for determining self consistent electric fields within a plasma uses the assumption of quasineutrality and the Boltzmann Distribution described in equation 2.3.

$$n_e = n_{e0} \exp\left(\frac{e\phi_e(r)}{k_B T}\right) \tag{3.49}$$

This equation can be rearranged for the electric potential, replacing the $k_B T$ term with the average electron energy:

$$\phi_e(r) = \frac{2}{3}\epsilon_e \ln\left(\frac{n_e}{n_{e0}}\right) \tag{3.50}$$

This expression gives the plasma potential generated by the plasma. It requires a reference density to calculate this potential however. The Boltzmann Relation was derived earlier in chapter 2 with perturbation theory, assuming a uniform density to begin with and applying changes after the fact [36]. This expression for potential has the same underlying assumptions, a bulk density that will not contribute to the change of potential, and any variation from that will modify the potential accordingly.

This equation captures the plasma potential, but not the addition of the discharge potential applied by the anode in a Hall thruster. This can be incorporated easily through the principle of superposition by adding the two potentials together;

$$\phi(r) = \phi_a(r) + \phi_e(r) \tag{3.51}$$

$$\phi(r) = \phi_a(r) + \frac{2}{3}\epsilon_e \ln\left(\frac{n_e}{n_{e0}}\right) \tag{3.52}$$

where $\phi_a(r)$ is the static potential generated by the anode - cathode potential difference.

Both of these methods, quasineutral and Poisson, were included in the simulation software and tested for efficiency and accuracy. The hybrid nature of the simulation lead to artificially increased localized charge densities, and it was postulated that this caused the Poisson solver to overestimate the electric fields generated by the plasma. For this reason, the Quasineutral approach was taken. It also happens to be significantly simpler and faster than the Poisson approach, likely on account of not needing to solve an entire system of equations.

3.5.2 Magnetic Fields

The simulation applied a static magnetic field profile as an input from the Finite Element Methods Magnetics software. The FEMM simulations return a 2D magnetic field profile based on material properties [30]. For the 1D simulation, a 1D profile was generated by taking the perpendicular field component in a line parallel to the thrust axis at the channel midpoint. Any internally generated magnetic fields within the plasma are negligible compared to the static externally generated field.

3.6 Neutral species

The background neutral species was assumed to stationary for the purposes of this simulation. The relative motion of neutrals compared to ions and electrons makes this assumption commonplace in the modeling of Hall thrusters [5]. An initial distribution needs to be generated however. This was done by running a preliminary simulation that introduces the neutral macroparticles at a Maxwellian thermal velocity distribution at the anode, and uses a Direct-Simulation-Mote-Carlo approach, DSMC. Starfish PIC was used for this initial neutral gas expansion [6]. Similarly to the MCC method used for the chemical reactions, DSMC generates random numbers upon particle interactions.

DSMC models scattering reactions between a single species as opposed to the chemical reactions of MCC. When two particles collide, a random number generator establishes new paths for each particle [6]. The neutral solver was run in 2 dimensions and a central 1D profile extracted. The neutral gas expansion simulation was run on a much courser timestep on account of significalntly lower velocities than the plasma simulation. The neutral macroparticles serve as the source of ions for the plasma simulation.

3.7 Secondary Electron Emission

Secondary electron emission (SEE) is the process of an incident ion or electron displacing an electron in the dielectric material that forms the channel walls of a Hall thruster. It is a significant electron source in Hall thrusters, and accordingly should be modeled.

In 2D and 3D models, Wall currents are calculated as part of the Wall boundary condition and used to determine the secondary electron yield. In 1D models, as the one developed for this thesis, this current cannot be easily calculated. Instead, many 1D models will use an electron-wall collision frequency to calculate the secondary emission yields [42].

Modeling the secondary emission coefficient relies on the secondary emission coefficient parameter γ. This parameter is a material characteristic that outlines the number of secondary emitted electrons per energy of incident electron. Combined with the wall collision frequency and electron energy density, this can model the increase in both electron energy and density from secondary emission [17]. The wall collision frequency is calculated from the ratio of plasma volume to wall surface area, and the plasma density.

$$\Gamma_{SEE} = \gamma \Gamma_{e,wall} \tag{3.53}$$

$$\nu_{wall} = \frac{2\pi(r_o + r_i)\Gamma_{e,wall}}{n\pi(r_o^2 - r_i^2)} \tag{3.54}$$

The secondary emission coefficient is calculated via equation 3.55 [44]. The incident energy of the electron greatly influences the chances of a secondary emission event. This relation is empirically derived from experiments with Boron nitride, the ceramic typically used as a wall material in Hall thrusters [44].

$$\gamma = 0.1983 \times \left(\frac{kT_e}{e} \right)^{0.576} \tag{3.55}$$

The SEE flux was calculated based on the assumption of a wall collision frequency of $\nu_{wall} = \alpha 10^7 s^{-1}$ [5] [17]. This is a common assumption in Hall thruster models, and introduces tuning parameter α that takes on values 0.01-0.1 [17]. This assumption allows for the wall flux to be calculated from equation 3.54, and then the SEE flux to be in turn calculated from 3.53. Thus the source term for the fluid electron model can be updated with equation 3.56 to account for secondary emission effects.

$$\Gamma_{SEE} = \gamma \alpha 10^7 \frac{n\pi(r_o^2 - r_i^2)}{2\pi(r_o + r_i)} dt \tag{3.56}$$

Secondary emission effects also include energy lost to the walls, in addition to energy injected via SEE electrons. To account for the energy losses from secondary emission, the following formulation in equation 3.57 was used [17].

$$\Gamma_{SEE\epsilon} = \alpha 10^7 \epsilon_e e^{-U_{see}/\epsilon_e} dt \tag{3.57}$$

This approach is quite empirical in nature, using the same empirical coefficient, α, as seen above, and assumes an emission energy threshold of $U = 20eV$.

3.8 Anomalous Electron Transport

Experimentally, electrons see increased mobility than numerical models capture. The exact mechanism behind this phenomenon is unknown, but there are several theories on what causes this anomalous mobility increase. Due to this lack of particular physics knowledge, the modeling of electron mobility is more complex than the Einstein relation used in the prior section.

There are several theories on the augmentation of the electron mobility, and this thesis examines these theories in their application to a 1D model, and how they scale down to low power Hall thrusters. The un-augmented electron mobility formulation is shown in equation 3.58.

$$\mu_e = \frac{e}{m_e \nu_m} \frac{1}{1 + \frac{\omega_e^2}{\nu_m^2}} \tag{3.58}$$

Using an energy-integrated cross section, the neutral collision frequency ν_m was calculated to be $2.5 \times 10^{-13} \times n_a$ where n_a is the neutral density [22]. Increases in this frequency result in increasing diffusion rates as outlined in section 1's description of the Hall parameter. The models for anomalous diffusion discussed in this thesis all modify the neutral collision frequency as the primary mode of altering the electron mobility through the addition of a ν_{ano} term as seen in equation 3.59. The mechanisms for anomalous diffusion can be seen in table 3.3.

$$\nu_m = 2.5 \cdot 10^{-13} \times n_a + \nu_{ano} \tag{3.59}$$

Mechanism	ν_{ano}	Reference
Wall Collisions	$\nu_{ano} = \alpha \cdot 10^7$	Koo and Boyd [22]
Bohm Diffusion	$\nu_{ano} = \alpha\omega_e$	Koo and Boyd [22]
Mixed Model	$\nu_{ano} = \alpha\omega_e + \alpha \cdot 10^7$	Koo and Boyd [22]

Table 3.3: Anomalous Mobility Models

3.8.1 Wall Collisions

The anomalous mobility model based on wall collisions assumes that the electron-wall collisions accounts for the increase in mobility. The SEE module described earlier accounts for emission of electrons, and energy losses that occur in SEE interactions, but doesn't account for momentum loss interactions with the wall. This model uses an a-priori averaged thermal energy to calculate a wall-electron collision frequency [22]. This wall electron collision frequency is combined with an empirical parameter α which is scaled until the desired discharge current is achieved. This model is accurate in regions with walls, and less accurate in the plume region [22].

$$\nu_{ano} = \alpha \times 10^7 \tag{3.60}$$

3.8.2 Bohm Diffusion

Bohm diffusion postulates that anomalous diffusion is a magnetically driven affect, and that the anomalous diffusion will scale directly with the magnetic field [22]. Anomalous Bohm mobility introduces an empirical parameter α

and multiplies it by the gyrofrequency to generate the anomalous collision frequency. This factor is scaled until the desired discharge current is reached [32].

$$\nu_{ano} = \alpha \cdot \omega_e \tag{3.61}$$

3.8.3 Mixed Model

Koo and Boyd saw most success with a mixed mobility model [22]. This is an approach to modeling anomalous mobility through the used of near wall conductivity in the thruster channel and Bohm mobility outside the channel as a piecewise function.

3.9 Thruster Performance Metrics

The metrics used for thruster comparison include thrust, specific impulse, and various efficiencies. These macroscopic quantities are the output of the simulation, calculated from intermediate plasma properties. Thrust and specific impulse are critical in assessing the use cases for a thruster, and efficiencies are useful in thruster optimization.

Thrust was calculated via the ion velocity and the average ion number density at the exit plane, along with the exit plane area. The density and exit plane area can be related to the ion mass flow rate, $\dot{m}_i = n_i(L)Av_{ion}$. Multiplying the mass flow rate by exhaust velocity gives thrust, as seen in equation 3.62.

$$T = n_i A_{exit} v_{ion}^2 \tag{3.62}$$

The specific impulse was calculated from the thrust by dividing by the input mass flow rate and gravitational constant, as in equation 3.63.

$$I_{sp} = \frac{T}{\dot{m} g_0} \tag{3.63}$$

The anode efficiency is calculated via the product of the mass utilization efficiency, the energetic efficiency, and beam efficiency as describe in equation 3.67 [25]. Mass utilization efficiency is the fraction of propellant ionized as calculated by equation 3.64, using the same conversion of current to mass flow

rate discussed earlier in this section. The energetic efficiency is the ratio of effective discharge voltage, to actual discharge voltage, as described in equation 3.65. The beam efficiency is the ratio of the discharge current to the cathode current as described in equation 3.66 [25].

$$\eta_m = \frac{m_i}{e}\frac{I_{exit}}{\dot{m}_{input}} \tag{3.64}$$

$$\eta_v = \frac{U(L)}{U_d} \tag{3.65}$$

$$\eta_i = \frac{I_d}{I_{cat}} \tag{3.66}$$

$$\eta_a = \eta_m \eta_v \eta_i \tag{3.67}$$

Thrust efficiency is calculated as the ratio of the power generated by the thruster to the power used by the thruster, as seen in equation 3.69, where P_T is the total thruster input power, including cathode, coil, and anode [25].

$$\eta_T = \frac{\frac{1}{2}\dot{m}u_i^2}{P_T} \tag{3.68}$$

$$\eta_T = \frac{T^2}{2\dot{m}P_T} \tag{3.69}$$

3.10 Model Overview

The plasma model developed in this thesis is a 1D hybrid fluid-PIC model that uses a drift diffusion approximation for electrons, particle in cell leapfrog formulation for the heavy species, a Monte Carlo scheme for collisions, a Poisson solver for the electric field, an external simulation for the magnetic field, and several different models for wall effects.

The 1D structure and fluid electrons allow for significant reduction of computational load. Resolving the electron plasma frequency would require timesteps on the order 1×10^{-12} s as opposed to 1×10^{-10} s required for the ion stability. A 1D model also reduces the number of cells by orders of magnitude.

The Drift diffusion approximation isolated the electron mobility and diffusion coefficient to allow for investigation of anomalous diffusion effects. This approximation comes from the first three moments of the Boltzmann equation and the Einstein relation of Diffusion and mobility. The model has four different anomalous diffusion models that modify these transport coefficients that are to be examined in low power applications.

The particle-in-cell approach used for the heavy species maintains accuracy, and is also applicable due to the large mean free path of heavy species collisions. Fluid models require sufficient interaction between particles of the same species to allow for the assumption of a thermodynamic distribution. The omission of magnetic effects for the heavy species is also appropriate due to the very large ratio of Lamor radius to channel length. The PIC approach was also used to simulate the neutral gas expansion in a preliminary simulation, and the neutral species was frozen as a background to the main simulation. This assumption is valid due to the relative velocities of ions to neutrals, as no exterior force is accelerating the neutrals.

Figure 3.5 is a flowchart of the simulation. Quasineutrality is used as a convergence criterion, and timestep relaxation used to increase convergence when the limit is not met. An iteration limit is also introduced for the convergence subroutine, as seen in the flowchart.

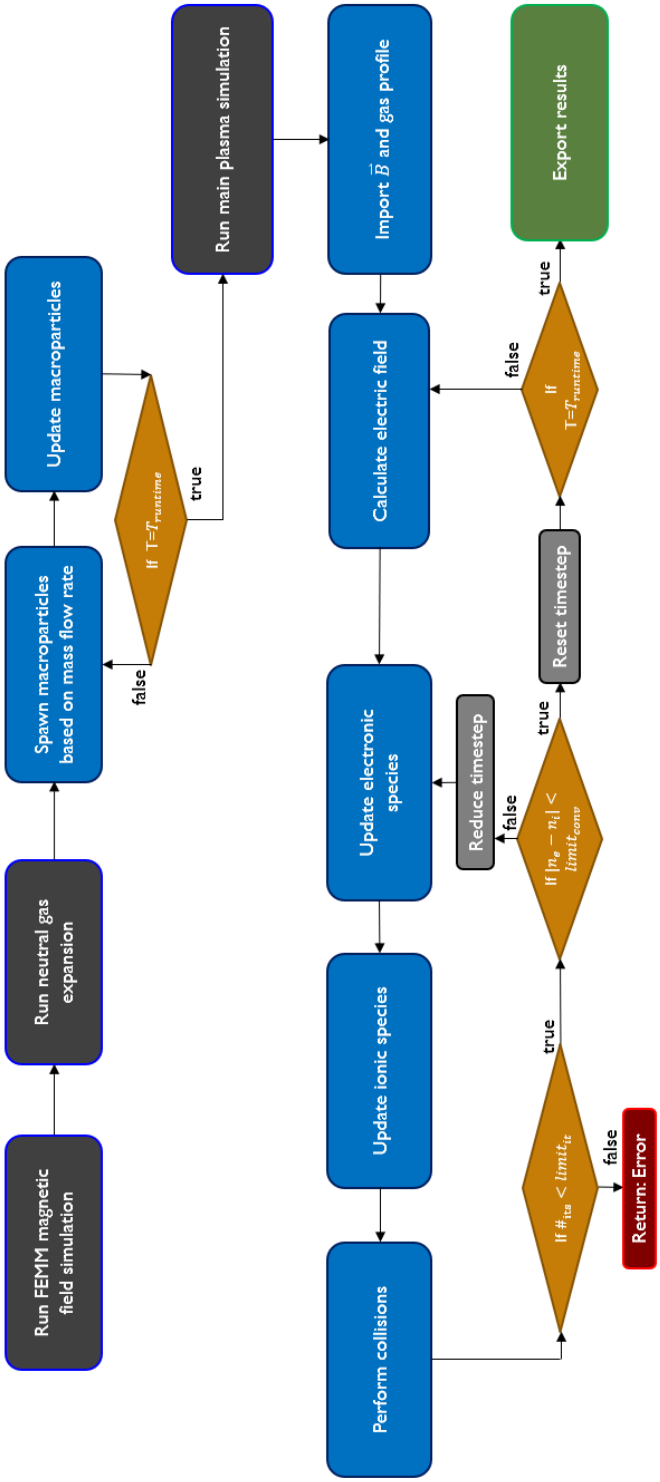

Figure 3.5: Simulation Flowchart

4 Model Validation

To ensure that the model developed for this thesis is accurate, a verification process was applied. This process was primarily comparing the RHS software to both other existing simulations in HPHALL2, HYPICFLU [34] and experimental results [13] [5].

Specific comparisons to other thrusters examined the scaling of thruster performance with changing mass flow rates, discharge voltages, and channel geometries. Thruster performance metrics included thrust, specific impulse, power, anode efficiency, and thrust efficiency. Specific importance was given to the anomalous diffusion models and their effects on the thruster characteristics.

4.1 SPT-100 Thruster Performance

The SPT-100 was used as a baseline model for the examination of thruster performance as calculated by the model in this thesis. The first simulations run were the neutral gas expansion in StarfishPIC and the magnetic field simulation in FEMM. The results in this section will present both simulations performed using classical electron mobility and anomalous electron mobility to better examine the accuracy of the model. The anomalous diffusion results are for the optimized coefficient values unless otherwise stated, outlined in section 3.3. The uncertainty of the presented results is 3% relative, as outlined in chapter 5.

4.1.1 Neutral gas expansion

Xenon exiting the anode of an SPT-100 at 5 mg/s with a macroparticle size of 1×10^9 was simulated in starfishPIC. This value is justified in chapter 6, and is based on the Debye density to allow for the self-shielding behaviour outlined in chapter 2 to occur. The 2D results of the simulation can be seen

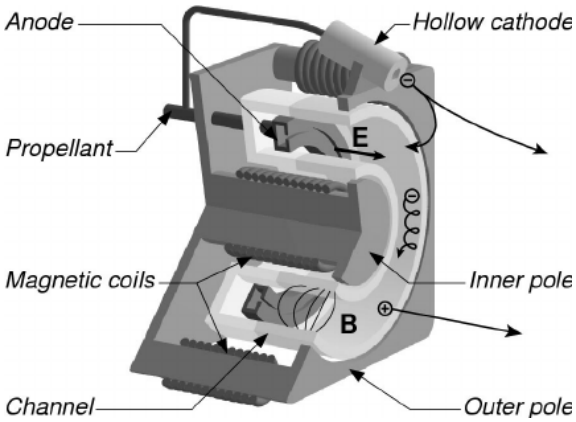

Figure 4.1: Cutaway Schematic View of an SPT-100 Hall thruster (Taken from [14])

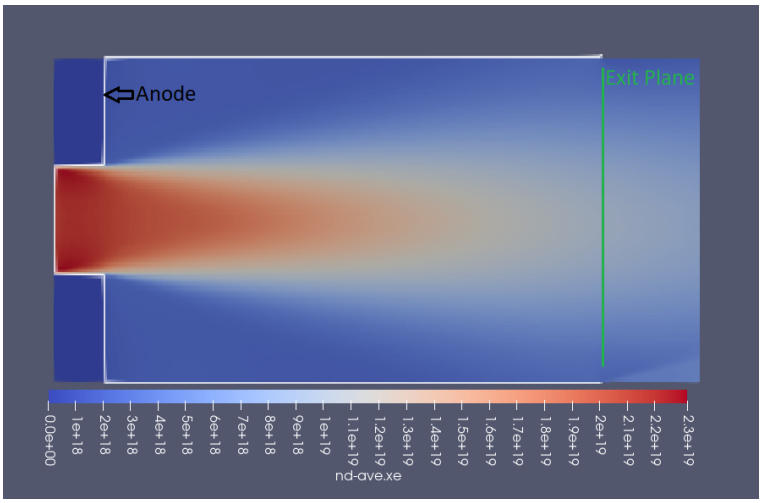

Figure 4.2: 2D time averaged neutral Xenon density in m^{-3}in an SPT-100 at 5 mg/s, simulated in StarfishPIC

in figure 4.2, and the 1D profile extracted and used for the plasma simulation is shown in figure 4.3.

The resultant neutral gas expansion profile is within the variation of the solvers from literature. These solvers include HYPICFLU and HPHall2, hybrid PIC fluid solvers similar to the RHS developed in this thesis [34]. The slight variation is attributed to the gas injection method at the anode, and

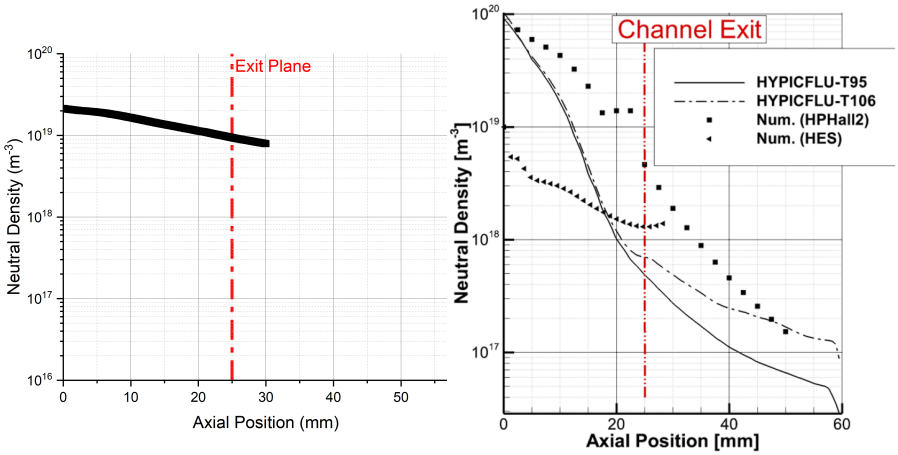

Figure 4.3: Time averaged neutral gas profiles in an SPT-100 thruster at 5 mg/s flow rate, simulated in StarfishPIC (Left) *vs* Literature (Right) [34]

the assumption of a static neutral species in the RHS.

4.1.2 Magnetic Field

The magnetic field of an SPT-100 was simulated in FEMM and a 1D profile extracted to match the profile extracted from the STAFISH neutral gas expansion simulation. The axial profile is shown in figure 4.4.

These results closely match those seen experimentally in SPT-100 thrusters [5][39][31]. This 1D profile, in addition to the neutral gas 1D profile from figure 4.3 were used as the inputs to the benchmarking of the Rappel Hall Sim benchamrk test. Table 4.1 outlines the other inputs that were used by the program. For the initial benchmarking, none of the anomalous diffusion models were included.

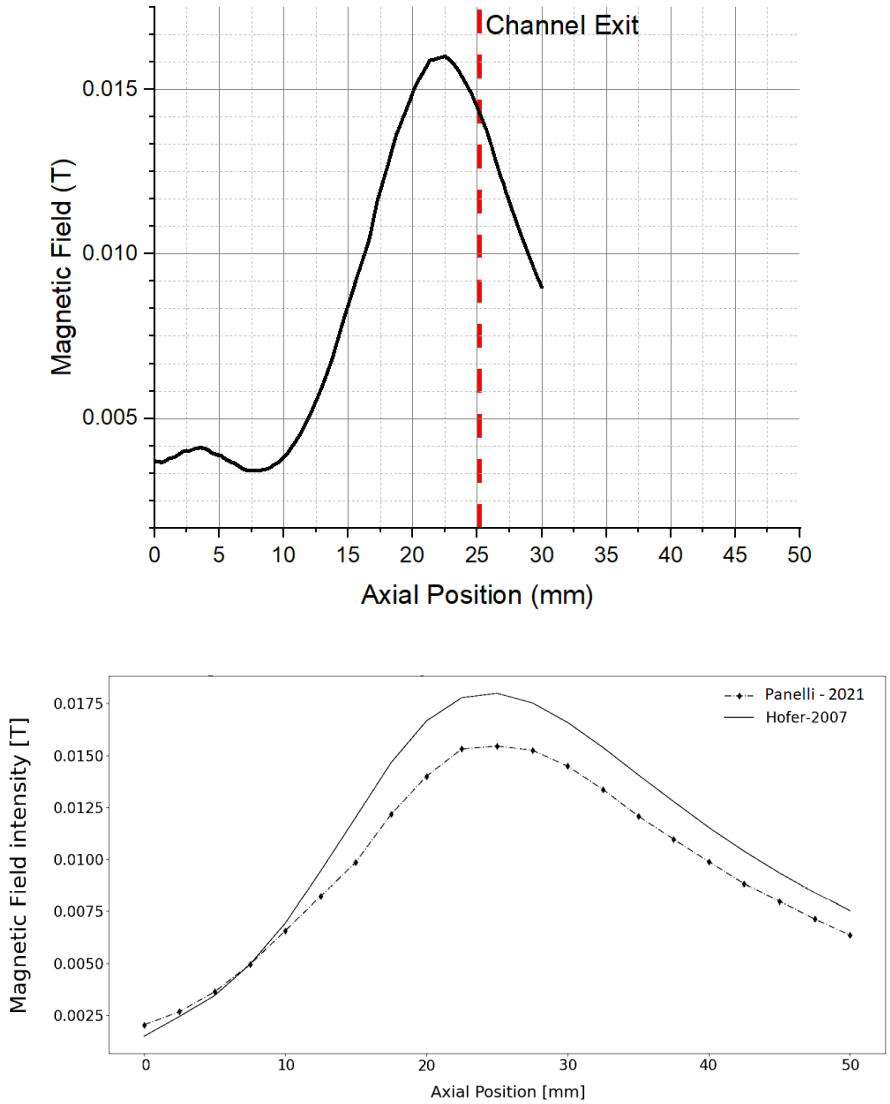

Figure 4.4: FEMM Simulated magnetic field profile in an SPT-100 thruster (Top) *vs* simulated profile in HYPICFLU[34] / HPHALL-2 [19] (Bottom).

SPT-100 Benchmark Simulation Inputs		
Variable	Notation	Value
Channel Length	L	0.025 m
Channel Radius Inner	r_i	0.035 m
Channel Radius Outer	r_o	0.05 m
Discharge Voltage	U_d	300 V
Magnetic Field Maximum	$\mathbf{B}$	0.0150 T
Ano. collision model	ν_{ano}	none
Propellant Mass (Xenon)	m	2.1746×10^{-25} kg
Mass Flow Rate	$\dot{m}_j$	5×10^{-6} kg/s
SEE Empirical Coefficient	α	0.02
Cell Size	dx	1×10^{-4} m
Time Step	dt	2.5×10^{-10} s

Table 4.1: SPT 100 Benchmark Inputs

The values calculated by the RHS are summarized in table 4.2. Comparison of the simulated results to values from literature can be seen in tables 4.3 - 4.5. It is evident that the simulation predicts a thruster performance that is comparable but lower than other numerical models such as those developed by Boeuf [5] and Sankovic [39] and the experimental characterizations performed by Mikellides [31] and Grimaud [16].

SPT-100 Benchmark Simulation Results [15]		
Variable	Notation	Value
Thrust	T	75.1 mN
Specific Impulse	I_{sp}	1530 s
Thrust Efficiency	η_T	0.418

Table 4.2: SPT 100 Benchmark Results

SPT-100 Benchmark - Thrust	
Reference Literature	
Boeuf [5]	90.2 mN
Sankovic [39]	86.9 mN
Mikellides [31]	83.0 mN
Grimaud [16]	80 mN
This Model [15]	
Classical Mobility	75.1 mN ±3%
NWC Mobility	82.7 mN ±3%
Bohm Mobility	86.7 mN ±3%
Mixed Mobility	84.2 mN ±3%

Table 4.3: SPT 100 Benchmark Results - Thrust

SPT-100 Benchmark - Specific Impulse	
Reference Literature	
Boeuf [5]	1734 s
Sankovic [39]	1470 s
Mikellides [31]	1600 s
Grimaud [16]	1600 s
This Model [15]	
Classical Mobility	1530 s±3%
NWC Mobility	1685 s±3%
Bohm Mobility	1767 s±3%
Mixed Mobility	1717 s±3%

Table 4.4: SPT 100 Benchmark Results - Specific Impulse

SPT-100 Benchmark - Thrust Efficiency	
Reference Literature	
Boeuf [5]	0.603
Sankovic [39]	0.463
Mikellides [31]	0.500
Grimaud [16]	0.426
This Model [15]	
Classical Mobility	0.418 ±3%
NWC Mobility	0.506 ±3%
Bohm Mobility	0.557 ±3%
Mixed Mobility	0.526 ±3%

Table 4.5: SPT 100 Benchmark Results - Thrust Efficiency

These tables show that the Rappel Hall Sim can model an SPT-100 thruster at nominal operating conditions. The under-performance of the thruster is attributed to a lack of anomalous electron transport modeling. Lower electron mobility decreases the average electron energy through a lower limit on the kinetic energy achievable. This decreases the likelihood of ionization events, and thus decreases the overall thrust and efficiency of the thruster.

4.1.3 Variable Discharge Voltage

Simulations of the SPT-100 were performed from 150 to 400 Volts using the same inputs defined in table 4.1. The results generated by the sweep are visible in figure 4.5. The thrust, impulse, and efficiencies for each voltage were recorded and compared to values from literature.

Thrust and Impulse

The thrust and specific impulse were expected to scale proportional to the square root of the discharge voltage, as outlined in chapter 2 [9]. The actual results appear more linear in nature and can be seen in figure 4.5. The values again closely matched those found in literature with some deviation.

There are several possible explanations for the linear relationship seen. These include the lack of corrections for anomalous electron transport, and the 1D simplification of the Rappel Hall Sim. Both of these mechanisms are

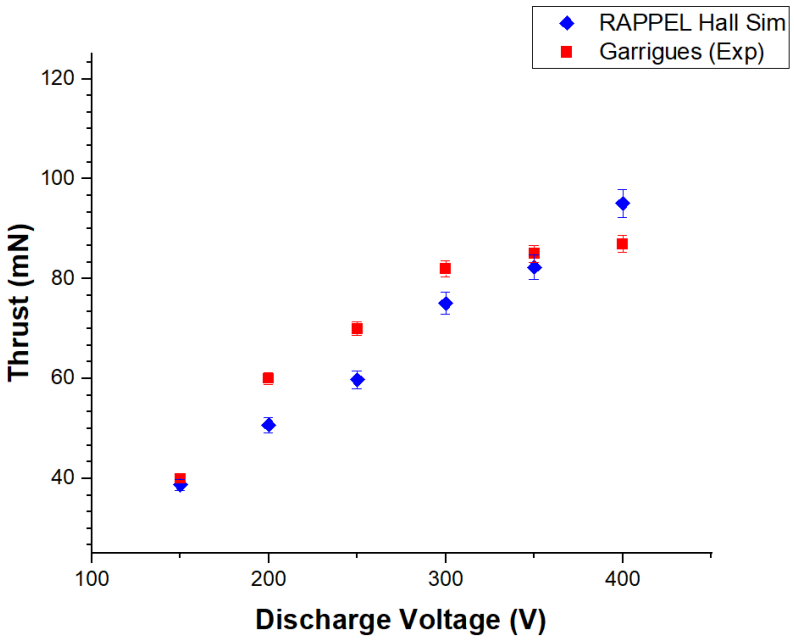

Figure 4.5: Thrust *vs* Voltage for an SPT-100 thruster operating at 5 mg/s flow rate, experimental values taken from Garrigues *et al.* [13]

linked to the thrust and discharge voltage, and could correct the trend seen in the data. The anomalous electron transport will increase the ionization rate and mean electron energy, as driven by the discharge voltage which could account for the change in trends. The 1D nature of the simulation also fails to account for plume divergence, which could reduce the thrust seen at higher power operation.

Power and Efficiency

The magnetic field in the SPT-100 has been optimized for operation at 300 V discharge voltage and 5 mg/s anode mass flow rate. It was expected for the total efficiency of the thruster to be optimal at this operating point at the top of a parabolic curve.

The simulation does not show this trend in parabolic efficiency, and instead shows a linear efficiency scaling. This is likely due to the same process affecting the scaling of thrust with the discharge voltage, as slightly higher thrust at

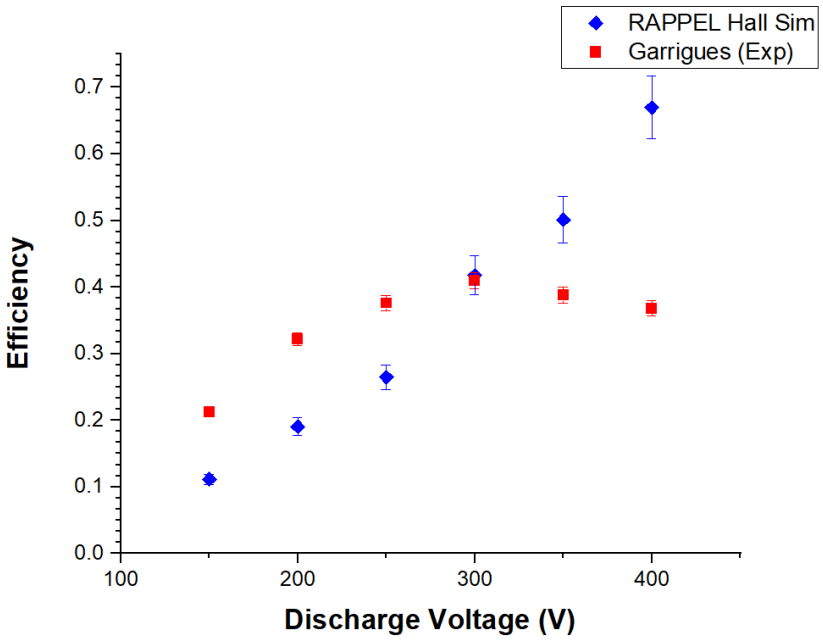

Figure 4.6: Efficiency *vs* Discharge Voltage for an SPT-100 thruster operating at 5 mg/s flow rate, experimental values taken from Garrigues *et al.* [13]

$200 - 300$ V discharge voltage and slightly lower thrust at $350 - 400$ V would results in the correct parabolic curve seen in the experimental data.

4.1.4 Variable Mass flow

The SPT-100 was simulated at several mass flow rates varying from 3.95×10^{-6} kg/s to 5.5×10^{-6} kg/s, otherwise using the same inputs defined in table 4.1. The thrust, impulse, and efficiencies were recorded. These results were compared to values from literature to examine how accurately the model captures the performance of Hall thrusters in a range of operating conditions.

Thrust and Impulse

The expected scaling of thrust is a direct proportionality between the mass flow rate and thrust at constant discharge voltage. The parametric sweep over mass flow rates done using the 1D model is shown in figure 4.7.

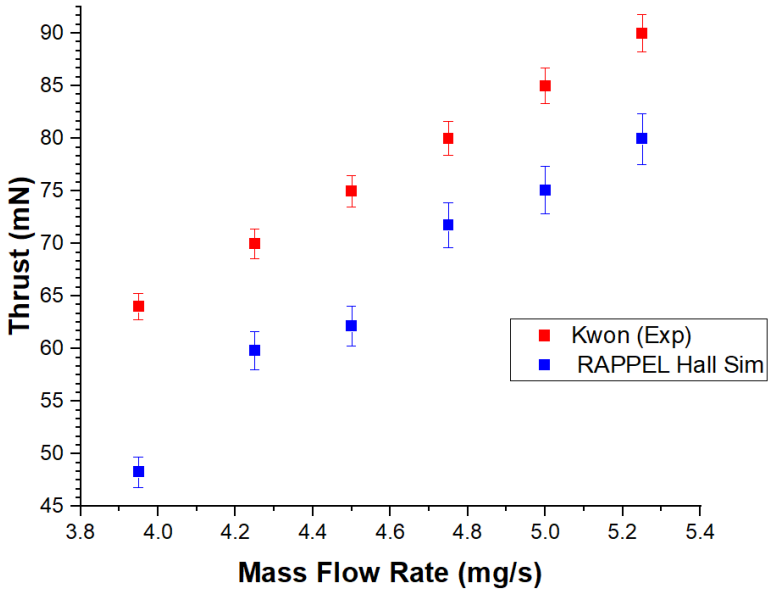

Figure 4.7: Thrust *vs* Mass Flow Rate for an SPT-100 thruster operating at 300 V discharge voltage, experimental values taken from [24]

The linear relationship between thrust and mass flow is evident. The simulated thruster provides a slightly lower thrust on average. This is attributed to the deficiency of anomalous mobility modeling. The increase expected would bring all the other thrust values in line to the experimental results.

Power and Efficiency

The propellant utilization efficiency described by Ashkenazy et al. outlines a direct linear proportionality between mass flow and discharge current [2]. A linear fit of mass flow to current, and thus thrust, was expected. The efficiency is also expected to increase linearly with increased mass flow rate, as the ionization fraction of the propellant increases. This relationship is visible in figure 4.8.

The slope generated by the simulation sweep shows a more significant change in thrust efficiency with varying mass flow rates than the experimental

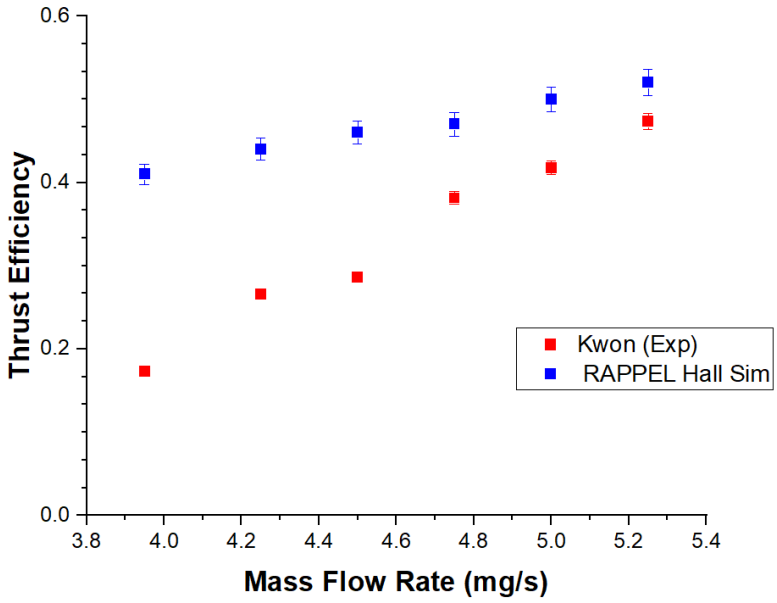

Figure 4.8: Efficiency *vs* Mass Flow Rate for an SPT-100 thruster operating at 300 V discharge voltage, experimental values taken from [24]

results from [24]. Given that the efficiency is inherently linked to the thrust, an increase in the thrust from anomalous diffusion could bring this in line.

4.2 Microscopic Plasma Behaviours

The microscopic plasma quantities used to determine the thruster characteristics were also recorded, and compared to values from literature. The plots shown are a steady state average of the variables, with steady state defines as 4 ms and onwards, the time taken for a typical Hall thruster to ignite.

4.2.1 Plasma Density

The plasma density in a Hall thruster is expected to peak with the magnetic field peak, typically at the exit plane. This is where the classical mobility is highest, impeding the motion of electrons [5]. The computed electron density was expected to be slightly higher with the absence of an anomalous diffusion

term, as anomalous diffusion increases electron transport across magnetic field lines. The peak density as seen in figure 4.9 is 2.5×10^{18} compared to the expected $1.5 \times 10^{18} m^{-3}$ seen in HYPICFLU and HPHALL2 [34] in figure 4.10, and is located in the correct position just inside of the thruster exit plane.

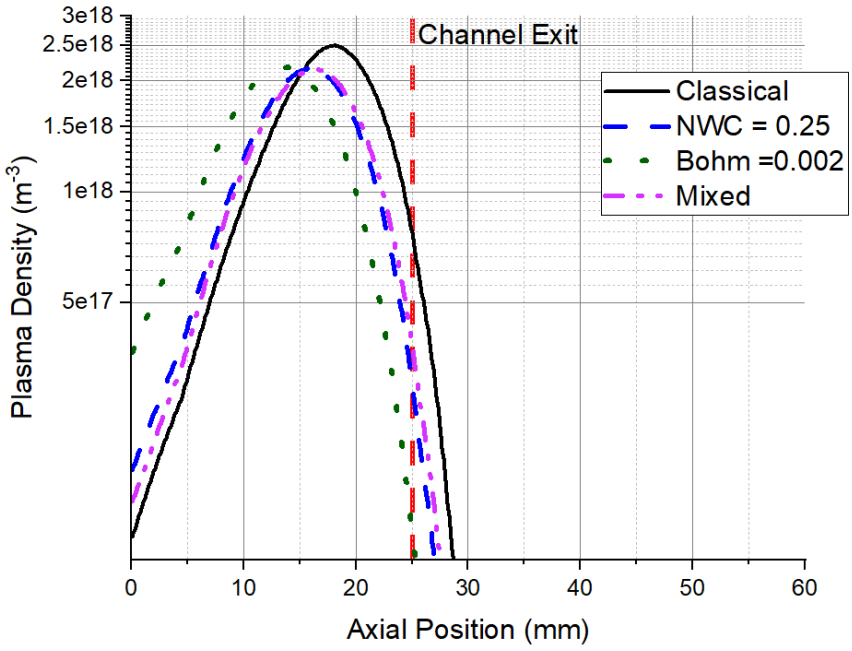

Figure 4.9: Simulated electron number density in an SPT-100 thruster at nominal operating conditions with 4 different mobility models, RAPPEL Hall Sim

4.2.2 Electron Temperature

The average electron temperature in a Hall thruster is typically around $18eV$, and follows the same trend of the electron density peaking with the magnetic field [5]. The modeled average electron energy profile of the SPT-100 Hall thruster operating at nominal conditions can be seen in figure 4.11.

The average electron temperature is significantly higher without the anomalous mobility. The increase in energy at the exit plane occurs as expected

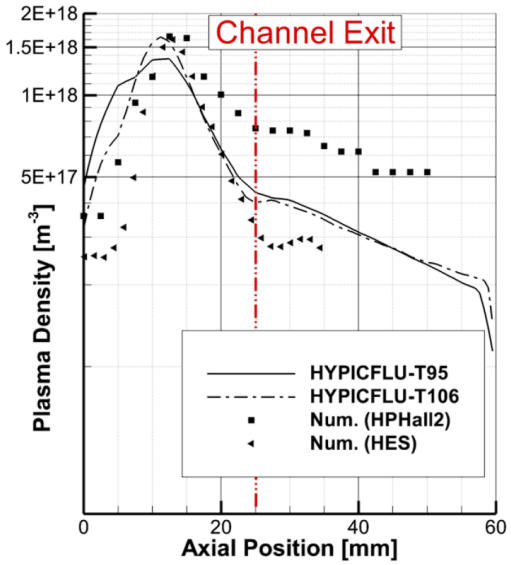

Figure 4.10: Simulated electron number density in an SPT-100 thruster at nominal operating conditions, HYPICFLU/HPHALL2 [34]

however, albeit significantly larger than seen in HYPICFLU and HPHALL simulations [34]. The similarity in treatment between the electron energy and number density in the numerical model can explain this phenomenon. Energy is transfer ed in the model through drift and diffusion mechanisms in the same way the number density is. An increase in the electron mobility would decrease the energy in a similar way to the observed decrease in electron number density. Anomalous diffusion has a much more significant impact on the temperature than then number density however. This could explain the increased plasma density seen by the model.

4.2.3 Electric Field

The electric field in Hall thrusters is typically on the order of $20,000-30,000$ V/m, and peaks just after the magnetic field peak outside of the exit plane [5]. Given that the plasma potential is driven by the plasma density, so with a sharp decrease in density and thus potential, a spike in the electric field will occur in the same location. The simulation results were expected to be slightly lower, as the electron temperature has significant impact on the electric potential calculation via the Boltzmann distribution as outlined in Chapter 3 and the temperature profile returned was lower than expected.

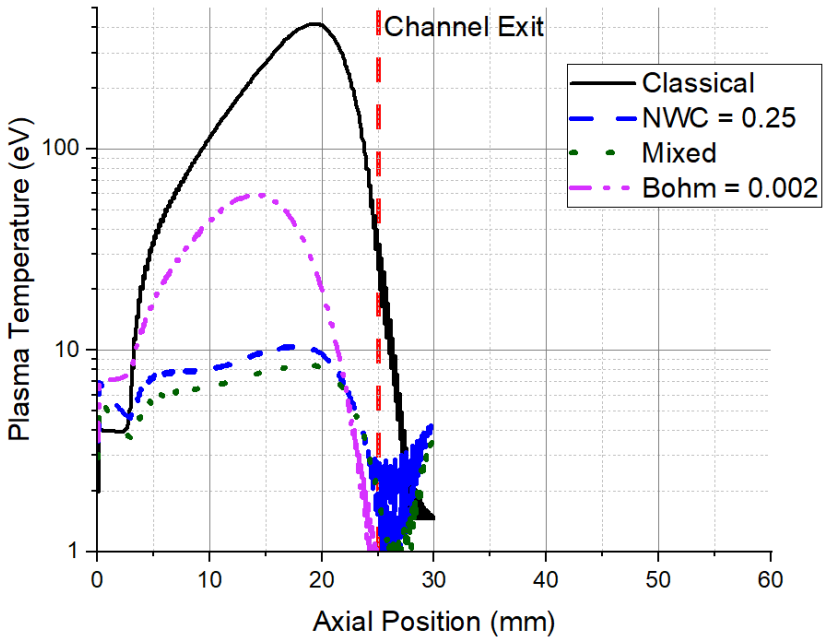

Figure 4.11: Simulated electron temperature in an SPT-100 thruster at nominal operating conditions with 4 different mobility models, RAPPEL Hall Sim

The electric field is relatively close to the expected magnitude, and peaks in the correct location at the channel exit plane. With the introduction of anomalous mobility it is expected that the electron temperature will increase, and thus the potential and its gradient will increase by a similar factor according to the Boltzmann relation [36].

4.2.4 Classical Electron Mobility

The electron mobility is expected to be significantly lower when anomalous mobility is unaccounted for. This is seen in figure 4.16 where the classical mobility as calculated by the Rappel Hall Sim is approximately one-tenth the augmented mobility seen in HYPICFLU and HPHALL [34].

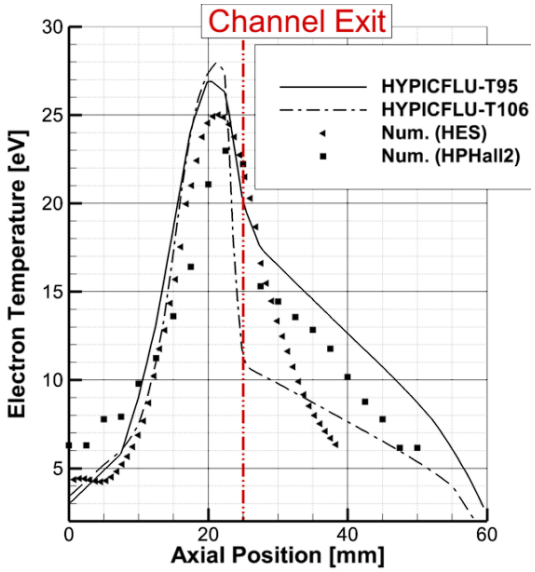

Figure 4.12: Simulated electron temperature in an SPT-100 thruster at nominal operating conditions, HYPICFLU/HPHALL2 [34]

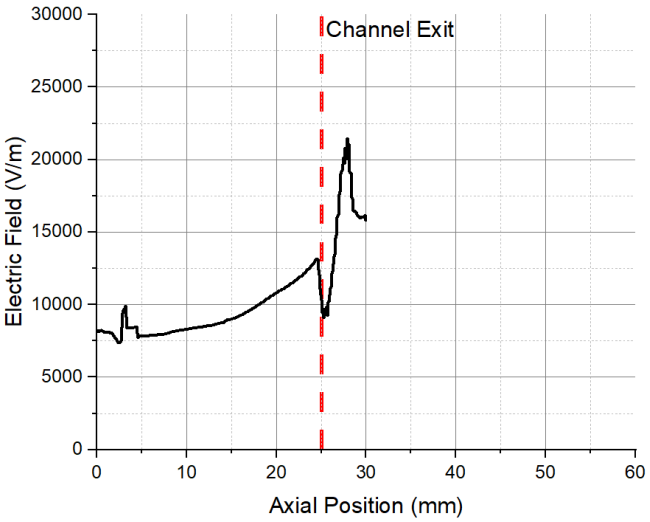

Figure 4.13: Simulated electric field in an SPT-100 thruster at nominal operating conditions; Rappel Hall Sim

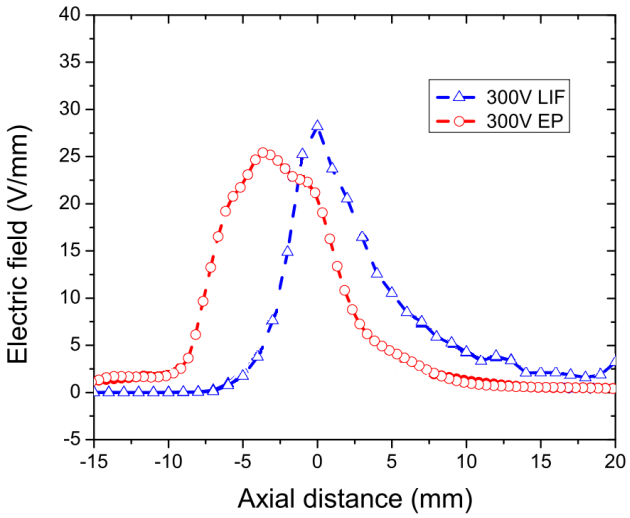

Figure 4.14: Electric field in an SPT-80 thruster at nominal operating conditions; Experimental measurements with laser induced florescence and emissive probes taken from [16]

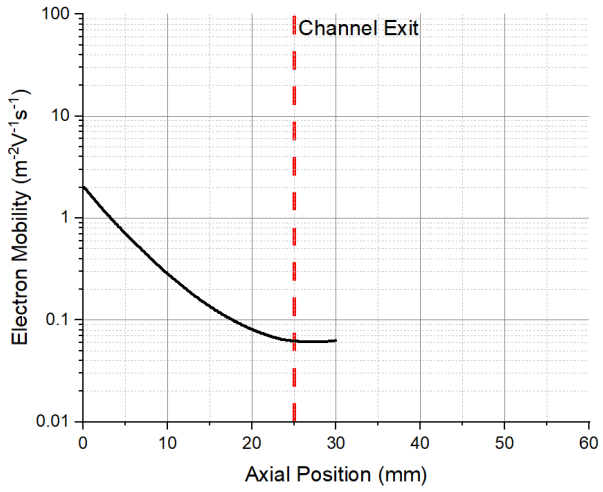

Figure 4.15: Simulated classical electron mobility in an SPT-100 thruster at nominal operating conditions: Rappel Hall Sim

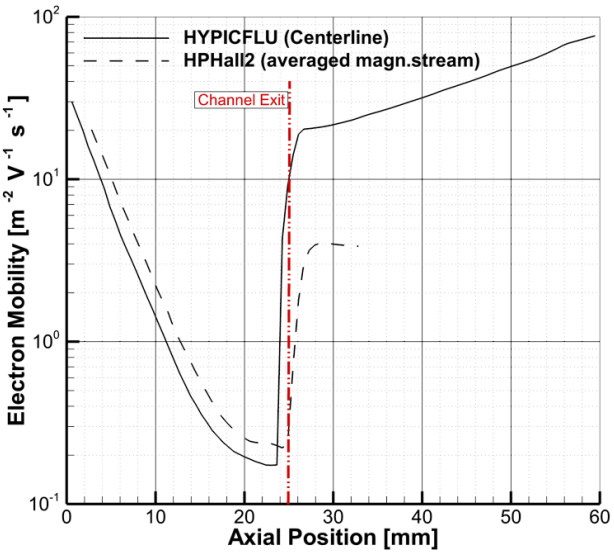

Figure 4.16: Simulated augmented electron mobility in an SPT-100 thruster at nominal operating conditions: HYPICFLU/HPHALL2 [34]

4.3 Anomalous Mobility Model Benchmark

Anomalous electron mobility is not fully understood, so modeling it requires the use of empirical coefficients. For the RAPPEL Hall Sim, a range of empirical coefficients were tested that returned values around the magnitude of the augmented mobility as seen in literature [34]. The parameter value that returned the most accurate thruster performance metrics was selected as the 'optimal' coefficient. This was done for the SPT-100 at nominal operating conditions, but the optimal empirical coefficients will change with changes in discharge voltage and mass flow rate [24].

4.3.1 Near-Wall Conductivity

The introduction of a wall collision term to the electron momentum transfer frequency improved the thruster performance, as predicted. The thrust, specific impulse, and thrust efficiency all increased to values that are much closer to the references literature. The results can be seen in figure 4.17. The wall mobility empirical coefficient used was $\alpha_{wall} = 0.1$, taken from the paper by Koo and Boyd [22]. The wall collision model assumes that collisions with the walls induce anomalous transport, modeled through adding constant collision

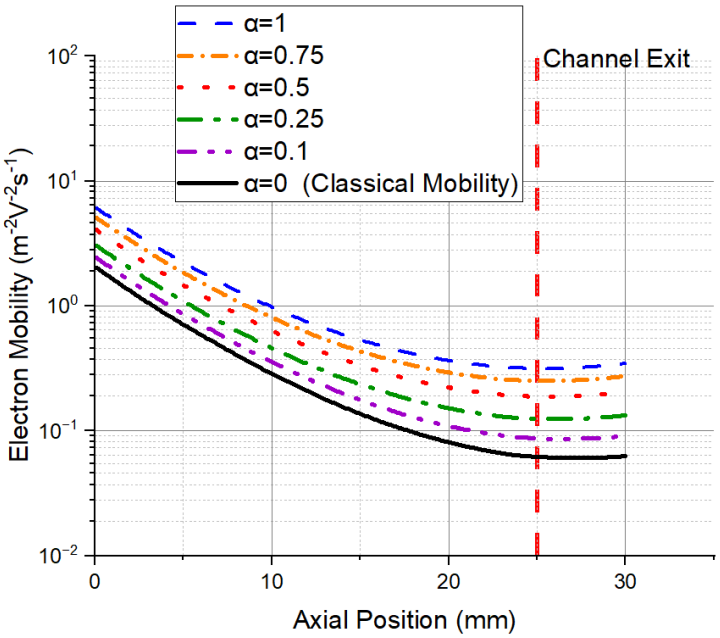

Figure 4.17: Simulated NWC augmented electron mobility in an SPT-100 thruster at nominal operating conditions; varying empirical near wall conductivity parameter

frequency $\nu_{anno} = \alpha \times 10^7$. In this context alpha is a tuning parameter that took on values in the range of 0.1 to 1, as in Koo and Boyd's investigation on anomalous mobility in Hall thrusters [22]. Figure 4.17 depicts the electron mobility varying the empirical parameter α. For this method of calculating the anomalous mobility, the empirical coefficient was tuned to return values of $0.1 - 0.3 \mathrm{m}^{-2}\mathrm{V}^{-1}\mathrm{s}^{-1}$, as calculated by HYPICFLU and HPHALL2 [34].

α_{nwc} Value	Thrust (mN)	I_{sp} (s)	Efficiency	Mobility ($m^{-2}V^{-1}s^{-1}$)
1	52.1	1063	0.263	0.3147
0.75	69.6	1419	0.335	0.2515
0.5	75.0	1529	0.417	0.1883
0.25	82.6	1685	0.506	0.1251
0.1	79.6	1624	0.470	0.0872
0	75.0	1530	0.418	0.06197

Table 4.6: SPT 100 Wall Collision Mobility Results for varying α_{wall}, reported mobility inside exit plane. Measurements at 3% relative uncertainty

Simulations at nominal operating conditions were run over a range of coefficient values to determine the most accurate value. Figure 4.18 outlines the thruster performance as it changes with the anomalous diffusion coefficient.

The cross field mobility is most significant at the thruster exit plane, as this is where the magnetic confinement of the electrons is the strongest, and close to where the density of electrons is the highest. A value of $\alpha = 0.25$ matches the calculated mobility to values from literature at the exit plane. This is also the value for the empirical coefficient where accuracey of thruster performance was optimized. The primary effect on the microscopic plasma parameters appears to be changes in electron density. Figure 4.20 shows how the electron density changes with varying of the near wall conductivity empirical parameter.

With increasing anomalous mobility, the electron density profile decreases in magnitude, increases in width and shifts towards the anode. There is a notable change in the mass utilization of the thruster that appears to be the mechanism behind the observable improved thrust. This is attributed to the higher electron density by the gas emitting anode, axial position = 0. There appears to be a point where the increase in plasma density by the anode begins to inhibit the performance of the thruster.

As mentioned in Chapter 3, the wall collision mobility assumption for anomalous diffusion is most applicable in the thruster channel itself. In terms of the effects on the plasma profiles, the electron density did decrease slightly as predicted, the change visible in figure 4.20.

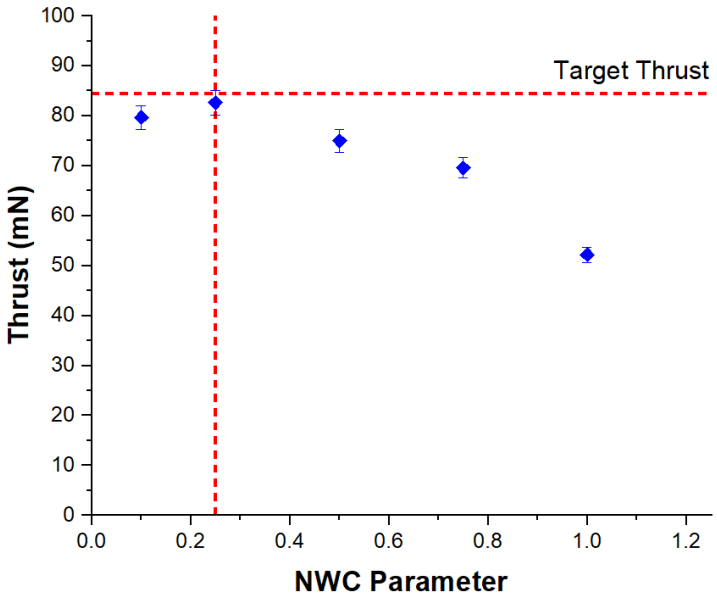

Figure 4.18: SPT 100 Thrust vs. varying α_{NWC} at nominal operating conditions

The addition of the anomalous mobility results in a profile that matches the other simulation programs much closer than the classical mobility model shown earlier in figure 4.16. The near wall conductivity model returns a lower mobility at the anode than HPHALL2 or HYPICLFU [34]. This is attributed to the neutral gas density at the anode being higher by about an order of magnitude, seen in figure 4.3. Given that anomalous mobility is being modeled as an increase in the neutral-electron collision frequency, it follows that a lower neutral density will result in a lower mobility at the anode. At the thruster exit plane the predicted mobility matches much closer to the values returned by HYPICFLU and HPHALL2 [34].

4.3.2 Bohm Diffusion

The next model for anomalous diffusion was Bohm Diffusion, an anomalous mobility model that assumes a proportionality to the gyrofrequency of the electrons within a plasma. Taking the form of $\nu_{ano} = \alpha_{Bohm}\omega_e$. The empirical Bohm diffusion coefficient α_{Bohm} was given values ranging from 0.001 to 0.005,

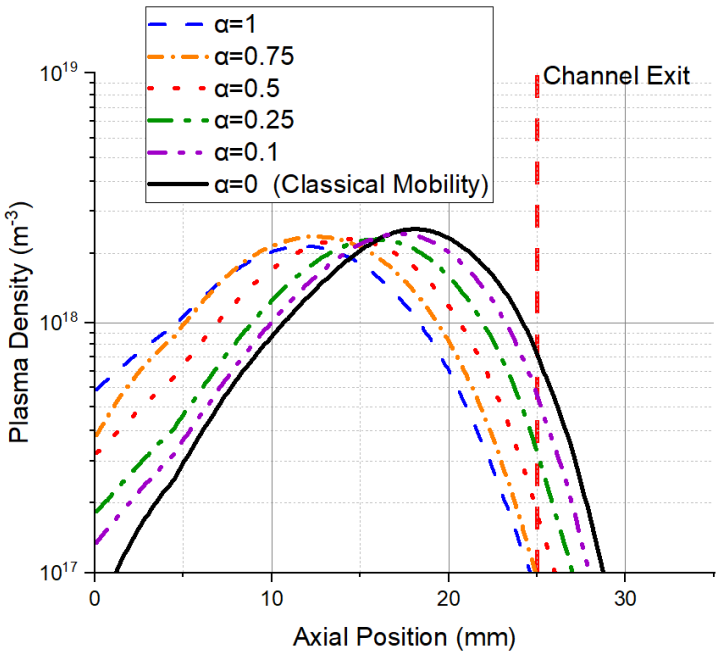

Figure 4.19: Simulated electron density in an SPT-100 thruster at nominal operating conditions; varying the empirical near wall conductivity parameter

as done by Koo and Boyd [22]. Figure 4.22 shows the thruster performance for this parametric sweep. For this method of calculating the anomalous mobility, the empirical Bohm coefficient was tuned too return a value of 0.1-0.3 $m^{-2}V^{-1}s^{-1}$, as calculated by HYPICFLU and HPHALL2 [34].

Using the same approach as the near wall conductivity model $\alpha_{Bohm} = 0.002$ shows the optimal thruster performance within the outlined range of coefficients. Similar to the near wall conductivity model, the increase in mobility shows a more accurate thruster performance at the given empirical coefficient value.

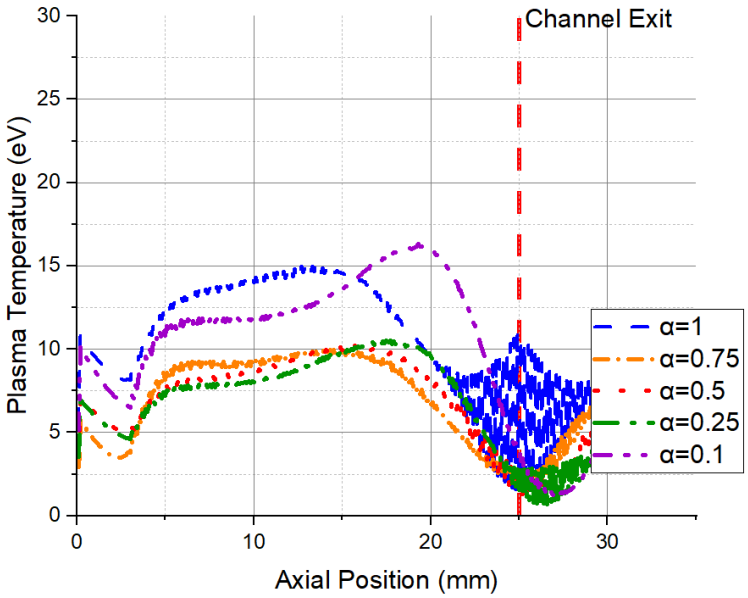

Figure 4.20: Simulated electron temperature in an SPT-100 thruster at nominal operating conditions; varying the empirical near wall conductivity parameter

α_{Bohm} Value	Thrust (mN)	I_{sp} (s)	Efficiency	Mobility ($m^{-2}V^{-1}s^{-1}$)
0.005	25.3	516	0.0475	0.3953
0.004	62.6	1277	0.291	0.3286
0.003	78.5	1600	0.457	0.2620
0.002	86.7	1768	0.557	0.1953
0.001	83.7	1706	0.519	0.1286
0	75.0	1530	0.418	0.06197

Table 4.7: SPT 100 Bohm Mobility Results for varying α_{Bohm}, reported mobility inside exit plane. Measurements at 3% relative uncertainty

The electron density plots exhibit similar trends to those seen when using the near wall conductivity model, but the Bohm model has less deviation in the maximum value of electron density from one empirical value to the next. The exception to this is when the empirical Bohm coefficient takes on a value

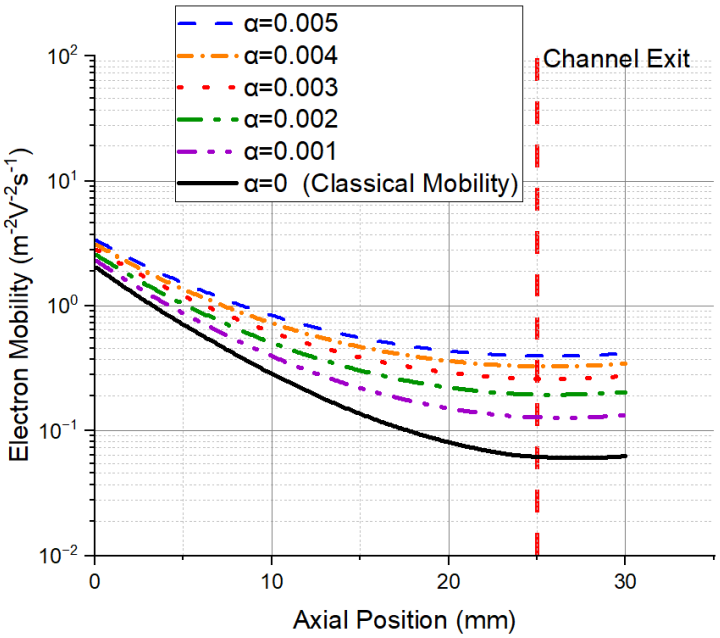

Figure 4.21: Simulated electron mobility in an SPT-100 thruster at nominal operating conditions; varying the empirical Bohm diffusion parameter

of 0.005. Beyond this range, increases in the empirical Bohm coefficient results in event more significant deviation from the classical mobility baseline.

The optimal Bohm diffusion coefficient returns a mobility profile that is lower than the near wall conductivity model at the anode. The similarity in results from the Bohm and Near Wall Conductivity models makes sense as both are tuned to produce the same value at the thruster exit plane. It is important to note that reproducing the same mobility value of $0.2\mathrm{m}^{-2}\mathrm{V}^{-1}\mathrm{s}^{-1}$ at the exit plane is not the optimal case for both mobility models. Variation within the channel still has significant effects on the modeled thruster performance. The optimal Bohm coefficient corresponds with a significant increase in the average electron temperature as seen in figure 4.24.

4.3.3 Mixed Mobility

As mentioned in Chapter 4, the Bohm diffusion model is more accurate outside the main thruster channel, and Near Wall Conductivity is more accu-

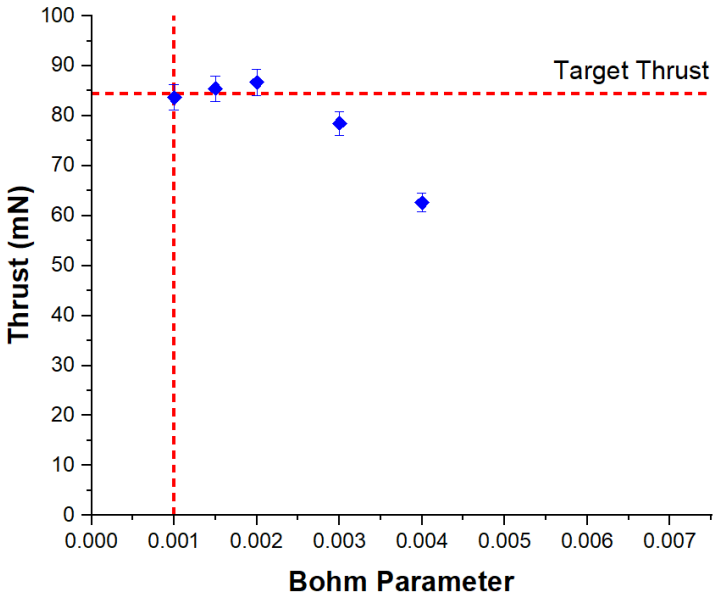

Figure 4.22: SPT 100: Thrust *vs.* varying α_{Bohm} at nominal operating conditions

rate within the channel. For this reason, a mix of near wall conductivity and Bohm diffusion is often used [22]. It is defined as a piece-wise function that uses near wall conductivity inside the thruster channel , and Bohm mobility in the plume $\nu_{ano} = \alpha_{Bohm}\omega_e + \alpha_{wall}10^7$.

The resulting discontinuity has a smaller increase than those seen in HPHALL2 and HYPICFLU [34]. To examine the interaction of the two mobility models, a sweep of α_{Bohm} was performed. At the higher end attempting to replicate the mobility seen in HYPICLFU [34] the simulation diverged and no meaningful data could be recovered. At lower values in line with HPHALL2 [34], there was a drastic decrease in thruster performance as can be seen in table 4.8. The previously optimized empirical Bohm coefficient of 0.002 did correspond to a marginal increase in thruster performance over the near wall conductivity, but this did not match the values calculated by HPHALL2 and HYPICFLU [34]. The resulting electron mobility profiles can be seen in figure 4.25, and their associated electron density profiles are shown in figure 4.26.

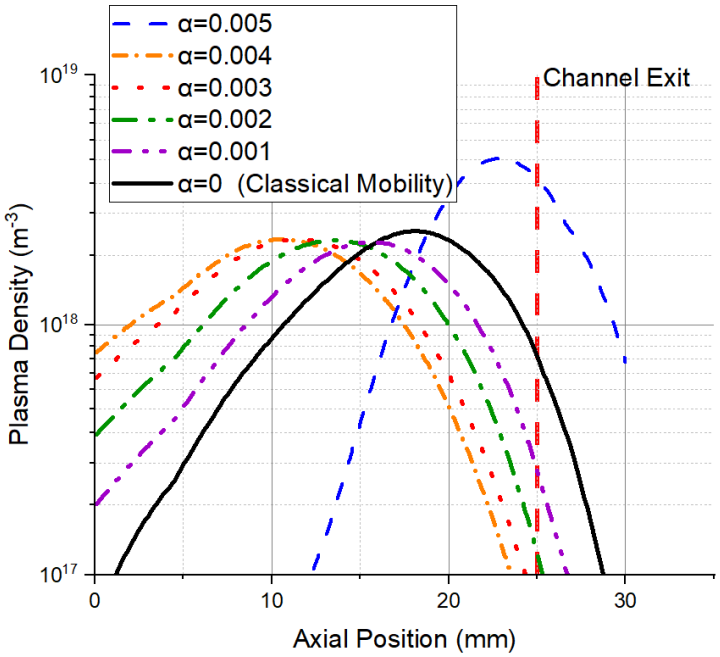

Figure 4.23: Simulated electron density in an SPT-100 thruster at nominal operating conditions; varying the empirical Bohm diffusion parameter

α_{Bohm} Value	Thrust (mN)	I_{sp} (s)	Efficiency	Mobility ($m^{-2}V^{-1}s^{-1}$)
0.05	12.3	252	0.0113	3.386
0.02	40.6	827	0.122	0.7284
0.005	77.3	1577	0.444	0.3952
0.002	84.2	1717	0.526	0.1951
0.001	81.0	1651	0.486	0.1285
0 (NWC)	82.6	1685	0.506	0.1251

Table 4.8: SPT 100 Mixed Mobility Results for varying α_{Bohm} and $\alpha_{Wall} = 0.25$, reported mobility outside exit plane

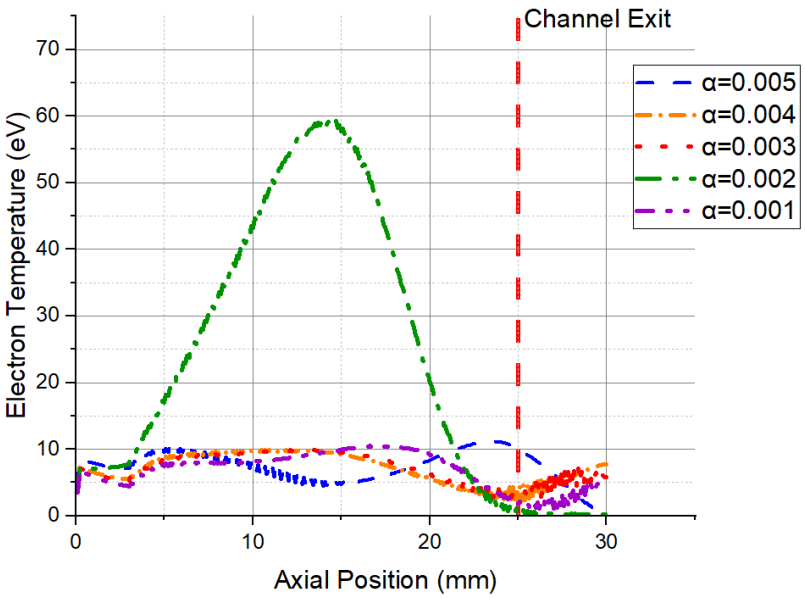

Figure 4.24: Simulated electron temperature in an SPT-100 thruster at nominal operating conditions; varying the empirical Bohm diffusion parameter

It is interesting to note that the change in mobility outside the thruster exit plane has a significant impact on the density profile inside the exit plane. The combination of $\alpha_{wall} = 0.25$ and $\alpha_{Bohm} = 0.002$ results in 84.24 mN of thrust at 1717 s specific impulse and an efficiency of 0.526. This is very close to the average values of referenced literature [5] [39] [31] [16].

Kwon et al. determined that the optimal empirical coefficients for mixed mobility Bohm-wall models change with discharge voltage and mass flow rate among other factors [24]. They propose a 36 trial numerical exploration of the empirical coefficients to determine the optimal coefficient values, squaring and adding the relative errors as compared to experiment to determine the most accurate coefficients [24]. Kwon et al. propose that the empirical coefficients can be presented as free parameters in attempts at a-priori simulation of thrusters, presenting results for a range of potential coefficients [24].

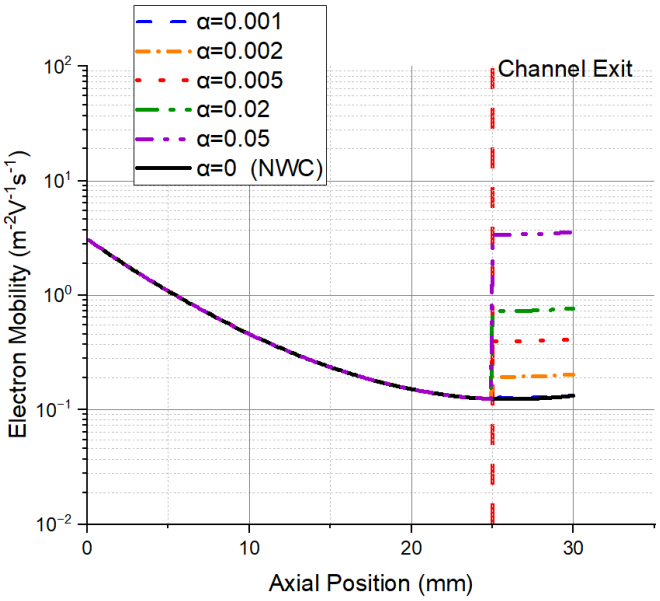

Figure 4.25: Simulated augmented electron mobility in an SPT-100 thruster operating at nominal operating conditions; varying Bohm diffusion parameter in a mixed mobility anomalous diffusion model with $\alpha_{wall} = 0.25$

The numerical exploration used for this thesis was based on that on Kwon et al. [24], but optimized the NWC coefficient first and then the Bohm coefficient second, reducing the number of trials required to 12 from 36. The optimal coefficient was determined to be that which had the lowest error in thrust. This approach was used for the remainder of the data presented in this thesis unless otherwise stated.

4.3.4 Thruster Performance with Anomalous Mobility

The use of an appropriate empirical mobility model can improve the simulated performance of the thruster. Figure 4.27 shows a plot of the discharge voltage vs thrust produced by the simulation for optimized anomalous diffusion coefficients in a mixed mobility model alongside the thrust predicted by classical mobility.

The implementation of an optimized anomalous mobility model greatly improves the accuracy of the simulation, but is limited in use as a design tool.

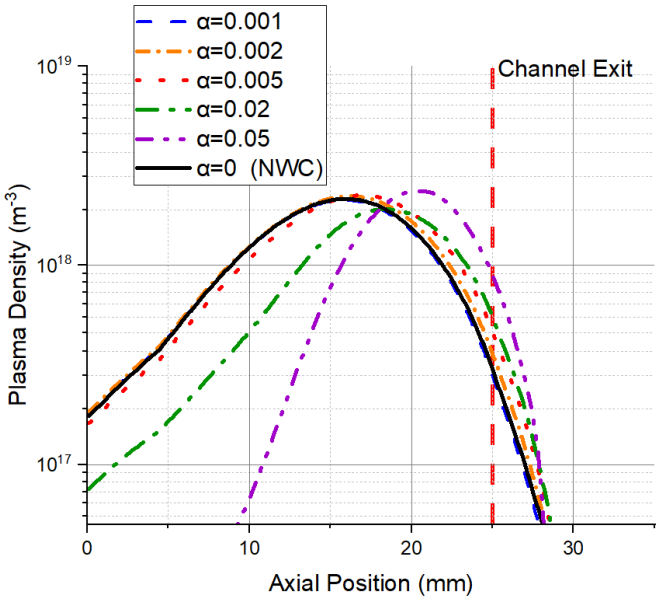

Figure 4.26: Simulated electron density in an SPT-100 thruster at nominal operating conditions; varying the Bohm diffusion parameter in a mixed mobility anomalous diffusion model with $\alpha_{wall} = 0.25$

The knowledge required to optimize the coefficients and produce accurate results implies knowledge of the thruster operating conditions in advance of running the simulation. The inclusion of optimized anomalous diffusion significantly increased the accuracy of the simulation. For this data, a mixed anomalous diffusion model was used. The empirical coefficients were optimized via numerical exploration using the same method outlined earlier, 0.002 for the Bohm coefficient and 0.25 for the near wall conductivity coefficient. These coefficients are similar in value to those used by other numerical models [24].

4.4 2.6 cm Princeton Plasma Physics Laboratory Cylindrical Hall Thruster

The scaling effects of thruster dimensions are expected to be less predictable than the other variables. Given that the simulation is one dimensional in nature, geometric scaling effects are likely to be the subject of most error in

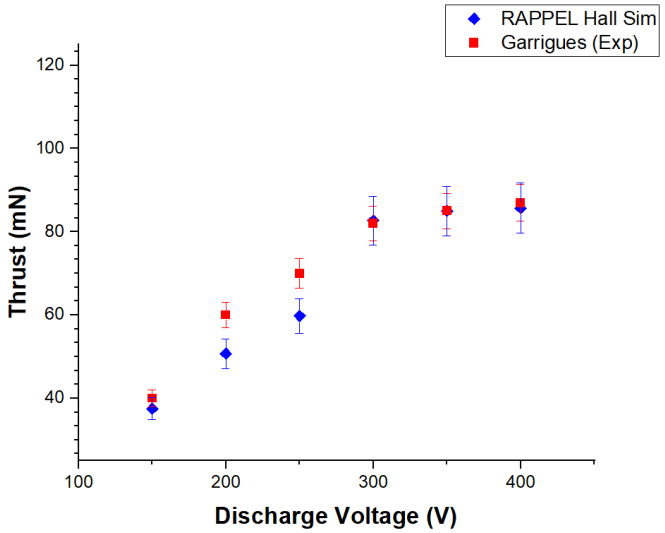

Figure 4.27: Thrust *vs* Discharge Voltage for an SPT-100 thruster operating at 5 mg/s flow rate, experimental values taken from Garrigues et al. [13]

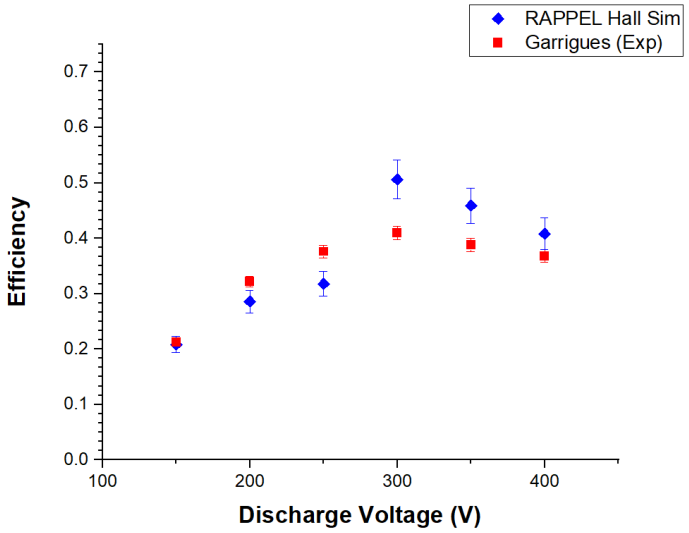

Figure 4.28: Efficiency *vs* Discharge Voltage for an SPT-100 thruster operating at 5 mg/s flow rate, experimental values taken from Garrigues et al. [13]

the model, as significant assumptions are required in adapting a 3D channel to a 1D model.

The RAPPEL lab is focused on micropropulsion, accordingly a low power Hall thruster was used as a benchmark. This test case examined the 2.6 cm Princeton Plasma Physics Laboratory Cylindrical Hall Thruster (2.6 cm PPPL CHT) [41, 37], shown in figure 4.29.

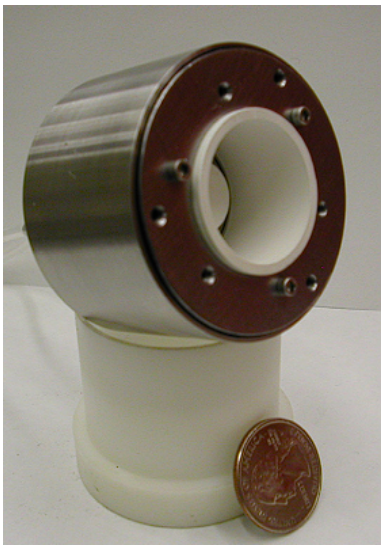

Figure 4.29: PPPL 2.6 cm CHT (From [37])

The inputs for the 2.6 PPPL CHT simulation are summarized in table 4.9, and the RHS results in table 4.10.

2.6 cm PPPL CHT Simulation Inputs		
Variable	Notation	Value
Channel Length	L	0.022 m
Channel Radius Inner	r_i	0 m
Channel Radius Outer	r_o	0.013 m
Discharge Voltage	U_d	250 V
Magnetic Field Maximum	$\mathbf{B}$	0.065 T
Ano. collision model	ν_{ano}	Bohm
Bohm Empirical Coefficient	α_{Bohm}	0.1
Propellant Mass (Xenon)	m	2.1746×10^{-25} kg
Mass Flow Rate	$\dot{m}_j$	0.4×10^{-6} kg/s
SEE Empirical Coefficient	α	0.02
Cell Size	dx	1×10^{-4} m
Time Step	dt	1×10^{-10} s

Table 4.9: 2.6 cm PPPL CHT Simulation Inputs, taken from [41]

The Bohm diffusion model for anomalous mobility was chosen to model this thruster was chosen on account of the work done by Smirnov et al. who simulated the thruster at the Princeton Plasma Physics Laboratory and compared it to the experimental performance of the thruster [41]. They used a full PIC simulation with Bohm mobility to model the thruster. They noted that the most accurate empirical Bohm coefficient was several times larger than typically seen in the modeling of Hall thrusters. The optimal coefficient value was determined to be on the order of 1/16 compared to typical values on the order of 0.001 [41]. The range of the numerical exploration was changed to account for this phenomenon. The uncertainty in theses results increased to ±8%, as outlined in chapter 5

2.6 cm PPPL CHT Simulation Results			
Variable	Notation	Sim. ±8%	Exp. [41]
Thrust	T	5.0 mN	5 mN
Specific Impulse	I_{sp}	1273 s	1200 s
Thrust Efficiency	η_T	0.208	0.20

Table 4.10: 2.6 cm PPPL CHT Simulation Results

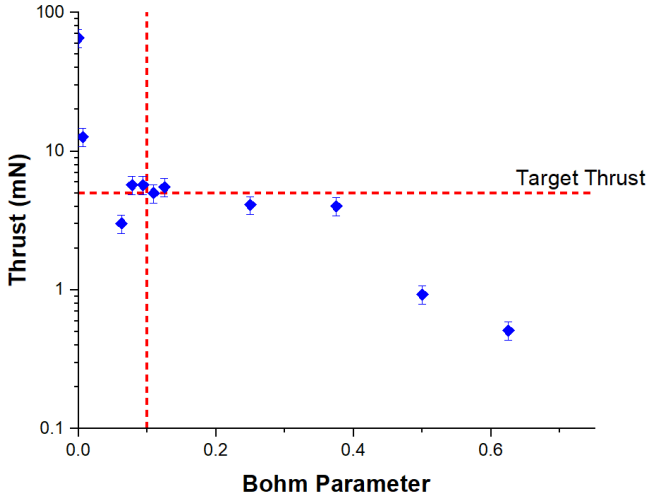

Figure 4.30: Simulated thrust from the PPPL 2.6cm CHT for varying Bohm Parameter

A sweep of empirical values from $\alpha_{Bohm} = 0.005$ to 0.5 was performed. The results are shown in figure 4.31.

The optimal Bohm coefficient was found to be similar to that outlined by Smirnov et al. with a value of 0.1, significantly higher than the 0.002 used for the SPT-100. It is evident that the anomalous mobility has a much more significant effect in these lower power thrusters, varying the thrust over orders of magnitude. The plateau observed in both the NWC on Bohm models is of interest, as it lines up with the target thrust quite closely in both models.

Another pattern to note is the decrease in thrust with anomalous mobility with the PPPL 2.6 cm CHT thruster and the increase with the SPT-100. This is likely on account of the magnetic field. In the SPT the annular geometry allows for the peak to be placed at the exit plane, whereas the cylindrical geometry of the PPPL 2.6 CHT has the peak well within the acceleration channel.

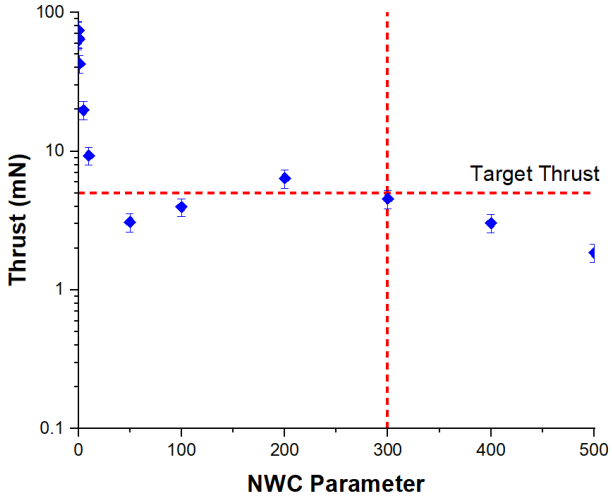

Figure 4.31: Simulated thrust from the PPPL 2.6cm CHT for varying NWC Parameter

4.5 Summary

The RHS was found to capture the trends and physics of an operational Hall thruster. Tuning of empirical parameters was required to obtain measurements within error of experimental results. The values that theses empirical coefficients were optimized at was found to be in line with values in found literature, further indicating that the model is correctly modeling the physics within Hall thrusters. There is still significant room for improvement in the accuracy of the model stemming from the simplifications and assumptions made. A further investigation of the accuracy, precision, and limitations of the model is the focus of Chapter 5.

5 Model Performance

The development of the RAPPEL Hall Sim was very much an iterative process. Plasma simulations are complex, and there are many different approaches, assumptions, and simplifications that must be made to model all the interconnected physical processes at play within a Hall thruster. The initial design goal was to develop a piece of software that has the ability to predicatively model low power Hall thruster operation with the intent to be used as a design tool within the RAPPEL lab.

The RAPPEL Hall Sim has the capacity to model the performance and trends of low power Hall thrusters, with some limits to the accuracy of the model. The limitations of a 1D model and the nature of the simplifications and assumptions mean that this model is not suitable for examining small scale physical plasma phenomenon and localized wall interactions. The performance of the thruster can be captured, and allows for the software to be used as a design tool, as will be demonstrated in chapter 6.

5.1 Comparison to Other Hall Thruster Modeling Software

This type of simulation is well documented, as seen in table 5.1. A number of 1D hybrid quasineutral Hall thruster models exist and are used by labs to design and characterize Hall thrusters. The construction of this software has expanded the research capacity of the RAPPEL Lab, and laid the framework for more detailed simulation work to be conducted in the future.

Summary of Hall Thruster Modeling Softwares			
Author(s)	Model Type	SEE	Potential Solver
Boeuf and Garrigues (1998)	1D hybrid	No	QN
Ashkenazy et al. (1999)	1D hybrid	No	QN
Morozov and Savelyev (2000)	1D hybrid	No	QN
Keidar et al. (2001)	1D fluid	Yes	Poisson
Ahedo et al. (2002)	1D hybrid	No	QN
Roy and Pandey (2002)	1D fluid	Yes	QN
Ahedo (2003)	1D fluid	Yes	Poisson
Barral et al. (2003)	1D fluid	Yes	QN
Hara et al. (2012)	1D hybrid	No	QN
Komurasaki and Arakawa (1998)	2D hybrid	No	QN
Fife (1998)	2D hybrid	Yes	QN
Hagelaar et al. (2002)	2D hybrid	No	QN
Koo and Boyd (2004)	2D hybrid	No	QN
Keidar et al. (2004)	2D fluid	No	QN
Parra et al. (2006)	2D hybrid	Yes	QN
Garrigues et al. (2006)	2D hybrid	Yes	QN
Mikellides and Katz (2012)	2D fluid	Yes	QN
Lam et al. (2015)	2D hybrid	Yes	QN
Andreussi et al. (2018)	2D fluid	Yes	QN
RAPPEL Hall Sim (2023)	1D hybrid	Yes	QN

Table 5.1: Summary of Hall Thruster Modeling Software [42]

Hybrid models have been used extensively to simulate Hall thrusters as is seen in table 5.1, but do have some drawbacks. The discretized nature of macroparticle representation of the ionic species created discontinuities in the charge density profile. This in turn caused issues with the electric field solver.

5.2 Electric Field Solvers

The first iterations of the RAPPEL Hall Sim used a Poisson potential solver rather than a quasineutral solver. This Poisson solver used the net charge density and Gauss's Law to calculate the electric potential. The hybrid nature of the plasma representation resulted in discontinuities in the net charge density that in turn resulted in an increased frequency of instabilities that arose in

the simulations. The Poisson Solver also required the program to solve a large system of linear equations with each timestep, significantly increasing the computational load of the simulation. The solution to each of these problems was to transition to the quasineutral potential solver that uses the plasma density rather than the charge density. The use of the Boltzmann Dsitribution to calculate the electric potential, as outlined in chapter 3, greatly reduces the computational requirements of the program, and allows for the fluid electron density to be used to calculate the ion density and avoid the discontinuities inherent to PIC representation.

The complexity and continuity problems associated with a Poisson solver are likely why it is not used as often as the quasineutral approach. In table 5.1 it is evident that the quasineutral approach is preferable to the Poisson solver, with only two out of the twenty other simulation programs using a Poisson solver [42].

5.3 Accuracy and precision

Analysing the accuracy of the RAPPEL Hall Sim is challenging when the empirical anomalous diffusion models influence the outputs so significantly. In light of these limitations, the accuracy of the model with and without the use of anomalous diffusion was examined. The accuracy analysis was done by taking the error in each benchmark simulation and taking the average and standard deviation of the error. The average relative error was used for examining the accuracy of a model, and the standard deviation of that error was used for examining the precision.

For the un-augmented model, the mean of the error across all benchmarking data points was 12.33%. With the addition of the anomalous mobility, this drops to 7.1%.

The Monte-Carlo Collision scheme for ionization introduces an aspect of randomness to the simulation, varying results slightly when all input parameters are the same. To better analyze the precision of the model, 100 simulations with the same inputs were run and the deviation of the results analyzed bellow. The standard deviation of the thrust results was 2.4 mN around an average of 82.8 mN, or about 3% relative imprecision.

Treating both of these quantities as independent error sources results in an uncertainty in the simulation results of 12.7% for the un-augmented simulation and 7.7% for the anomalous mobility augmented simulation.

To examine if this error is absolute or relative to the calculated thrust, a similar investigation was performed looking into the performance of the PPPL 2.6 cm CHT. After 100 simulations the standard deviation was approximately $4 \times 10^{-4} mN$, or 8% relative, used as the error for the low power measurements. An increase in error by an order of magnitude in this context is expected. The imprecision introduced by the Monte-Carlo scheme will be more pronounced at lower mass flow rates on account of fewer particles.

5.4 Model Stability

The RAPPEL Hall Sim could not return meaningful results for all tested inputs. The primary method of failure for simulations was numerical solver divergences defined as localized electron number density spikes significantly above physically possible values (plasma density > neutral density). There were a number of causes for this behaviour. The most common causes for these singularities was improper spatial and temporal discretization. To examine the effects of this, a parameter sensitivity analysis was run on the numerical parameters of timestep, cell size, and macroparticle weight. The bounds on these parameters were determined via Von-Neuman stability analysis.

5.4.1 Particle-In-Cell Stability Limits

The first major decision in developing the RAPPEL Hall Sim was how to model the different plasma species. As outlined in chapter 3, a fluid approach was decided. There were two primary factors that lead to this decision. The first was the increases in computational efficiency offered by a fluid electron model. The requirement to represent the Debye length and plasma frequency in the spatial and temporal discretizations respectively would have lead to significantly longer computational times with PIC electrons. The other factor was the mobility modeling. The drift-diffusion model adapts very readily to models of anomalous electron transport in a Hall thruster. Treatment of the electrons as a bulk modulus and isolating the mobility in the drift diffusion equation as seen in chapter 3 allows for easy modification and examination of different mobility models.

The decision for the ions to be represented as PIC was based on the fact that the ions were assumed to be collisionless and unmagnetized, assumptions that are not applicable to the electronic species. Without a significant number of self-collisions, the thermodynamic equilibrium required for fluid models is not achieved. The unmagnetized nature also means that complex mobility models are not required. Thus a simple particle pusher model was used, realizing the much lower Debye length and plasma frequency of the ions.

The use of the forward difference method in PIC schemes leads to unstable numerical errors over time in PIC models, as the acceleration is not constant over the timestep, it will change as the electric field changes in time. This change will offset the actual results, and compounds over time leading to an instability [45]. To examine it numerically, a harmonic oscillator of an electron in the field of a stationary ion can be considered. From chapter 2, the equations of motion for this oscillator is as follows:

$$x'' = -\omega^2 x \tag{5.1}$$

$$x' = -\omega \sin(\omega t) \tag{5.2}$$

$$x = \cos(\omega t) \tag{5.3}$$

$$\omega = \left(\frac{n_{e0} e^2}{\epsilon_0 m_e} \right)^{1/2} \tag{5.4}$$

Lubos Brieda et. al. examine the stability with Von-Neumann analysis of the forward difference scheme by introducing linear amplification factor g [6].

$$x^{n+1} = g x^n \tag{5.5}$$

$$v^{n+1} = g v^n \tag{5.6}$$

This amplification factor represents the change in x from one timestep to the next. Von-Neumann analysis assumes that the error grows proportionally to the values itself. In a stable system, this growth factor g will be $|g| \leq 1$. Stability can be analysed by expressing the system of equations in matrix form, and solving for allowed values of g [6]. For a non trivial solution of the system of equations to exists, the determinant must be equal to zero.

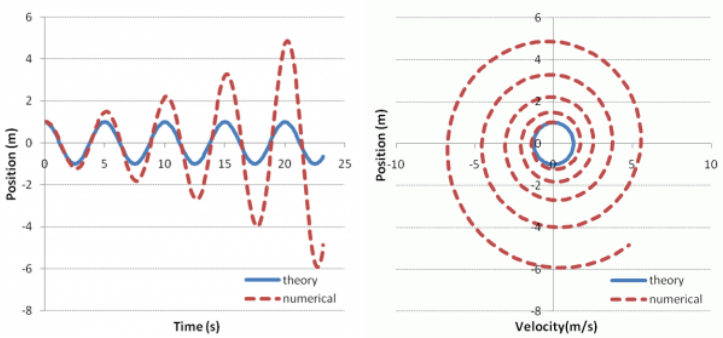

Figure 5.1: Theory *vs* Forward difference numerical integration scheme for a charged particle harmonic oscillator [6]

$$\begin{bmatrix} g-1 & \omega_p^2 \Delta t \\ -\Delta t & g-1 \end{bmatrix} \begin{bmatrix} v_0 \\ x_0 \end{bmatrix} = \begin{bmatrix} 0 \\ 0 \end{bmatrix} \tag{5.7}$$

The determinant for this system is:

$$(g-1)^2 + \omega_p^2 \Delta t^2 = 0 \tag{5.8}$$

So for a solution to exists, g must take on values $g = 1 \pm i\omega_p \Delta t$. These values indicate that this forward difference method is inherently unstable. Figure 5.1, created by Brieda et al., shows the evolution of such a harmonic oscillator model over time. Brieda identifies the issue in this scheme as using the nth velocity to calculate the $n+1$ position when using the time averaged velocity would be more accurate, the velocity at $n + 1/2$ [6].

Using time averaged variables to alternating calculate distance and velocity changes is known as the leapfrogging method. The velocity integration occurs on half timesteps, and the position on whole timesteps, resulting in an algorithm that 'leapfrogs' over itself to allow for time averaged integration [6].

$$x^{n+1} = gx^n \tag{5.9}$$

$$v^{n+1/2} = gv^{n-1/2} \tag{5.10}$$

$$\begin{bmatrix} g^{1/2} - g^{-1/2} & \omega_p^2 \Delta t \\ -\Delta t & g-1 \end{bmatrix} \begin{bmatrix} v_0 \\ x_0 \end{bmatrix} = \begin{bmatrix} 0 \\ 0 \end{bmatrix} \tag{5.11}$$

The system is then modified as seen in equations 5.9 through 5.11. The amplification factor g is split evenly in between $v^{n+1/2}$ and $v^{-1/2}$ as it is scaling from the value at $n = n$. Setting the determinant of the system to zero results in equation 5.12 [6].

$$g^2 - (2 - \omega_p^2 \Delta t^2)g + 1 = 0 \tag{5.12}$$

Application of the quadratic formula results in a solution for g as equation 5.14.

$$g = \frac{(2 - \omega_p^2 \Delta t^2) \pm \sqrt{(2 - \omega_p^2 \Delta t^2)^2 - 4}}{2} \tag{5.13}$$

$$g = 1 - \frac{\omega_p^2 \Delta t^2}{2} \pm i\omega_p \Delta t \sqrt{1 - \frac{\omega_p^2 \Delta t^2}{4}} \tag{5.14}$$

Calculating the magnitude of g via the complex conjugate and applying the limitation of $|g| \leq 1$ results in the inequality seen in equation 5.15. This also happens to limit the value of g to real numbers. So for the leapfrogging scheme to be stable, the timestep of the simulation has an upper limit dependant on the plasma frequency.

$$\Delta t < \frac{2}{\omega_p} \tag{5.15}$$

The resulting equations of motion for the charged particle species are seen in equations 5.16 to 5.18. A graphical representation of this scheme done by Breida et al. can be seen in figure 5.2.

$$x_{n+1} = x_n + v_{n+1/2} \Delta t \tag{5.16}$$

$$v_{n+1/2} = v_{n-1/2} + a\Delta t \tag{5.17}$$

$$a = \mathbf{E} \frac{q}{m} \tag{5.18}$$

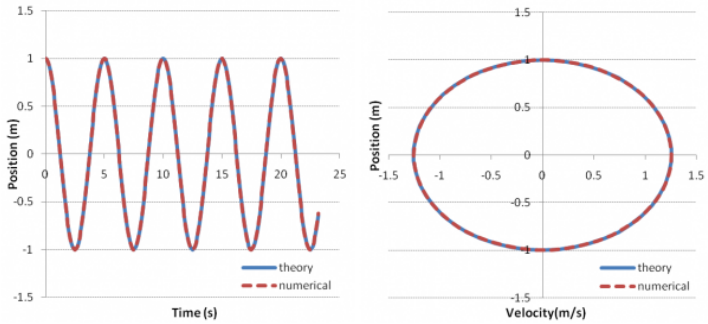

Figure 5.2: Theory *vs* Leapfrog numerical integration scheme for a charged particle harmonic oscillator [6]

This scheme for PIC advancement in time is considered stable for cell sizes $< \lambda_D$ and timesteps $< \omega_p^{-1}$. This limit does not apply to fluid models. There is no association of velocity to a given particle, so the compounding of errors seen in the forward difference method does not occur in the fluid electrons present in the model.

5.4.2 Parameter Sensitivity Analysis

Timestep Sensitivity

Simulations were run across a range of timsteps. The SPT-100 was simulated at nominal operating conditions with the mixed mobility model outlined in chapter 5. Simulations were run using timesteps of 1×10^{-9} s, 1×10^{-10} s, 1×10^{-11} s, and 1×10^{-12} s. A divergence occurred in the simulation with timestep equal to 1×10^{-9} s. Seeing as the typical plasma frequency for the operating conditions of an SPT-100 is on the order of $1 \times 10^{10} s^{-1}$, this timestep violates the stability criterion of dt $< \omega_p^{-1}$. The other trials had no discernable variation with timestep in measured thrust and efficiency or plasma properties. All imprecision was attributed to the Monte-Carlo methods, and was always at or under the 3% variation outlined earlier in this chapter. The simulation results were found to be conclusively independent of the timestep used.

Cell Size Sensitivity

Simillarly to the exploration of the timestep dependence, for the cell size dependence investigation the SPT-100 was simulated at nominal operating conditions with varying cell sizes. The simulated cell sizes were dx $= 1 \times 10^{-5}$

m, 1×10^{-4} m, and 1×10^{-3} m. There was significantly more variation to these results. The first trial, dx = 1×10^{-5} m, resulted in a divergence in the simulation. The second trial was that used in the bulk of this paper, and the third gave results with significant difference with thrusts on the order of 120 mN rather than the expected 80 mN. Given that the stability limit on the PIC algorithm for the ions is dx $< \lambda_D$, and for the SPT-100 the Debye length $\lambda_D = 1 \times 10^{-3}$ m [33], this instability in the results is given little importance.

The divergence in the first trial is attributed to the stiffness of the equations being solved. The RAPPEL Hall Simulation uses SI units and a first order spatial disrcretization to solve the differential equations. The equations governing plasmas are known to be numerically stiff in nature [1]. This approach served well to develop the software but remains a limitation that can be improved upon in future work.

A second set of trials was run in the range of $\lambda_D >$ dx $> 1 \times 10^{-5}$ m. The simulated values were dx = 7.5×10^{-5} m, 1×10^{-4} m, and 2.5×10^{-4} m. There was little to no variation found in these results beyond that introduced by the Monte-Carlo scheme.

Macroparticle Weight Sensitivity

The effects of several different macroparticle weights on the simulation of an SPT-100 were examined. These included 1×10^8, 1×10^9, 1×10^{10} , and 1×10^{11}, all expressed in ions per macroparticle. Variation grew with increase in the macroparticle weight. The primary cause of variation in the simulation is the Monte-Carlo scheme used for macroparticle interactions. With an increase in the weight, and decrease in number of the macroparticles, the individual macroparticles influence the final result more significantly at higher weights. The total thrust in each trial can be seen in table 5.2.

Macroparticle weight (#/particle)	Thrust	Charge Ratio (-/+)
1×10^9	83.4 mN	0.722
1×10^{10}	91.5 mN	0.280
1×10^{11}	234.6 mN	0.292

Table 5.2: Thrust and macroparticle weight

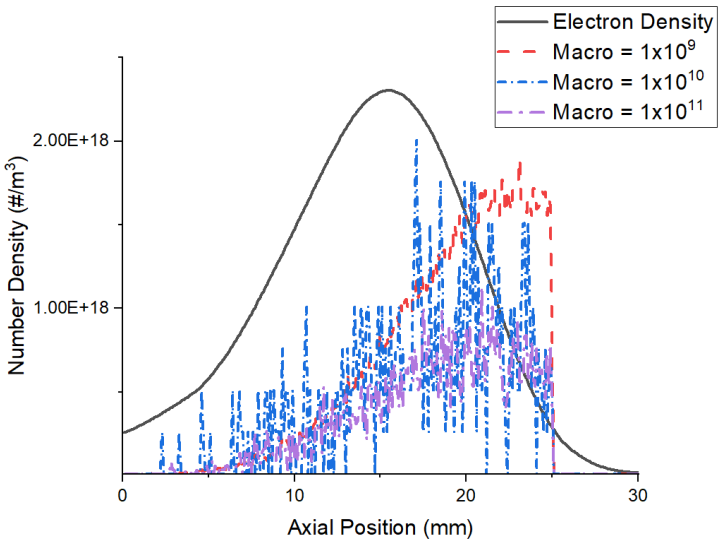

Figure 5.3: Ion Density *vs* Electron Density for varying macroparticle weight

Figure 5.3 shows how the ion number density changes with varying macroparticle size. There is a significant decrease in the ion density with increasing macroparticle size. This affects the quasineutrality of the plasma, as seen in table 5.2. With a plasma density on the order of $1 \times 10^{18}\text{m}^{-3}$ and a Debye length of 1×10^{-3} m, macroparticle sizes $> 1 \times 10^{9}$ m will result in a Debye density lower than one. Less than one particle per cubed Debye length means that the Debye shielding behavior described in chapter 2 cannot occur, and the model cannot capture the critical process of Debye shielding occuring within the plasma [36]. This results in significant deviation from quasineutrality at high macroparticle weights.

The discretization values for macroparticles, cell size, and timestep are comparable to those used by others in literature, specifically Cappelli *et al.* in HYPICFLU [7]. A side by side comparison of those used by the RAPPEL Hall Simulation and Cappelli et al. can be seen in table 5.3.

Variable	RAPPEL Hall Sim	Capelli et al. [7]
Timestep	1×10^{-10} s	2×10^{-10} s
Cell Size	1×10^{-4} m	1.25×10^{-4} m
Macroparticle Weight	1×10^{9}	3×10^{9}

Table 5.3: Discretization Parameters

5.5 Lessons Learnt from 1D Model

There still remains significant space for iterative improvement in the model. Adaption to two dimensions would allow for more in depth examination of wall effects and how they effect secondary emission and anomalous transport. The stability of the solver could be improved upon as well, issues were often arising around numerical heating and singularities at higher power operation and at high electron mobility values.

The 1D nature of the model greatly reduced the work required to develop the software such that it could be the basis of a Master's thesis. There are significant drawback in accuracy of the model however, relying heavily on empirical parameters to return accurate results. The very significant impacts of anomalous electron diffusion on the operational characteristics of the simulated Hall thrusters show this empirical dependency. The 1D nature of the software inherently limits the accuracy with which it can resolve this phenomenon, but it is left for future work to improve upon the model.

6 Use Case: Preliminary design of a Cylindrical Dual Stage Hall Thruster

Propellant utilization in Hall thrusters decreases when scaling to low power devices. In a typical Hall thruster, the discharge voltage drives the ionization process as outlined in chapter 2. Separating the ionization process from the acceleration process and discharge voltage allows for higher propellant utilization in low power devices [2]. The relation between the ionization and discharge potential of a Hall thruster can be seen in figure 1. As the discharge potential lowers, so does the ionization fraction.

6.1 Dual Stage Cylindrical Hall Thruster: Design

The proposed design of the dual stage thruster will be based on the dual stage Hall thrusters designed by Perez-Luna *et al.* [35] and the 2.6 cm Princeton Plasma Physics Laboratory Cylindrical Hall Thruster [41]. The design will adapt the PPPL geometry to accommodate a second stage via the use of a doubly peaked magnetic field and intermediate electrode as done by Perez-Luna [35]. It can be thought of simply as a Hall thruster pointing into another Hall thruster. The primary ionization stage is optimized to increase the ionization fraction of the fuel, and the secondary stage is optimized to increase the specific impulse of the thruster. The ionization region acts as an ion source, providing the ionized atoms required for operation and the electric field in the acceleration region accelerates the ions. The potential between the anode and intermediate electrode drives the ionization, and the potential between the intermediate electrode and cathode drives the acceleration.

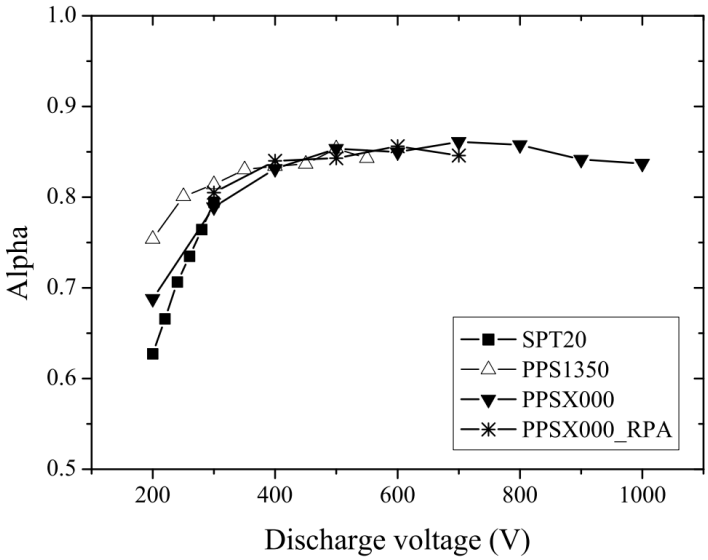

Figure 6.1: Propellant conversion efficiency α as a function of the discharge voltage for three types of Hall thrusters (from [9])

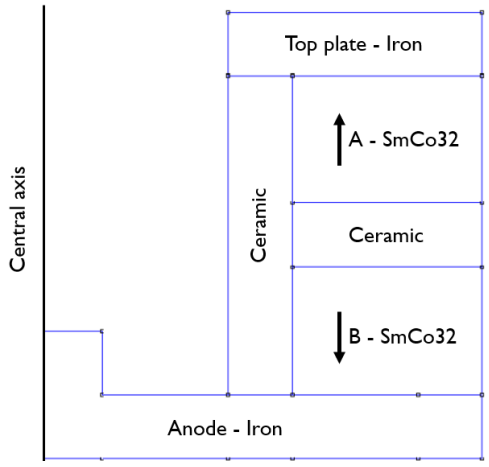

Figure 6.2: Diagram of proposed thruster

A doubly peaked magnetic field profile is one of two mechanisms by which the design implements dual stage operation. Annular coils cannot be used in a cylindrical geometry so significant change is required to implement the doubly peaked magnetic field. This magnetic profile was implemented using two permanent ring magnets and a ferromagnetic field enhancing anode. This orientation captured the doubly peaked magnetic profile while maintaining a cylindrical geometry. The proposed design can be seen in figure 6.2.

The proposed design was simulated in several configurations. The first was single stage operating mode, with only one permanent ring magnet. The simulation of the single stage configuration will help determine if the addition of a second stage helps with increasing the ionization fraction of the propellant.

6.2 DSCHT Simulations: Inputs

The same anomalous diffusion model examined for the PPPL 2.6 cm CHT in chapter 5 was used as the geometry, discharge voltage, and anode mass flow rate all remain unchanged from those simulations. The inputs for each simulation can are shown in table 6.1.

Dual Stage Cylindrical Hall Thruster Simulation Inputs		
Variable	Notation	Value
Channel Length	L	0.022 m
Channel Radius Inner	r_i	0 m
Channel Radius Outer	r_o	0.013 m
Discharge Voltage	U_d	250 V
Intermediate Electrode Voltage	U_e	200 V
Intermediate Electrode Position	z_e	$0.005 - 0.015$ m
Magnetic Field Maximum	$\mathbf{B}$	0.065 T
Ano. collision model	ν_{ano}	Bohm
Bohm Empirical Coefficient	α_{Bohm}	0.1
Propellant Mass (Xenon)	m	2.1746×10^{-25} kg
Mass Flow Rate	$\dot{m}_j$	0.4×10^{-6} kg/s
SEE Empirical Coefficient	α	0.02
Cell Size	dx	1×10^{-4} m
Time Step	dt	1×10^{-10} s

Table 6.1: Dual Stage Cylindrical Hall Thruster Simulation Inputs

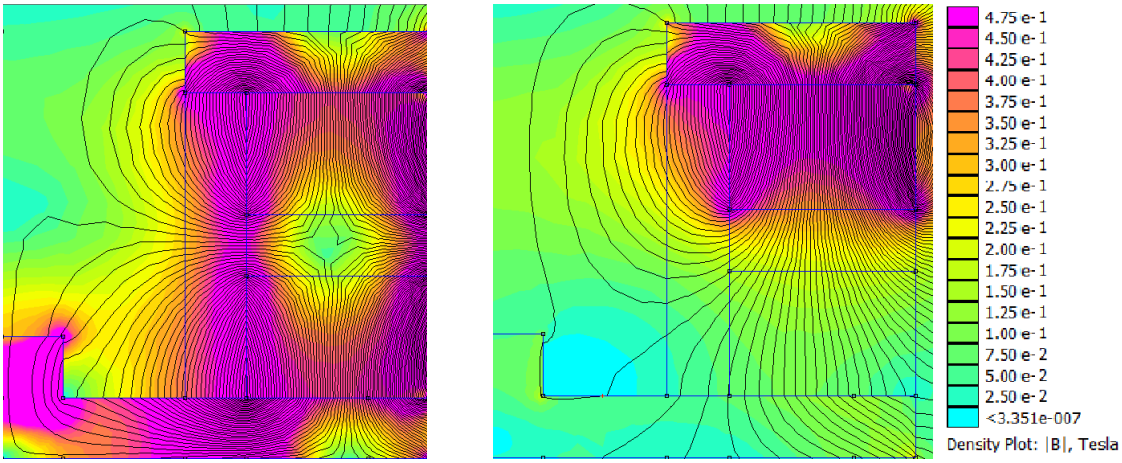

Figure 6.3: Simulated Magnetic Field profiles of the proposed Dual Stage Cylindrical Hall Thruster; Dual Stage (Left) and Single Stage (Right)

The same neutral gas expansion simulation was used as the PPPL 2.6 cm CHT. The magnetic field was simulated in FEMM in both single stage and dual stage orientations, the results of which can be seen in figure 6.3.
The magnetic field profile is shown in figure 6.4, in both single and dual stage orientations.

6.3 DSCHT Simulations: Results

The simulation results are shown in table 6.2. The ionization fraction in single stage operation was determined to be 0.75. This increased significantly with the addition of a second stage, with all dual stage simulation returning ionization fractions higher than 0.9 compared to the single stage thruster with an ionization fraction of 0.7. Ionization fraction values over 1 are indicative of a failure of the model. The assumption of a static neutral species allows for ionization fractions greater than 1, as there is not predator-prey relationship between the various plasma species with respect to the ionization process. Without introducing new neutrals and deleting the ionized neutrals, there is no limit on the ion mass flow rate exiting the thruster. This is what allows for ionization fractions above 1 in the model.

For simulation of the dual stage configuration, the central electrode was placed at intervals from $5 - 15$ mm from the anode and biased at 200 V, the results of which are shown in table 6.2. In addition to the increase in

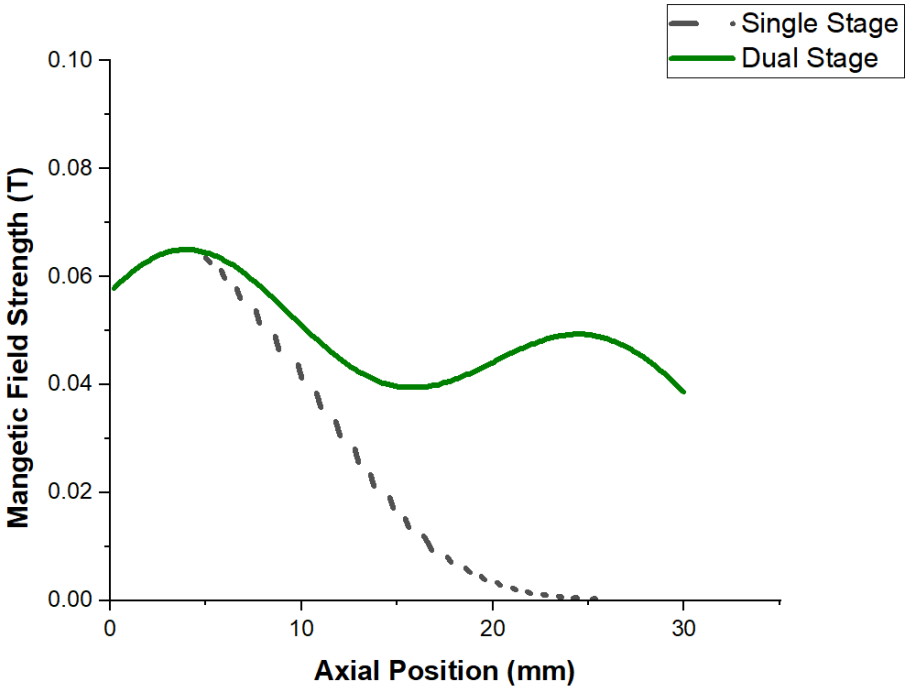

Figure 6.4: Magnetic Field Profile of Proposed Thruster

Electrode Position	Thrust	I_{sp}	Mass Efficiency	Anode Current
NA (Single stage)	5.0 mN	1273 s	0.752	0.22 A
5.00 mm	6.7 mN	1730 s	0.957	0.30 A
7.50 mm	7.9 mN	2027 s	1.120	0.35 A
10.0 mm	9.1 mN	2343 s	1.390	0.41 A
12.5 mm	6.9 mN	1777 s	0.983	0.31 A
15.0 mm	6.5 mN	1672 s	0.925	0.29 A

Table 6.2: Simulation results of single stage vs dual stage operation with varying central electrode placement (distance as measured from anode). Uncertainty for all measurements at ±8% relative.

Electrode Position	Thrust	I_{sp}	Mass Flow Rate	Anode Current
NA (Single stage)	5.0 mN	1273 s	0.4 mg/s	0.22 A
12.5 mm	6.9 mN	1777 s	0.4 mg/s	0.31 A
12.5 mm	4.5 mN	1700 s	0.25 mg/s	0.20 A

Table 6.3: Simulation results of single stage *vs* dual stage operation with varying mass flow rate, all measurements ±8%

ionization fraction, there is a significant increase in the thrust observed while in dual stage configuration. The thrust has to be limited by the available propellant though, so all results with a ionization fraction of 1 or higher should be dismissed. The highest thrust simulated with an ionization fraction < 1 was 6.97 mN, a 40% increase over the thrust observed in single stage operation.

The behaviour of the thruster is difficult to discern at electrode placements $7.5-10$ mm from the anode, as the ionization fraction returned is non-physical for steady state operation. Further experimental work or refinement to the model is required for investigation of those specific operational parameters.

With the increase in thrust comes an increase in anode power. From single stage to dual stage the anode power increases by 38.5 Watts. This will significantly increase the thermal load on the thruster, one of the limiting factors of low power thrusters. The thermal load is driven by Joule heating, and with a 50% increase in the anode current from single stage to dual stage operation, the thermal load will increase significantly. Thus the direct comparison at the same operating conditions is disingenuous, as it fails to account for this increased thermal load.

Scaling the mass flow rate down to achieve operation at a comparable anode power level between singe and dual stage operation allows for a more meaningful comparison. As outlined in chapter 2, the discharge current can be decreased via a decrease in the anode mass flow rate. Simulations were completed scaling down the flow rate from 0.4 mg/s to 0.25 mg/s. This resulted in a similar anode current and thrust, but a much higher specific impulse. Table 6.3 shows the results of this simulation. This indicates that the addition of a second stage can significantly increase the specific impulse of a low power cylindrical Hall thruster.

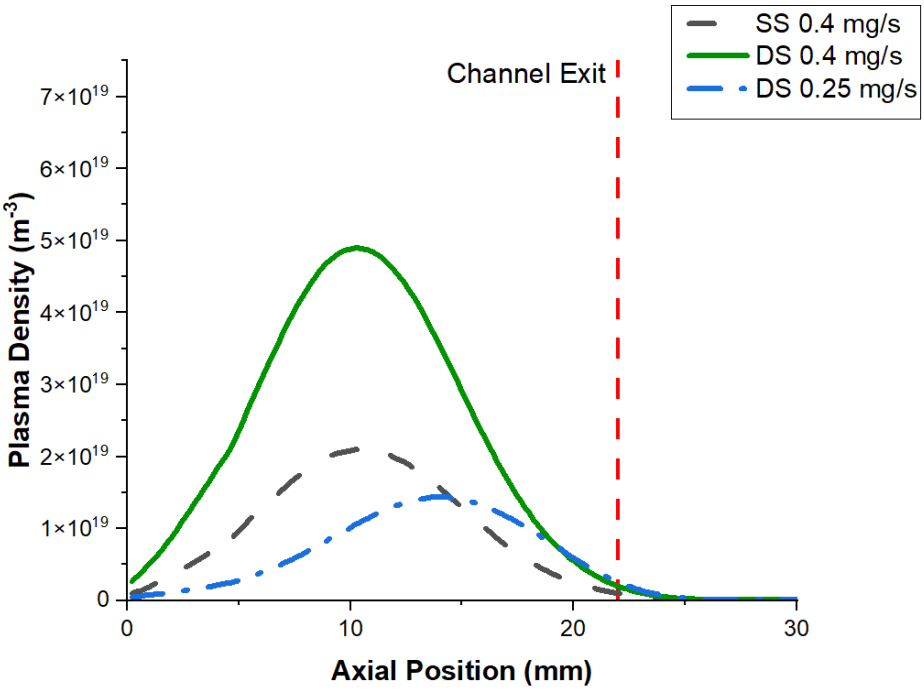

Figure 6.5: Electron Density in the proposed Dual Stage Hall Thruster (central electrode at 12.5 mm and 200 V for dual stage)

Figures 6.5 and 6.6 show the electron and neutral densities respectively in the both single and dual stage orientations. The single stage is the same as the PPPL 2.6 cm CHT. Using a doubly peaked magnetic field with a central electrode can convert that design to a dual stage orientation [35]. These simulation results indicate that the proposed dual stage design can increase the propellant ionization fraction at the cost of increased power and thermal loads. These issues can be mitigated by reducing the mass flow rate of the thruster. The resulting plasma density profile has a higher gradient and is located further along the thruster axis, both of which will contribute to a stronger electric field and increased thrust and specific impulse compared to the single stage thruster.

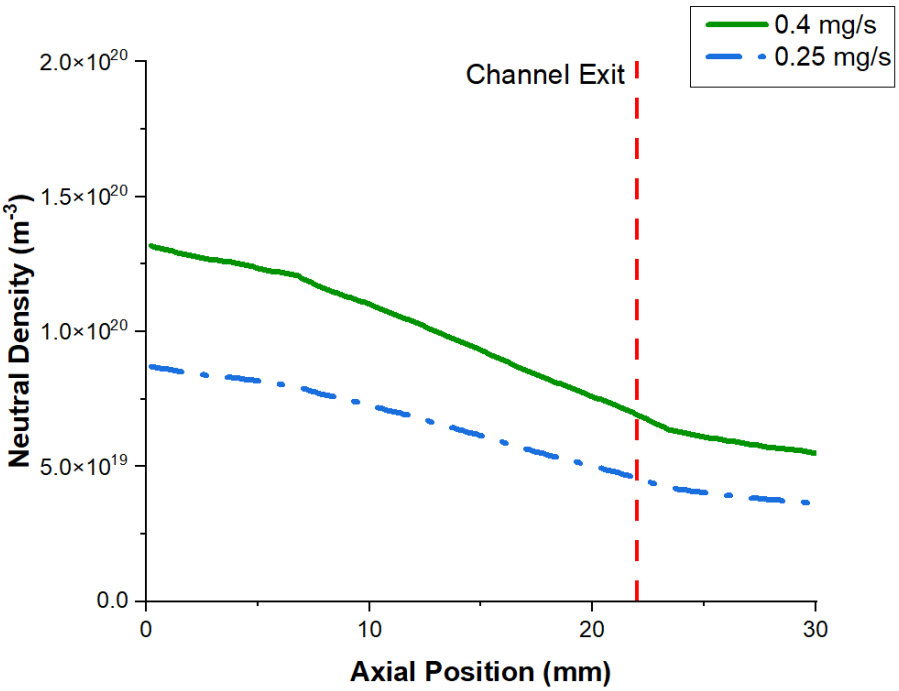

Figure 6.6: Neutral Density in the proposed Dual Stage Hall Thruster at $0.4mg/s$ and 0.25 mg/s

7 Conclusions

The research goals of this thesis were met: The RHS software is able to predicatively model the operational characteristics of Hall thrusters. The empirical nature of the anomalous electron mobility model used does limit the use of the model, but this is a characteristic of all numerical models for Hall thrusters at this point. The 1D nature of the model also limits the accuracy. However, in conjunction with experimental data, the RAPPEL Hall Simulation has, and will, allow for the RAPPEL lab to further investigate both the design of Hall thrusters, and the physical phenomenon present within them.

The proposed dual stage design offers the potential of significant increases in the specific impulse of the PPPL 2.6 cm CHT. The proposed mechanism of that increase is directly visible in the observed higher plasma density and higher propellant utilization in the dual stage orientation. A higher plasma density with the same mass flow rate indicates that there is a higher rate of propellant utilization.

7.1 Accuracy of predictive model

The precision of the model is directly tied to the macroparticle weight. Lower macroparticle weights increase precision significantly. The accuracy of the model is more difficult to define. The highly empirical nature of the anomalous electron mobility, and the methodology for the numerical exploration to determine the appropriate values for that empirical model inherently limit the inaccuracy. This is a characteristic of most all Hall thruster simulation software [42].

In comparison to other models, the RHS software still has significant room to improve. The 1D nature of the model limits accuracy and examination of Wall

effects and azimuthal waves within the plasma. The first order spatial ODE solver used in calculating the electric field and density gradients represents another area for improvement in the solver. The limit on spatial discretization outlined in chapter 5 limits the accuracy of the model, and this is very likely a result of the solver being implemented. The RAPPEL Hall Simulation in its current form still allows for meaningful investigation of existing and novel Hall thruster designs, and provides the base of future developments to increase the accuracy and scope of what it can acheive.

7.2 Future work

There are several directions that future work could potentially target. The first is improvement of the RHS software, specifically addressing the limitations on accuracy and resolution outlined earlier in Chapter 5. This can be done via the refinement of the ODE solver used, and the implementation of a second dimension. The way data is stored in the simulation could also be improved. Many plasma simulation softwares will use dimensionless units, or store density data in logarithmic form, but the RAPPEL Hall Simulation uses SI units throughout. The use of these modified units/representation can provide stability improvements to the solvers. Additional plasma species could be introduced as well; An excited neutral species, a transient neutral species, and a doubly charged ionic species. The inclusion of these species would increase the accuracy of simulation, and could provide more insight into the effects and mechanisms of anomalous diffusion. All of these would allow for improved investigation of Hall thrusters.

The second direction that future investigation could take is the investigation of the proposed dual stage design outlined in chapter 6. Experimental characterization of that design is a nature next step for the RAPPEL laboratory.

The third and final proposed future investigation is simply the use of the model, as it is sufficient in accuracy to use as a design tool. It was designed to fill the absence of Hall thruster modeling software and allow for numerical exploration to compliment physical experimentation within the lab. While there are some limits, the use of similar thrusters to determine optimal empirical coefficient values for operation at that power level can provide meaningful insight into the operation of the thruster.

Bibliography

[1] Colin J. Aro. Chemsode: a stiff ode solver for the equations of chemical kinetics. *Computer Physics Communications*, 97(3):304–314, 1996.

[2] Joseph Ashkenazy, Y. Raitses, and G. Appelbaum. 2nd european spacecraft propulsion conference. volume 398, page 455, 05 1997.

[3] C.D.R. Azevedo, Diego Gonzalez Diaz, Stephen Biagi, C.A.B. Oliveira, Carlos Henriques, J. Escada, F. Monrabal, Juan Gómez-Cadenas, Vicente Alvarez, J. Borges, A. Botas, Sara Cárcel, J.V. Carrión, S. Cebrián, Carlos Conde, José Díaz, M. Diesburg, R. Esteve, Ryan Felkai, and N. Yahlali. Microscopic simulation of xenon-based optical tpcs in the presence of molecular additives. *Nuclear Instruments and Methods in Physics Research Section A: Accelerators, Spectrometers, Detectors and Associated Equipment*, 877, 05 2017.

[4] S. Boccelli, T. Charoy, A. Alvarez Laguna, P. Chabert, A. Bourdon, and T. E. Magin. Collisionless ion modeling in hall thrusters: Analytical axial velocity distribution function and heat flux closures. *Physics of Plasmas*, 27(7):073506, 2020.

[5] Jean-Pierre Boeuf. Tutorial: Physics and modeling of hall thrusters. *Journal of Applied Physics*, 121(1):011101, 2017.

[6] Lubos Brieda and Michael Keidar. Development of the starfish plasma simulation code and update on multiscale modeling of hall thrusters. *48th AIAA/ASME/SAE/ASEE Joint Propulsion Conference*.

[7] Mark Cappelli, Christopher Young, Eunsun Cha, and Eduardo Fernández. A zero-equation turbulence model for two-dimensional hybrid hall thruster simulations. *Physics of Plasmas*, 22:114505, 11 2015.

[8] Birdsall CK. Plasma physics via computer simulation. *IOP Publishing*, pages 1–50, 1990.

[9] Käthe Dannenmayer and S. Mazouffre. Elementary scaling laws for the design of low and high power hall effect thrusters. *EUCASS Proceedings Series*, pages 601–616, 10 2011.

[10] Zoltán Donkó, Peter Hartmann, and Gabor Kalman. Strongly coupled plasma liquids. *Research Institute for Solid S tate Physics and Optics, Hungarian Academy of Sciences*, 11 2007.

[11] A Einstein. On the movement of small particles suspended in stationary liquids required by the molecular-kinetic theory of heat. *Annalen der Physik*, 1905.

[12] D Frem. A reliable method for predicting the specific impulse of chemical propellants. *J Aerosp Technol Manag*, 10, 2018.

[13] L. Garrigues, Jean-Pierre Boeuf, and Iain Boyd. Computation of hall thruster performance. *Journal of Propulsion and Power - J Propul Power*, 17:772–779, 07 2001.

[14] Nicolas Gascon and S. Barral. Wall material effects in stationary plasma thrusters. i. parametric studies of an spt-100. *Physics of Plasmas*, 10:4123–4136, 10 2003.

[15] Curtis Graham and Manish Jugroot. Development of a 1d hybrid fluid-pic plasma model of low power hall thrusters for small spacecraft - manuscript. 08 2023.

[16] Lou Grimaud, A. Pétin, Julien Vaudolon, and S. Mazouffre. Perturbations induced by electrostatic probe in the discharge of hall thrusters. *Review of Scientific Instruments*, 87:043506, 04 2016.

[17] G. J. M. Hagelaar, J. Bareilles, L. Garrigues, and J. P. Boeuf. Two-dimensional model of a stationary plasma thruster. *Journal of Applied Physics*, 91(9):5592–5598, 2002.

[18] G J M Hagelaar and L C Pitchford. Solving the boltzmann equation to obtain electron transport coefficients and rate coefficients for fluid models. *Plasma Sources Science and Technology*, 14(4):722, oct 2005.

[19] Richard Hofer, Ioannis Mikellides, Israel Katz, and Dan Goebel. Wall sheath and electron mobility modeling in hybrid-pic hall thruster simulations. *Collection of Technical Papers - 43rd AIAA/ASME/SAE/ASEE Joint Propulsion Conference*, 3, 07 2007.

[20] K. Holste and P. Dietz. Ion thrusters for electric propulsion: Scientific issues developing a niche technology into a game changer. *Review of Scientific Instruments*, 91(6):061101, 2020.

[21] Ugur Kokal. Development of a mili-newton level thrust stand for thrust measurements of electric propulsion systems and uk90 hall effect thruster. *Istanbul Technical University, PhD Thesis*, 2018.

[22] Justin W. Koo and Iain D. Boyd. Modeling of anomalous electron mobility in hall thrusters. *Physics of Plasmas*, 13(3):033501, 2006.

[23] W. B. Kunkel. Hall effect in a plasma. *American Journal of Physics*, 49(8):733–738, August 1981.

[24] Kybeom Kwon, Mitchell Walker, and Dimitri Mavris. Self-consistent, one-dimensional analysis of the hall effect thruster. *Plasma Sources Science and Technology*, 20:045021, 07 2011.

[25] Andrea Leporini. One-dimensional model of a hall effect thruster and anomalous electron transport. *Universita Di Pisa*, 2014.

[26] Dan Lev, Roger M. Myers, Kristina M. Lemmer, Jonathan Kolbeck, Hiroyuki Koizumi, and Kurt Polzin. The technological and commercial expansion of electric propulsion. *Acta Astronautica*, 159:213–227, 2019.

[27] J Linnell and A Gallimore. Hall thruster electron motion characterization based on internal probe measurements. *IEPC-2009-105*, 2009.

[28] Hui Liu, Boying Wu, Daren Yu, Yong Cao, and Ping Duan. Particle-in-cell simulation of a hall thruster. *Journal of Physics D: Applied Physics*, 43(16):165202, apr 2010.

[29] Franz Mandl. Statistical physics, second edition. *The Manchester Physics Series*, pages 1–416, 01 1991.

[30] David Meeker. *Finite Element Method Magnetics*. 2020.

[31] Ioannis Mikellides, Israel Katz, Myron Mandell, and J. Snyder. A 1-d model of the hall-effect thruster with an exhaust region. 07 2001.

[32] Ioannis G Mikellides and Alejandro Lopez Ortega. Challenges in the development and verification of first-principles models in hall-effect thruster simulations that are based on anomalous resistivity and generalized ohm's law*. *Plasma Sources Science and Technology*, 28(1):014003, jan 2019.

[33] Carrie Niemela, Lubos Brieda, Michael Nakles, Jared Ekholm, and William Hargus. Comparison of hall thruster plume expansion model with experimental data. *Collection of Technical Papers - AIAA/ASME/SAE/ASEE 42nd Joint Propulsion Conference*, 3, 07 2006.

[34] Mario Panelli, Davide Morfei, Beniamino Milo, Francesco Antonio D'Aniello, and Francesco Battista. Axisymmetric hybrid plasma model for hall effect thrusters. *Particles*, 4(2):296–324, 2021.

[35] J. Perez-Luna, G. J. M. Hagelaar, L. Garrigues, and J. P. Boeuf. Model analysis of a double-stage hall effect thruster with double-peaked magnetic field and intermediate electrode. *Physics of Plasmas*, 14(11):113502, 2007.

[36] Alexander Piel. Plasma physics – an introduction to laboratory, space, and fusion plasmas, 2nd edition. *Springer*, pages 1–72, 08 2010.

[37] Kurt Polzin, E. Sooby, Adam Kimberlin, Y. Raitses, Enrique Merino, and Nathaniel Fisch. Performance of a permanent-magnet cylindrical hall-effect thruster. 08 2009.

[38] Donald Rapp and Paula Englander-Golden. Total cross sections for ionization and attachment in gases by electron impact. i. positive ionization. *Journal of Chemical Physics*, 43:1464–1479, 1965.

[39] John M. Sankovic, John A. Hamley, and Thomas Haag. Performance evaluation of the russian spt-100 thruster at nasa lerc. 1994.

[40] Hanspeter Schaub, Gordon Parker, and Lyon King. Coulomb thrusting application study. page 120, 01 2006.

[41] A.N. Smirnov, Y. Raitses, and N.J. Fisch. Electron cross-field transport in a miniaturized cylindrical hall thruster. *IEEE Transactions on Plasma Science*, 34(2):132–141, 2006.

[42] Francesco Taccogna and Laurent Garrigues. Latest progress in hall thrusters plasma modelling. *Reviews of Modern Plasma Physics*, 3, 12 2019.

[43] Christopher Tacon. Electron cyclotron resonance gridded ion thruster optic development. *University of Southampton, MSc Thesis*, 11 2019.

[44] Hirokazu Tahara, Takashi Fujioka, Atsushi Shirasaki, and Takao Yoshikawa. Simple one-dimensional calculation of hall thruster flowfields. *Journal of the Japan society for aeronautical and space sciences*, 51, 09 2003.

[45] Tokoshi Tajima. Computational plasma physics. *CRC Press*, pages 1–24, 2004.

[46] Blagonravov A.A. Tsiolkovsky, K.E. Collected works of ke. tsiolkovsky, volume ii - reactive flying machines, translation of "k.e. tsiolkovskiy, sobraniye sochmeniy, tom ii - reaktivnyye letatal'nyye apparaty". *NASA History Newsletter*, pages 71–117, 1965.

[47] Martin Turner. Rocket and spacecraft propulsion principles, practice and new development. *Springer*, 2009.